การศึกษาความเป็นไปได้ของการใช้เทคนิคการวิเคราะห์ด้วยนิวตรอนพลังงานสูง
เพื่อเสริมเทคนิคการวิเคราะห์ด้วยนิวตรอนอุณหภาพในการตรวจกับระเบิด
โดยการจำลองด้วยโปรแกรมมอนติคาร์โล

นายอนันท์ สัจจา

FEASIBILITY STUDY OF USING FAST NEUTRON

ANALYSIS TO COMPLEMENT THERMAL NEUTRON

ANALYSIS IN LANDMINE DETECTION

BY MONTE CARLO SIMULATION

Anan Sutcha

A Thesis Submitted in Partial Fulfillment of the Requirements for the

Degree of Master of Philosophy in Physics

Suranaree University of Technology

Academic Year 2011

FEASIBILITY STUDY OF USING FAST NEUTRON ANALYSIS TO COMPLEMENT THERMAL NEUTRON ANALYSIS IN LANDMINE DETECTION BY MONTE CARLO SIMULATION

Suranaree University of Technology has approved this thesis submitted in partial fulfillment of the requirements for the Degree of Master of Science.

Thesis Examining Committee

_____

(Assoc. Prof. Dr. Prapun Manyum)

Chairperson

_____

(Asst. Prof. Dr. Chinorat Kobdaj)

Member (Thesis Advisor)

_____

(Assoc. Prof. Dr. Worasit Uchai)

Member

_____

(Dr. Worawat Meevasana)

Member

_____   _____

(Prof. Dr. Sukit Limpijumnong)   (Assoc. Prof. Dr. Prapun Manyum)

Vice Rector for Academic Affairs   Dean of Institute of Science

อนันท์ สัจจา : การศึกษาความเป็นไปได้ของการใช้เทคนิคการวิเคราะห์ด้วยนิวตรอน
พลังงานสูงเพื่อเสริมเทคนิคการวิเคราะห์ด้วยนิวตรอนอุณหภาพในการตรวจกับระเบิดโดย
การจำลองด้วยโปรแกรมมอนติคาร์โล (FEASIBILITY STUDY OF USING FAST
NEUTRON ANALYSIS TO COMPLEMENT THERMAL NEUTRON ANALYSIS IN
LANDMINE DETECTION) อาจารย์ที่ปรึกษา : ผู้ช่วยศาสตราจารย์ ดร.ชิโนรัตน์ กอบเดช,
126 หน้า.

วิทยานิพนธ์นี้ได้ทำการศึกษาความเป็นไปได้ในการใช้เทคนิคการวิเคราะห์ด้วยนิวตรอน
พลังงานสูงร่วมกับเทคนิคการวิเคราะห์ด้วยนิวตรอนอุณหภาพ เพื่อใช้ประโยชน์ในการวัดรังสี
แกมมาที่เกิดจากการก่อกัมมันต์กับธาตุองค์ประกอบของทีเอ็นที (TNT, $C_7H_5O_6N_3$) ได้แก่
ไฮโดรเจน คาร์บอน ไนโตรเจน และออกซิเจน โดยใช้โปรแกรมมอนติคาร์โล (MCNP5) จำลอง
การวัดรังสีแกมมาด้วยชุดหัววัดของแหล่งกำเนิดนิวตรอน แคลิฟอเนียม (^{252}Cf) และอเมอริเซียม
เบอร์รินเลียม (^{241}Am-^{9}Be) ร่วมกับหัววัด NaI(Tl) BGO และ LaBe$_3$:Ce โดยฝังกับระเบิดที่มีมวล
ของทีเอ็นทีแตกต่างกัน ที่ความลึกแตกต่างกันใต้ชั้นดินทราย ดินปูน และดินร่วน ในการจำลอง
ทีเอ็นที 1 กิโลกรัม ฝังลึก 5 เซนติเมตร ใต้ชั้นดินทราย ปรากฏรังสีแกมมาของ 2.22 4.44 6.13 และ
10.83 MeV ซึ่งสรุปได้ว่ารังสีแกมมาเหล่านี้เกิดจากการก่อกัมมันต์ของ ไฮโดรเจน คาร์บอน
ออกซิเจน และไนโตรเจน ตามลำดับ จากนั้นนำฟลักซ์ของรังสีแกมมาที่ได้จากการจำลองมาคิด
สัดส่วนกัน ระหว่าง 2.22 และ 10.83 MeV (C_H/C_N) 4.44 และ 10.83 MeV (C_C/C_N) และ 2.22 และ
4.44 MeV (C_H/C_C) เพื่อเปรียบเทียบกับค่าทางทฤษฎี พบว่าสัดส่วนของฟลักซ์รังสีแกมมา C_H/C_N ที่
ได้จากหัววัด LaBe$_3$:Ce มีค่าสอดคล้องกับค่าทางทฤษฎีภายใต้ค่าความคลาดเคลื่อน ในขณะที่
C_C/C_N และ C_H/C_C มีค่าไม่สอดคล้อง โดยมีความแตกต่างอยู่ประมาณ 5 และ 2 เท่า ตามลำดับ
ซึ่งผลการจำลองดังกล่าวสามารถบอกเป็นนัยได้ว่า การใช้เทคนิคการวิเคราะห์ด้วยนิวตรอน
พลังงานสูงร่วมกับนิวตรอนอุณหภาพนั้น ไม่สามารถใช้ได้ในกรณีของการตรวจกับระเบิดทีเอ็นที
1 กิโลกรัม ฝังลึก 5 เซนติเมตรใต้ชั้นดินทราย อย่างไรก็ตาม เนื่องจากค่าสัดส่วนของ C_H/C_N มีค่า
สอดคล้องกับทางทฤษฎี ดังนั้นการใช้เทคนิคการวิเคราะห์ด้วยนิวตรอนอุณหภาพ สามารถใช้ตรวจ
กับระเบิดทีเอ็นที 1 กิโลกรัม ที่ฝังลึก 5 เซนติเมตร ใต้ชั้นดินทรายได้ และเนื่องจากองค์ประกอบ
ของชั้นดินทรายนั้นมีธาตุออกซิเจน เหมือนกันกับทีเอ็นที ซึ่งให้รังสีแกมมาพลังงาน 6.13 MeV
ดังนั้นในวิทยานิพนธ์เล่มนี้ จึงไม่ใช้ฟลักซ์รังสีแกมมาพลังงานดังกล่าวเข้าร่วมวิเคราะห์สัดส่วนกับ
ทางทฤษฎี ยิ่งไปกว่านั้น ในการจำลองการวัดรังสีแกมมา ในกรณีศึกษาของชั้นดินปูนและชั้นดิน

ร่วม พบว่าชั้นดินทั้งสองชนิดให้รังสีแกมมาที่มีพลังงานเดียวกันกับรังสีแกมมาที่มาจากกับระเบิด ดังนั้นจึงไม่ได้เปรียบเทียบค่าสัดส่วนจากการจำลองและสัดส่วนจากทฤษฎี

สาขาวิชาฟิสิกส์	ลายมือชื่อนักศึกษา _____
ปีการศึกษา 2554	ลายมือชื่ออาจารย์ที่ปรึกษา _____
	ลายมือชื่ออาจารย์ที่ปรึกษาร่วม _____

ANAN SUTCHA : FEASIBILITY STUDY OF USING FAST NEUTRON
ANALYSIS TO COMPLEMENT THERMAL NEUTRON ANALYSIS IN
LANDMINE DETECTION. THESIS ADVISOR : ASST. PROF.
CHINORAT KOBDAJ, Ph.D. 126 PP.

NEUTRON TECHNIQUE / LANDMINE DETECTION / TNA & FNA / FAST
NEUTRON ANALYSIS / THERMAL NEUTRON ANALYSIS

A Monte Carlo computer code, MCNP5, is used to simulate the detection of
TNT-landmine. The complementary FNA-TNA technique is used in this thesis. This
technique utilizes the detections of gamma-rays resulting from the thermal and fast
neutron activations of TNT's elemental compositions, H, C, N and O. The detector
heads used in the simulations are the combinations of ^{252}Cf- and ^{241}Am-^{9}Be- neutron
sources and NaI (Tl)-, BGO- and LaBe$_3$:Ce- gamma-ray detectors. TNT-landmines of
varying masses buried under sand-, CaCO$_3$- and clay-formations are used in the
simulations. Gamma-ray spectra resulting from the simulations of the detections of 1
kg TNT-landmine buried under formations at 5 cm depth are obtained. The gamma-
ray fluxes of the 2.22, 4.44, 6.13 and 10.83 MeV resulting from neutron activations of
H,C,O and N, respectively, are deduced. The simulated ratios of gamma-ray fluxes
between the 2.22 and 10.83 MeV (C_H/C_N), the 4.44 and 10.83 MeV (C_C/C_N) and the
2.22 and 4.44 MeV (C_H/C_C) are estimated and compared their results to those of the
theoretical ratios. The simulated ratio of C_H/C_N based on using LaBe$_3$:Ce gamma-ray
detector agrees with its theoretical ratio within their error limits. However, the
simulated C_C/C_N and C_H/C_C ratios of LaBe$_3$:Ce gamma-ray detector do not agree with

each other. They are about 10 and 2 times different, respectively. These results imply that the complementary FNA-TNA technique based on using LaBe$_3$:Ce can't be used to detect 1 kg TNT-landmine buried under sand-formation at 5 cm depth. However, since the theoretical and simulated C_H/C_N ratios agree with each other, it implies that the TNA technique can be used to detect 1 kg TNT-landmine buried under sand-formation at 5 cm depth. Since sand-formation has oxygen as its elemental compositions, the 6.13 MeV gamma-rays are not used in this thesis to compare between theoretical and simulated ratios. Moreover, since gamma-ray spectra resulting from the detections based on using CaCO$_3$ and clay as formations give interference, their spectra are not used in the comparison between theoretical and simulated ratios.
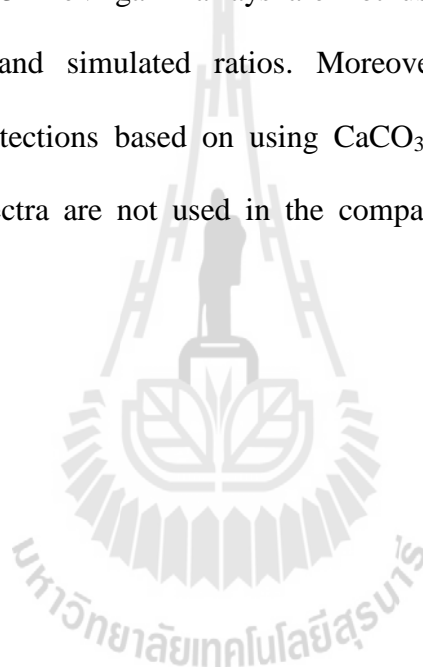
School of Physics   Student's Signature _____

Academic Year 2011   Advisor's Signature _____

                                                     Co-Advisor's Signature _____

ACKNOWLEDGEMENTS

I am grateful to Asst. Dr. Chinorat Kobdaj for being my thesis adviser. His advice on parallel methods of MCNP simulations that reduce simulation times has saved a lot of time required for running the program.

I would like to thanks Assoc. Dr. Prapun Manyum and Dr. Worawat Meevasana for being the examination committee of my thesis.

I would like to thank Dr. Sommai Shangkian and Dr. Jiraroj T-Thienprasert for their consistent help, especially on computer programming.

I would like to thank all my friends at SUT for their friendship and support during my M.Sc. study.

I acknowledge the financial support from Suranaree University of Technology.

Special thanks to my parents and family members for encouragement during my M.Sc. study.

More importantly, I would like to thanks Assoc. Dr. Worasit Uchai for being my thesis co-adviser. He set up the topic of my thesis research and gives valuable guidance and support on my thesis research throughout my M.Sc. study.

Anan Sutcha

CONTENTS

CONTENTS (Continued)

CONTENTS (Continued)

CONTENTS (Continued)

CONTENTS (Continued)

CONTENTS (Continued)

LIST OF TABLES

LIST OF TABLES (Continued)

LIST OF FIGURES

LIST OF FIGURES (Continued)

Figure

Page

LIST OF FIGURES (Continued)

Figure

Page

LIST OF FIGURES (Continued)

Figure

Page

LIST OF FIGURES (Continued)

Figure

Page

LIST OF FIGURES (Continued)

Figure

Page

LIST OF FIGURES (Continued)

Figure

Page

CHAPTER I

INTRODUCTION

1.1   Problem of Abandoned Landmine

Abandoned landmines cause serious humanitarian problems in many countries of the world (Monin and Gillimore, 2002). It is estimated that more than 100 million abandoned landmines are buried under ground of about 70 countries throughout the world. These landmines either killed or injured people who accidentally stepped on them. It is believed that number of civilians accidentally killed exceeds 25,000 per year worldwide and even larger numbers are maimed. Many of the victims of the abandoned landmines are women and children. Most of the casualties are caused by small anti-personnel landmines that are difficult to detect and remove using existing technologies. Figure 1.1 shows landmine affected Cambodians who arrive to receive support on November 19, 2010 at a district office, Battambang province, Cambodia (Lisa McCoy, 2010). Figure 1.2 represents a Cambodian woman walking past a landmine awareness sign near Thai-Cambodian border in July, 2007 (Miranda Leitsinger, 2009). According to the mine impact survey level 1, conducted by The United Nations as part of the international campaign to ban landmine, 17 countries are considered as the serious mine problem countries (humanitarian demining R&D program). Angola is considered as the most serious country that has abandoned landmine problem. Afghanistan, Cambodia and Mozambique, respectively, are listed as the the next most serious countries on the abandoned landmines.

Figure 1.1 Landmine affected Cambodians who arrive to receive support on November 19, 2010, at a district office, Battambang Province, Cambodia (Lisa McCoy, 2010).

Figure 1.2 A Cambodian woman walks past landmine awareness sign near Thai-Cambodian border in July 2007 (Miranda Leitsinger, 2009).

Abandoned landmines also caused serious problems to Thailand and its neighboring countries. It is estimated that 4-6 millions of abandoned landmines are spread over borders between Thailand and its neighboring countries, Cambodia, Lao PDR, Myanmar and Malaysia. It is indicated that the Thai-Cambodian border is the most landmines contaminated in the region. There are about 46 percents of Cambodian villages contaminated with landmines. For Lao PDR, it is difficult to select sites to develop for irrigation and agriculture purposes as there is a risk of stepping on unexploded ordinance (UXO) or landmine when digging the ground. In 2001, there was a report that 35 Lao people were killed and 87 injured because stepping on UXO and mines. According to the report of The Landmine Impact Survey (Landmine Monitor report, 2010), Thailand contains 530 landmine contaminated communities along the borders with its neighbors. Cambodia, Myanmar, Lao PDR and Malaysia contribute to the total contaminated community of Thailand with 297, 139, 90 and 4 communities, respectively. Figure 1.3 shows the map of landmine contaminated areas along border of Thailand and its neighboring countries (Landmine impact survey report, 2001). These contaminated communities affect the livelihood and safety of about 503,682 Thai people who live in 27 provinces. So far, there are 3,468 victims who accidentally step on the abandoned landmines in these communities, 1497 killed and 1,971 injured.
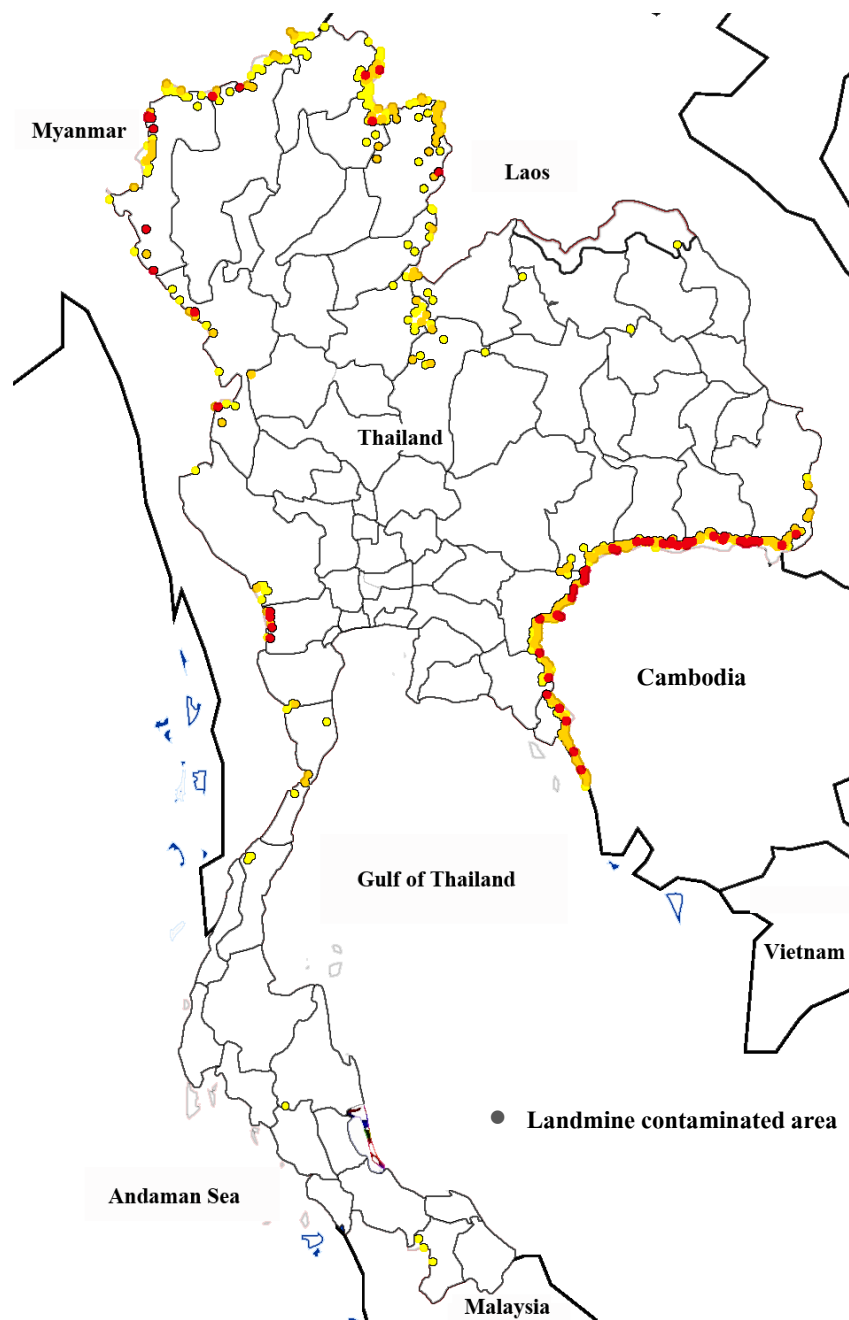
Figure 1.3 A map of landmine contaminated communities in Thailand along its border with neighboring countries (Landmine impact survey report, 2001).

So far, the loss of life and injury of civilians accidentally stepping on abandoned landmines throughout the world has tremendous consequences to world's population. Each country has to spend a lot of money to hospitalize its maimed population. Because of this, Ottawa Treaty or the Anti-Personnel Mine Ban Convention was held in Ottawa, Ontario, Canada in December 3, 1997 with the aim to stop the effect of anti-personnel landmine around the world. The agreements between Ottawa Treaty's state parties are the prohibition of the use, stockpiling, production and transfer of anti-personnel mines and on their destruction. As of April, 2010, there were 156 states parties out of 194 world's states (Ottawa Treaty, Wikipedia Website). However, the anti-personnel landmine effect still persists because of the lack of human resources, budget and efficient equipment for the detection and removal of landmines. At present, the landmine detection equipments available have limited capability, especially for humanitarian demining (HD). During September 15-18, 2003, the International Atomic Energy Agency (IAEA) called for the International Conference on Requirement and Technologies for the Detection and Neutralization of Landmine and UXO. Participants from universities and research institutes from 18 countries around the world participated in the conference. The conference's participants recommended that nuclear techniques which utilize neutrons and gamma rays should be used for obtaining the desired equipment (IAEA, 1999, 2001, 2003).

1.2   Type of Landmines and Detection Methods

In the field of HD, there are two types of landmines, anti-tank mines (ATM) and anti-personnel mines (APM). The ATM has mass of about 5 kg while the APM has, typically, less than 300 g. In order for the landmine to be detonated when a target

(person or tank) puts weight on it, the buried depth has to be within a few centimeters of the ground surface. Therefore, the detection method should be able to detect buried mines at a few centimeters deep. Furthermore, because the mine can be moved to other positions which are deeper due to natural or other causes, the efficient detection method should be able to detect mines at larger depth. Otherwise, a mine can be hazardous later on because the force exerted on it is reduced, by transmission through soil, until too low to actuate the detonator. Other than that, the detection method should be reliable and fast so that it can serve the HD mission satisfactorily. The established methods for landmine detection which has been used for HD includes metal detector, ground penetrating radar, sniffer dog and probing stick. These methods are insufficient for HD because they are too slow and expensive. The metal detector itself has limited capability, especially when use to detect artificial landmine which does not contain metal in its components.

1.3   Nuclear Techniques for APM Detection

There are various nuclear techniques used for APM detection, such as, x-ray backscattering, gamma-ray back scattering, and neutron-induced gamma-ray techniques. The later technique can be classified into four groups; 1) neutron-induced gamma emission, 2) neutron energy moderation, 3) neutron and gamma attenuation and 4) fast neutron back scattering. In group 1), neutrons of 14-MeV from a neutron generator is used to bombard sample buried under ground and a gamma-ray detector is used to detect gamma rays emitted from the sample. The pulse height spectrum from the detector is analyzed to identify the nuclei and hence the elemental compositions of the sample. The ratios of these elements can identify the type of

sample which may be a landmine. Examples of this approach are the Pulsed Elemental Analysis using Neutrons (PELAN) system (Vourvopoulos et al., 2003) and the Nanoseconds Neutron Analyzer (NNA) system (Kuznetsov et al., 2003). In group 2), neutrons from an isotopic source are used to bombard the sample and a neutron detector is used to detect fluxes of thermal and epithermal back-scattered neutrons which proportional to H-elemental composition of the sample. These fluxes can be used to identify landmine because its H-elemental composition is different from other materials buried under ground. Some examples of this approach are: Delft University Neutron Back-Scattering Landmine Detector (DUNBLAD) from the Netherland (Bom et al., 2004), Detection and Imaging of Anti-personnel Landmines by Neutron Backscattering Technique (DIAMINE) (Viesti et al., 2006) and Hydrogen Density Anomaly Detector (HYDAD) from South Africa (Brooks et al., 2005). In group 3), both neutrons and gamma rays are used to bombard the target buried under ground and both neutron and gamma ray detectors are used to detect the transmissions of neutrons and gamma rays, respectively. The Hydrogen Radiography (HYRAD) is created from both transmission signals (Bartle et al., 1990). In group 4), fast neutrons from a radioactive source are used to bombard the sample and a neutron detector is used to detect backscattering neutrons. The flux of backscattered neutron can identify the type of sample similar to HYDAD (Buffler et al., 2001; Csikai et al., 2001). There are other research works which relate to using nuclear techniques for APM detection. The details of these works can be obtained from the following references:(ElAgib, et al., 2008); (Miri-Hakimabad, et al., 2007); (Maucec and Rigollet, 2004); (Hussein and Waller, 2000).

Recently, there is a research work which is of interest to us. This is the work of the Canadian Department of National Defense which developed a tele-operated, vehicle mounted, multi-sensor system to detect ATM on roads and tracks in peacekeeping operations (Clifford, et al., 2007). The thermal neutron activation (TNA) technique is used in this work which emphasizes on detecting the 10.83 MeV gamma-ray associated with thermal neutron capture on ^{14}N. It uses a 100 microgram ^{252}Cf- neutron source and four NaI (Tl)- detectors of 7.62 cm x 7.62 cm size. This technique can detect the ATM buried at 10 cm deep within 3 minutes and at 30 cm deep within 100 seconds.

Another research work is the work of researcher at Bubble Technology Industries Inc., Chalk River, Ontario, Canada (Faust, et al., 2004). These researchers used fast neutrons from a neutron generator to detect landmines by using fast neutron activation (FNA) technique to complement the TNA technique. However, they found that there are too much interference between the gamma-rays from fast neutron interactions from the ground formation's constituents and the gamma-rays from the landmine's constituents. They suggested that this technique can't be used to detect landmine buried under ground-formation.

In this thesis, we want to do the feasibility study of using the FNA technique to compliment the TNA technique in landmine detection. This technique will be referred to as the complementary FNA-TNA technique in this thesis. MCNP5, a Monte Carlo computer code, will be used to do the landmine detection simulation for the feasibility study. The simulation components of this study consist of the radioactive neutron source, the gamma-ray detector, the detected sample and the ground-formation. In this study, two neutron sources, ^{252}Cf and ^{241}Am-^{9}Be, three

gamma-ray detectors, Sodium iodide (NaI(Tl)), Bismuth germinate (BGO, $Bi_4Ge_3O_{12}$) and Lanthanum halide (LaBr$_3$:Ce) and three ground-formations, sand, $CaCO_3$ and clay will be used as the simulation components.

CHAPTER II

THEORY

In this Chapter, theories relevant for the analysis and discussion of the simulation results in Chapter IV are discussed. The following sections, then, give the theories of neutron interaction with matter, neutron cross section, gamma-ray interaction with matter, and response function of gamma-ray detector.

2.1 Neutron Interaction with Matter

It is important to recognize that neutrons, which are constituents of the nuclei, are electrically neutral. They are not affected by the electrons in an atom or by the positive charge due to proton of the nucleus. Therefore, when neutrons interact with matters, they will pass through the atomic electron cloud and interact directly with the nucleus. As a consequence, the probability or cross section for nuclear interaction is higher for neutron than for charge particle. There are five ways which neutrons may interact with matter; elastic scattering, inelastic scattering, radiative capture, neutron-producing reaction and fission reaction. The following sections discuss the characteristic of neutron interaction with matters.

2.1.1 Elastic Scattering

In elastic scattering, when neutrons strike the nucleus which is always almost in its ground state, the nucleus is left in its ground state while the neutron reappeared.

In this case, the neutron is said to be elastically scattered by the nucleus. The total kinetic energy of the two colliding particles is conserved. The kinetic energy is simply redistributed between the two particles. The elastic scattering is denoted by the symbol (n, n) or as

$$n + {}_Z^A X \rightarrow {}_Z^A X + n \tag{2.1}$$

2.1.2 Inelastic Scattering

Inelastic scattering is identical to elastic scattering except that the nucleus is left in an excited state. Part of the kinetic energy of the neutron is given to the nucleus as excitation energy. After the collision, the excited nucleus will return to the ground state by emitting one or more gamma-rays. The inelastic scattering which is denoted by The symbol (n, n′γ) is an endothermic reaction because the energy is retained by the nucleus.

The following reactions are examples of inelastic scattering interactions which correspond to neutrons interactions with C, N, O, and Si, respectively.

$$^{12}C + {}_0^1 n\,(14\,MeV) \rightarrow ({}^{12}C)^*\,(4.44\,MeV) + {}_0^1 n \tag{2.2}$$

$$^{14}N + {}_0^1 n\,(14\,MeV) \rightarrow ({}^{14}N)^*\,(1\,MeV) + {}_0^1 n \tag{2.3}$$

$$^{16}O + {}_0^1 n\,(14\,MeV) \rightarrow ({}^{16}O)^*\,(3\,MeV) + {}_0^1 n \tag{2.4}$$

$$^{28}Si + {}_0^1 n\,(14\,MeV) \rightarrow ({}^{28}Si)^*\,(78\,MeV) + {}_0^1 n \tag{2.5}$$
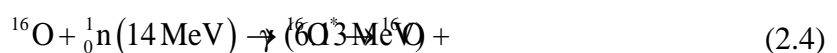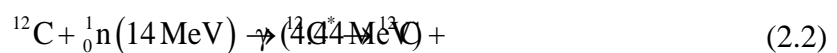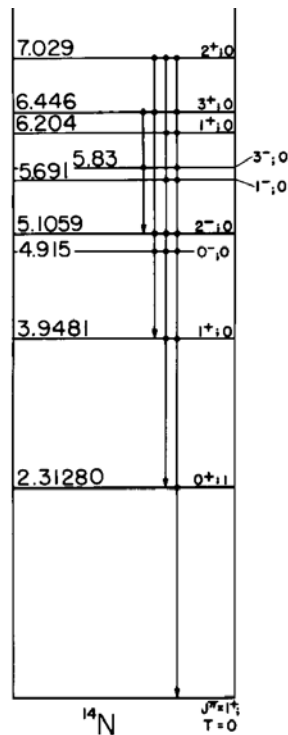
Figure 2.1 Gamma-ray decay scheme of ^{14}N which under gone inelastic scattering with a fast neutron.

2.1.3 Radiative Capture

In this reaction, the neutron is captured by the nucleus, and one or more gamma-ray are emitted from the nucleus. It is the exothermic reaction and is denoted by the symbol (n, γ). This reaction is an example of a class of interaction known as absorption reactions. The following reactions are examples of radiative capture reactions taking place when neutrons interact with H and N, the landmine's constituents

$$^{1}H + {}_{0}^{1}n\left(thermal\right) \rightarrow \gamma^{2}(2.22\,MeV)$$ (2.6)

$$^{14}N + {}_{0}^{1}n\left(thermal\right) \rightarrow \gamma^{15}(10.83\,MeV)$$ (2.7)
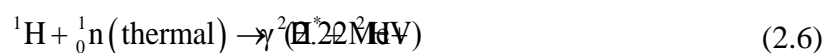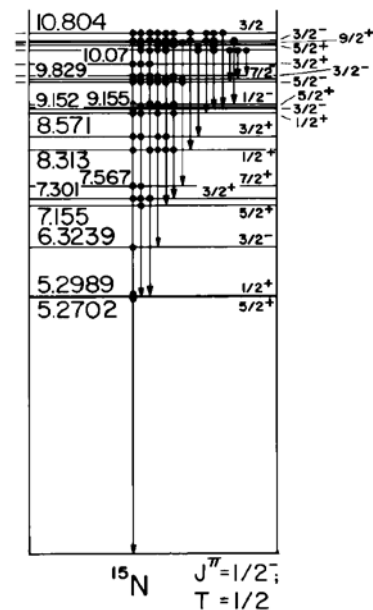
Figure 2.2 Gamma-ray decay scheme of ^{14}N which under gone radiative capture with a thermal neutron.

2.1.4 Neutron-Producing Reaction

In this reaction, when the energetic neutron strikes the nucleus it is absorbed by the nucleus and one or more neutrons is ejected from the nucleus. It is therefore considered as the endothermic reaction with can be denoted by the symbol (n, xn). For the reaction that two or three neutrons are ejected, the reaction symbols will be (n, 2n) and (n, 3n) respectively.

2.1.5 Charged-Particle Reaction

Charge-particle reaction is similar to neutron-producing reaction in which the striking neutron is disappeared while the charged-particle is emitted. Two examples of this reaction are (n, p) and (n, α). This reaction can be either endothermic or exothermic reactions.

2.1.6 Fission Reaction

In fission reaction, the nucleus is split apart while the colliding neutron disappeared. However, two to three neutrons are ejected from the nucleus. This reaction is the principal source of nuclear energy for practical application.

2.2 Neutron Cross Section

Each of the reactions described in Section 2.1 by which neutrons interact with nuclei is described by the characteristic cross section. This cross section represents the probability for each reaction type to occur when neutrons interact with matters. Thus elastic scattering is described by the elastic scattering cross section, σ_s; inelastic scattering is described by the inelastic scattering cross section, σ_I; radiative capture is described by the capture cross section, σ_γ; fission reaction is described by the fission cross section, σ_f; etc. The sum of all possible interactions is described by the total cross section, σ_t. Thus,

$$\sigma_t = \sigma_{Is} + \sigma_f + \sigma_\gamma + \sigma + \ldots \qquad (2.8).$$

The total cross section represents the probability that an interaction of any type will occur when neutrons strike the target. The absorption cross section which is the sum of cross sections of all absorption reactions is then given by

$$\sigma_a = \sigma_f + \sigma_\gamma \qquad (2.9).$$

Neutron cross sections depend strongly on the energy of the neutron as well as on the atomic weight and atomic number of the target nucleus. Figure 2.1 and Figure

2.2 Show the total cross sections for ^{27}Al and ^{238}U over the same energy region.
Notice the vast difference between the two cross sections both in terms of their
variation with energy and their magnitude in barns. All available information about
cross sections as a function of energy for all isotopes is contained in the Evaluated
Nuclear Data Files (ENDF) stored at the Brookhaven National Laboratory, Upton,
New York. The cross sections used for the MCNP simulations in this thesis are the
cross sections from ENDFB-5 which stored in the MCNP-code's data files. Table 2.1
Shows the cross section data used in this thesis.
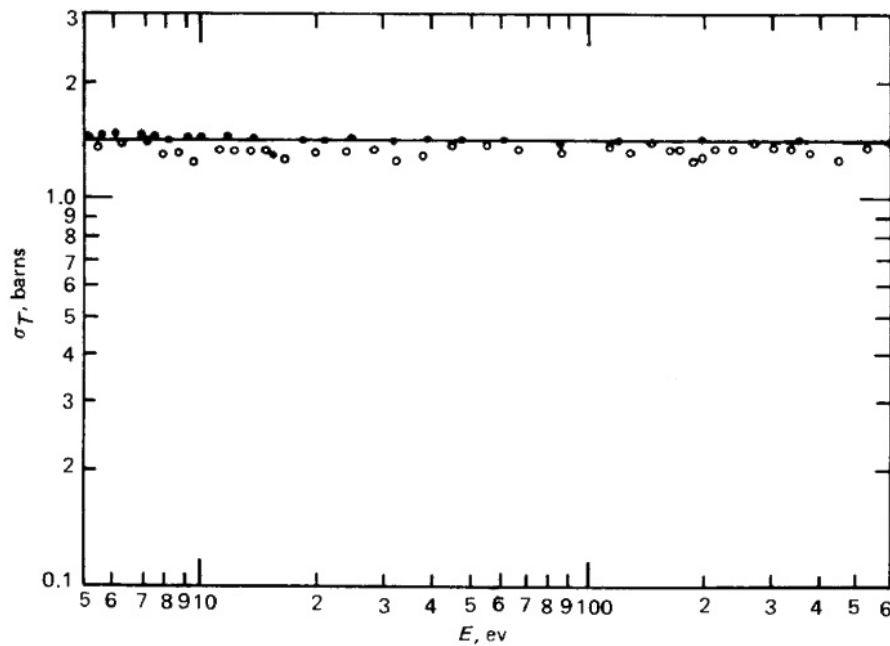
Figure 2.3   The total neutron cross section of ^{27}Al from 5 eV to 600 eV (from BNL-
325).
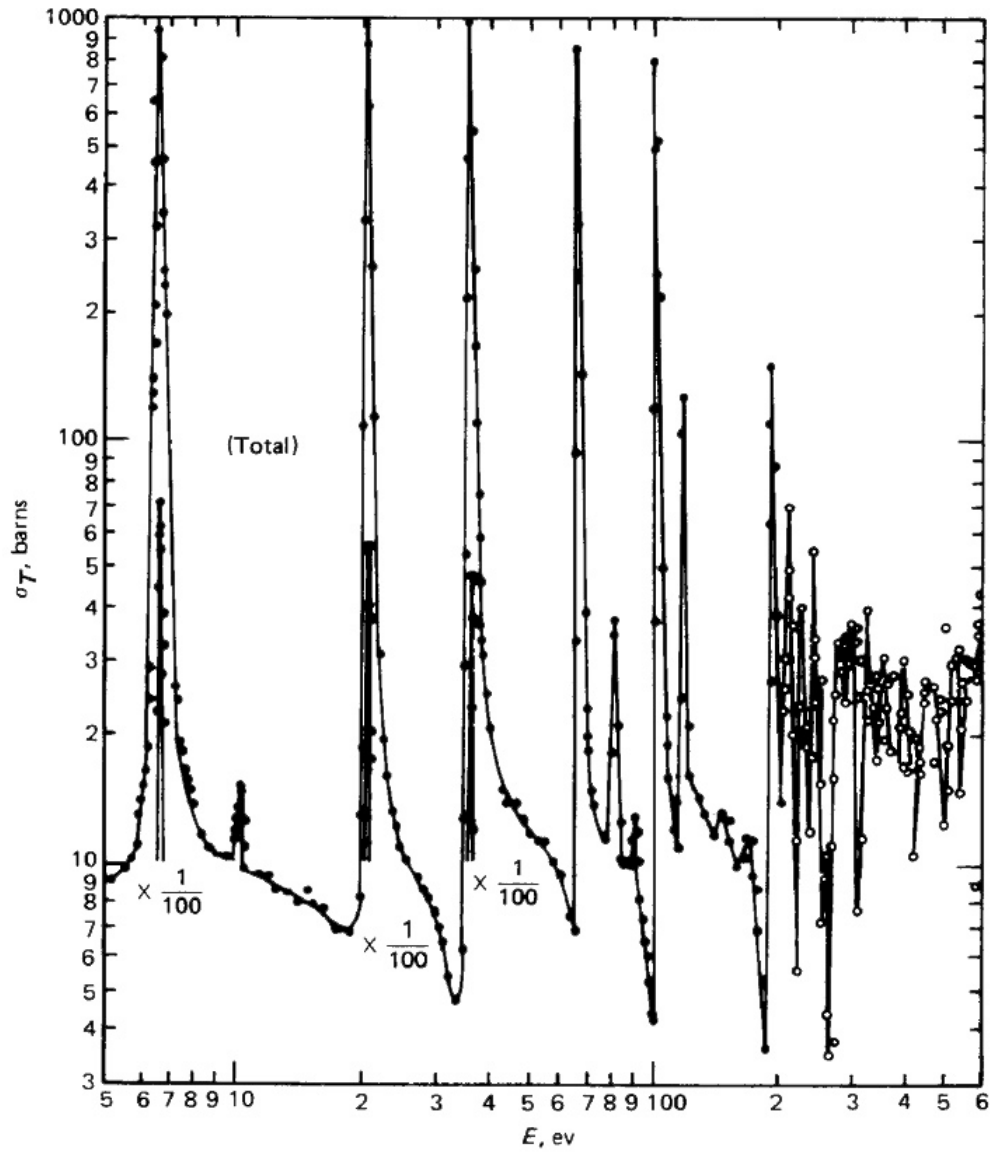
Figure 2.4 The total cross section of ^{238}U from 5 eV to 600 eV (from BNL-325).

Table 2.1 Gamma-ray cross sections of the elemental neutron interaction (Simakovl et al., 1998; Choi et al., 2006).

Eγ(MeV)	Element	Reaction Type	σγ(b)
0.9	O	$^{16}O(n, n'\gamma)^{16}O$	0.005-0.006
1.28	Si	$^{28}Si(n, \gamma)^{29}Si$	0.029
1.63	N	$^{14}N(n, n'\gamma)^{14}N$	0.030
1.59	Si	$^{28}Si(n, n'\gamma)^{28}Si$	0.024
1.78	Si	$^{28}Si(n, n'\gamma)^{28}Si$	0.293-0.471
2.09	Si	$^{28}Si(n, \gamma)^{29}Si$	0.033
2.13	N	$^{14}N(n, \alpha)^{11}B$	0.018-0.030
2.22	H	$^{1}H(n, \gamma)^{2}H$	0.333
2.23	Si	$^{28}Si(n, \gamma)^{29}Si$	0.003
2.31	N	$^{14}N(n, n'\gamma)^{14}N$	0.020-0.060
2.43	Si	$^{28}Si(n, \gamma)^{29}Si$	0.005
2.81	Si	$^{28}Si(n, n'\gamma)^{28}Si$	0.030-0.095
3.55	Si	$^{28}Si(n, \gamma)^{29}Si$	0.119
3.58	N	$^{14}N(n, \gamma)^{15}N$	0.015
4.44	C	$^{12}C(n, n'\gamma)^{12}C$	0.178-0.430
4.44	O	$^{16}O(n, n'\alpha)^{12}C$	0.027
4.94	Si	$^{28}Si(n, \gamma)^{29}Si$	0.119
5.11	N	$^{14}N(n, n'\gamma)^{14}N$	0.014-0.055
5.28	N	$^{14}N(n, \gamma)^{15}N$	0.005
6.13	O	$^{16}O(n, n'\gamma)^{16}O$	0.180
6.38	Si	$^{28}Si(n, \gamma)^{29}Si$	0.021
6.37	N	$^{14}N(n, \gamma)^{15}N$	0.015
6.92	O	$^{16}O(n, n'\gamma)^{16}O$	0.033-0.050
7.12	O	$^{16}O(n, n'\gamma)^{16}O$	0.022-0.064
10.83	N	$^{14}N(n, \gamma)^{15}N$	0.011

2.3   Gamma-Ray Interaction with Matter and Response Function

of Gamma-Ray Detectors

There are three mechanism of gamma-ray interactions with matters which have real significance in gamma-ray spectroscopy; photoelectric absorption, Compton scattering and pair production. The following sections briefly discuss about the characteristic of these mechanism. The detailed discussion is referred to Radiation Detection and Measurement, Second Edition (Knoll, 1989).

2.3.1   Photoelectric Absorption

Photoelectric absorption is an interaction in which the incident gamma-ray photon disappears and a photoelectron is ejected from one of the atomic electron shells of the target atom. The kinetic energy of this electron is equal to the incident photon energy hν minus the binding energy of the electron in its original shell (E_b). The diagram below shows the photoelectric process in which, for typical photon energies, the photoelectron is most likely be ejected from the K-shell.
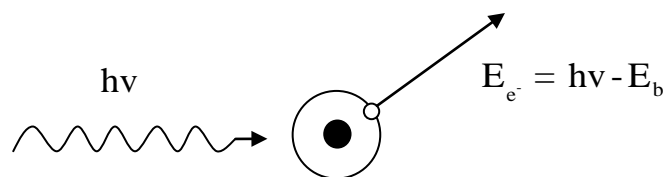
The vacancy that is created in the atomic shell is rapidly filled by electron rearrangement, in which, the binding energy is liberated either in the form of a characteristic X-ray or Auger electron. While the Auger electrons have extremely short range, the characteristic X-rays may travel some distance before being absorbed

through photoelectric absorption with less tightly bound electron shells of the target atoms. If these X-rays are fully absorbed without any escape, the effect of photoelectric absorption is the liberation of a photoelectron which carries off most of the gamma-ray energy, together with one or more of low-energy electrons corresponding to absorption of the original binding energy of the photoelectron.

If all of these electrons do not escape from the detector, the sum of all electron's kinetic energies that are created must equal to the original energy of the gamma-ray photon. Therefore, photoelectric absorption is an ideal process for measuring the energy of the original gamma-ray because the total electron kinetic energy equals to the incident gamma-ray energy. Under these conditions, the differential distribution of electron kinetic energy for a series of photoelectric absorption events would be simple delta function as shown in the diagram below. The single peak appears at the total electron energy corresponding to the energy of the incident gamma-rays.

2.3.2 Compton Scattering

Compton scattering is an interaction in which a recoil electron and the scattered gamma-ray photon are created after the incidence of the gamma-ray on the target as shown in the diagram below. The energy of the incident gamma-ray will be divided between the recoil electron and scattered photon according to the scattering angle.

In term of the scattering angle, θ, the energy of the scattered gamma-ray is given by

$$h\nu' = \frac{h\nu}{1+(h\nu/m_0c^2)(1-\cos\theta)} \tag{2.10},$$

where m_0c^2 is the electron's rest mass energy. Therefore, the kinetic energy of the scattered photon is given by

$$E_{e^-} = h\nu - h\nu' = h\nu\left(\frac{(h\nu/m_0c^2)(1-\cos\theta)}{1+(h\nu/m_0c^2)(1-\cos\theta)}\right) \tag{2.11}.$$

There are two extreme cases of Compton scattering which can be identified from these two equations:

1) A grazing angle scattering ($\theta \approx 0$). In this extreme, Eqs. (2.10) and (2.11) give $h\nu' \approx h\nu$ and $E_e \approx 0$, where the recoil Compton electron has little energy while

the scattered gamma-ray has nearly the same energy as the incident gamma-ray.

2) A head-on collision ($\theta \approx \pi$). In this case, the incident gamma-ray is back-scattered toward its original direction, while the electron recoils along the direction of the incident gamma-ray. This extreme represents the case where maximum energy that can be transferred to an electron in a single collision. For this extreme, Eqs. (2.11) and (2.12) becomes,

$$h\nu'\big|_{\theta=\pi} = \frac{h\nu}{1+2h\nu/m_0c^2} \qquad (2.11).$$

$$E_{e^-}\big|_{\theta=\pi} = h\nu\left(\frac{2h\nu/m_0c^2}{1+2h\nu/m_0c^2}\right) \qquad (2.12).$$

Basically, all scattering angles can occur in the detector in which the continuum of energies ranging from zero to the maximum predicted by Eqs. (2.12) can be transferred to the electron. For specific gamma-ray energy, the distribution of electron energy and the incident gamma-ray energy has the general shape as shown in the diagram below.
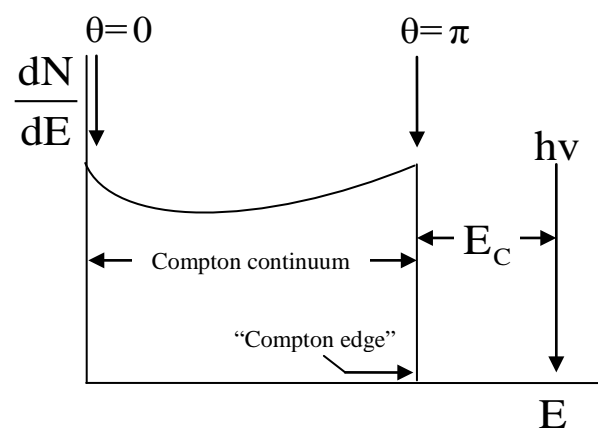
The gap between the maximum Compton recoil electron energy and the incident gamma-ray energy is given by

$$E_C = h\nu - E_{e^-}\Big|_{\theta=\pi} = \frac{h\nu}{1+2h\nu/m_0c^2} \qquad (2.13).$$

2.3.3 Pair production

Pair production is the third gamma-ray interaction process that occurs in the field of the target nucleus. This process corresponds to the creation of electron-positron pair at the point of complete disappearance of the incident gamma-ray photon. The minimum energy of the incident gamma-ray photon required for creation of electron-positron pair is 1.02 MeV (equal to $2m_0c^2$). If the incident gamma-ray energy exceeds this value, the excess energy will be shared in the form of kinetic energies of electron-positron pair. Therefore, pair production is the process that converts the incident gamma-ray energy into the kinetic energies of electron-positron pair with the total of,

$$E_{e^-} + E_{e^+} = h\nu - 2m_0c^2 \qquad (2.14).$$

Typically, both electron and positron will travel for a few millimeters at most before losing all their kinetic energies to the target nucleus. A plot of the total kinetic energies of electron-positron pair created by the incident gamma-ray is again the simple delta function, but it is now appeared at $2m_0c^2$ below the incident gamma-ray energy, as shown in the diagram below. This amount of energy will be deposited each time the pair production occurs within the detector. This energy will correspond to the position of double escape peak in the actual gamma-ray pulse height spectra.

$$\frac{dN}{dE}$$
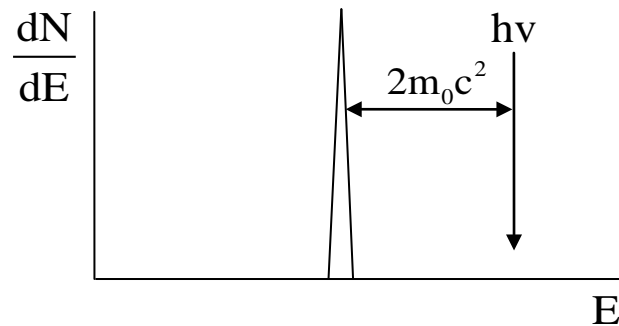
The pair production process is complicated due to the fact that the positron is not a stable particle. Once its kinetic energy becomes very low the positron will annihilate or combine with a normal electron in the target medium. At this point both disappear, and they are replaced by two annihilation photons of energy m_0c^2 (0.511 MeV) each. Since the time for positron to slow down is small, therefore the annihilation radiation will be in coincidence with the original pair production interaction.

2.4   Predicted Response Function of Gamma-Ray Detector

Since the expected response function of gamma-ray detectors depends on the detector size, the following sections discuss about the response function of gamma-ray detectors based on the detector size.

2.4.1   Small Detectors

If the detector size is small when compared with the mean free path of the secondary gamma radiation produced in interactions of the original gamma-rays, it is classified as the small detector. Because the mean free path of secondary gamma-rays is typically of the order of several centimeters, the condition of "smallness" is met if

the detector dimension does not exceed 1 or 2 cm. For small detectors, all charge particle energy (photoelectron, Compton electron, pair electron and positron) is completely absorbed within the detector volume. Figure 2.5 shows the predicted electron energy deposition spectra under these conditions.
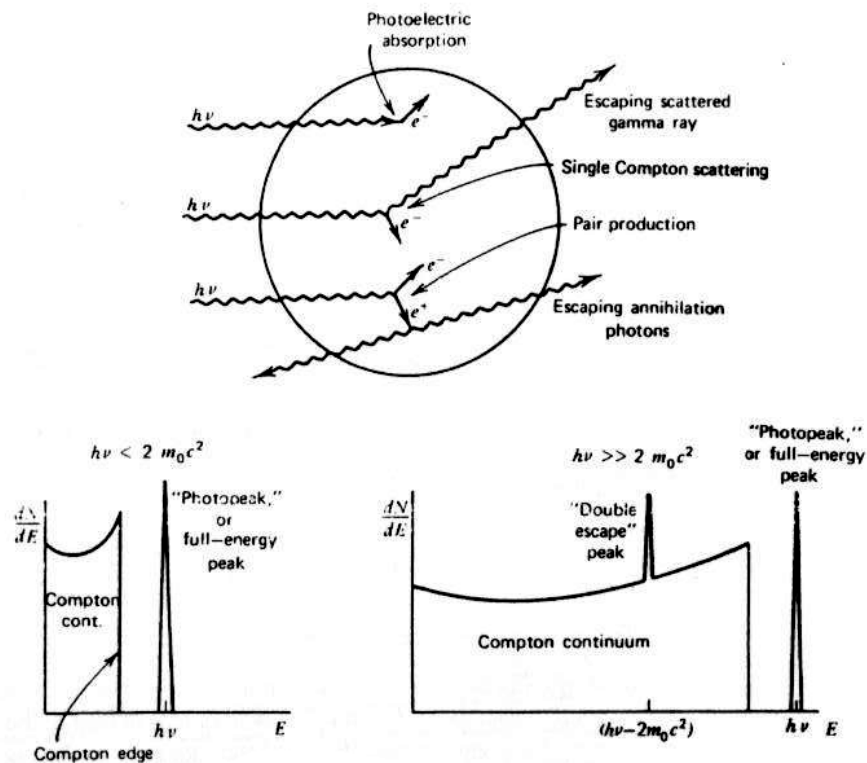
Figure 2.5 The "small detector" extreme in gamma ray spectroscopy. The processes of photo electric absorption and single Compton scattering give rise to the low-energy spectrum at the left. At higher energies, the pair production process adds a double escape peak shown in the spectrum at the right (Knoll, 1989).

If the incident gamma-ray energy is below the value at which pair production is significant, the spectrum contains only the effect of Compton scattering and photoelectric absorption. The continuum corresponding to Compton scattered

electrons is called the Compton continuum and the narrow peak corresponding to photoelectron is called the photopeak. If the incident gamma-ray energy is sufficiently high (several MeV), the results of pair production are also appear in the electron energy spectrum. For a small detector, only the electron and positron kinetic energies are deposited, and the annihilation radiation escapes. The net effect is to add a double escape peak to the spectrum located at an energy of $2m_0c^2$ (1.02 MeV) below the photopeak.

2.4.2 Very Large Detector

The very large detector is the opposite extreme case of gamma-ray detectors. The dimension of this detector is assumed to be sufficiently large so that all secondary radiations, including Compton scattered gamma-ray and annihilation photons, also interact within the detector active volume and none escapes from the surface. For typical energies, this condition would imply that the detector dimension on the order of many tens of centimeters is required.

For such very large detector, the response function is very simple. Some typical histories, obtained by following a particular source gamma-ray and all subsequent secondary radiation, are sketched in Figure 2.6. If the initial interaction is a Compton scattering event, the scattered gamma-rays will subsequently interact at some other location with the detector. The second interaction may also be a Compton scattering event, in which case a scattered photon of still lower energy is produced. Eventually, a photoelectric absorption will occur and the history is terminated at that point. For this detector, the time required for entire histories to take place is small. The time required for primary and secondary gamma-rays travel with speed of light in

the detector medium will be less than nanosecond which is less than the inherent response time of virtually all practical detectors used in gamma-ray spectroscopy. Therefore, the net effect is to create the Compton electrons at each scattering point and the photoelectron in time coincidence. The pulse produced by the detector will therefore be the sum of the responses due to each individual electron. The detector response is therefore the same as if the original gamma-ray photon had undergone a simple photo electric absorption in a single step.

For the very large detector, the response function will consist of a single peak as shown in Figure 2.6 Rather than the more complex function as shown in Figure 2.5.
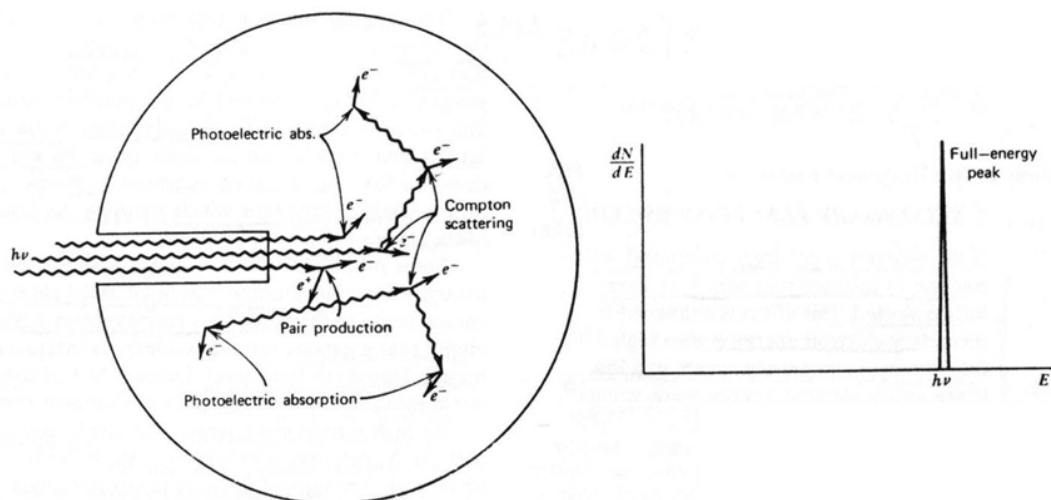
Figure 2.6   The "large detector" extreme in gamma ray spectroscopy. All gamma-ray photon, no matter how complex their mode of interaction, ultimately deposit all their energy in the detector. Some representative histories are shown at the top (Knoll, 1989).

2.4.3 Intermediate Size Detector

Real detectors in common use for gamma-ray spectroscopy have sizes neither small nor large by the above standard. For usual geometries in which the gamma-rays are incident externally on the surface of the detector, even large-volume detector appear finite because some interactions will take place near the entrance surface. The response functions of normal detectors, therefore, combine some of the properties discussed for the two previous cases, as well as additional features related to partial recovery of the secondary gamma-ray energy. Figure 2.7 shows some representative histories that illustrate these additional possibilities together with corresponding features response function. The spectrum for low to medium gamma-ray energies (where pair production is not significant) will consists of a Compton continuum and photopeak. In this case, the ratio of the area under the photopeak to that under the Compton continuum over that for the very small detector due to the added contribution of multiple event to the photopeak. The lower the incident gamma-ray energy, the lower will be the average energy of the Compton scattered photon. Thus , even the detectors of moderate size will appear to be large, and the relative area under the photopeak increases with decreasing incident photon energy. At medium energies, the possibilities of multiple Compton scattering followed by the escape of the final scattered photon can lead to a total energy deposition that is greater than the maximum predicted by Eq. (2.12).

For a single scattering, if the gamma-ray energy is high enough to make pair production significant, a more complicated situation prevails. The annihilation photon now may either escape or undergo further interaction within the detector. These additional interactions may lead to either partial or full-energy absorption of either

one or both of annihilation photon. The response function to be expected for a real gamma-ray detector will, therefore, depend on size, shape, and composition of the detector, and also on the geometric detail of irradiation conditions. For example, the response function will change some what if the point gamma-ray source is moved from a position close to the detector to one that is far away.
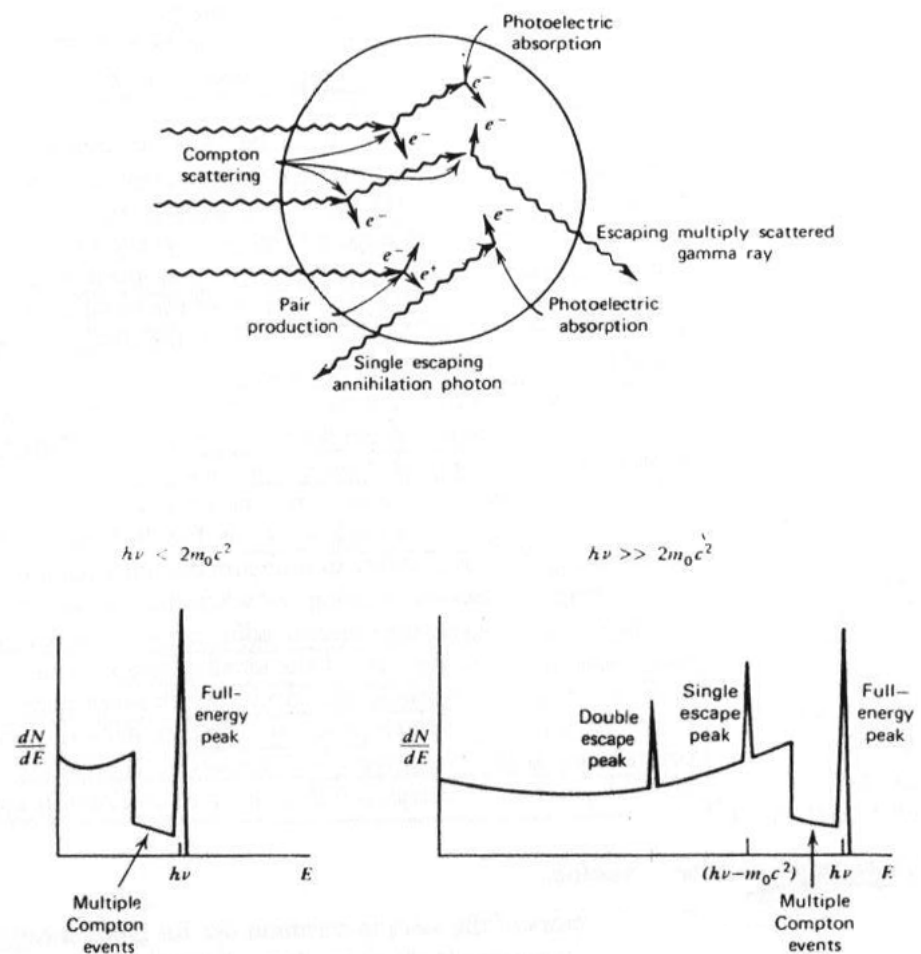
Figure 2.7 The case of intermediate detector size in gamma ray spectroscopy. In addition to the continuum from single Compton scattering and the full-energy peak, the spectrum at the left shows the influence of multiple Compton event follow by photon escape. The full energy peak also contains some histories that began with

Compton scattering. At the right, the single escape peak corresponds to initial pair production interaction in which only one annihilation photon leaves the detector without future interaction. A double escape peak as illustrated in Figure 2.5 will also be present due to those pair production events in which both annihilation photons escape (Knoll, 1989).

CHAPTER III

MCNP SIMULATION OF LANDMINE DETECTION BY

USING NUCLEAR TECHNIQUE

Since the main part of this thesis involves using MCNP to simulate the landmine detection by using nuclear techniques, the brief description of MCNP is discussed first. The later involves the discussion of the simulation of landmine detection by using nuclear techniques.

3.1   Introduction to MCNP

MCNP is a general-purpose particle (or Monte Carlo N-Particle) transport code, where N represents neutron, photon, electron or combination of them. It can be used to simulate the transport of neutrons of energy from 10^{-11}-20 MeV, and photons and electrons of energy from 1 keV-1,000 MeV. In solving a problem, MCNP uses the statistical process to simulate the transport of individual particles and record some aspects of their average behavior that can be inferred to be the average behavior of the particle in the physical system. For the problem of interaction of nuclear particles with matters, the individual probabilistic events that comprise a process are simulated sequentially and the probability distribution governing these events is statistically sampled to describe the total phenomenon. In using MCNP for calculation, the user must create an input file which contains information about the geometry specification,

the source definition, the material description, the selection of cross section evaluations and the type of answer and tally desired.

3.2   The Monte Carlo Method

In solving the problem, MCNP uses the statistical Monte Carlo method in which the individual probabilistic events that comprise a process are simulated sequentially. The probability distribution governing these events are statistically sampled to describe the total phenomenon based on the selection of random numbers, which is analogous to throwing dice in a famous gambling casino, name "Monte Carlo". In particle transport, MCNP follows each particle, from its birth after releasing from source, throughout its life when it is absorbed in or escaped from the system. Probability distributions of its transport are randomly sampled until the outcome at each step of its life has been scored. Figure 3.1 shows the random history of a neutron incident on a bulk of sample as an example of the particle transport. Numbers between 0 and 1 are selected randomly to determine what, if any, and where interaction takes place, based on the physical rules and probabilities governing the processes and materials involved. In this particular example, a neutron collision occurs at event 1 is scattered in the direction shown, which is selected randomly from the physical scattering distribution. A photon is also produced in that event and is temporarily stored in a certain memory location for later analysis. At event 2, a slowing down neutron has been completely captured and produced one photon which leaks out at event 3. The remaining photon generated at event 1 is now followed with a capture at event 4. As a rule, MCNP retrieves stored particles such that the last particle stored in the memory is the first particle taken out, in which, its history is now complete. As

more and more such histories are followed, the neutron and photon distributions become better known. The quantities of interest which the user requests are tallied, along with estimates of the statistical precision or uncertainty of the results. From this concept we can see that the accuracy of an estimate quantity tends to improve as one average over larger and larger samples of the quantity.
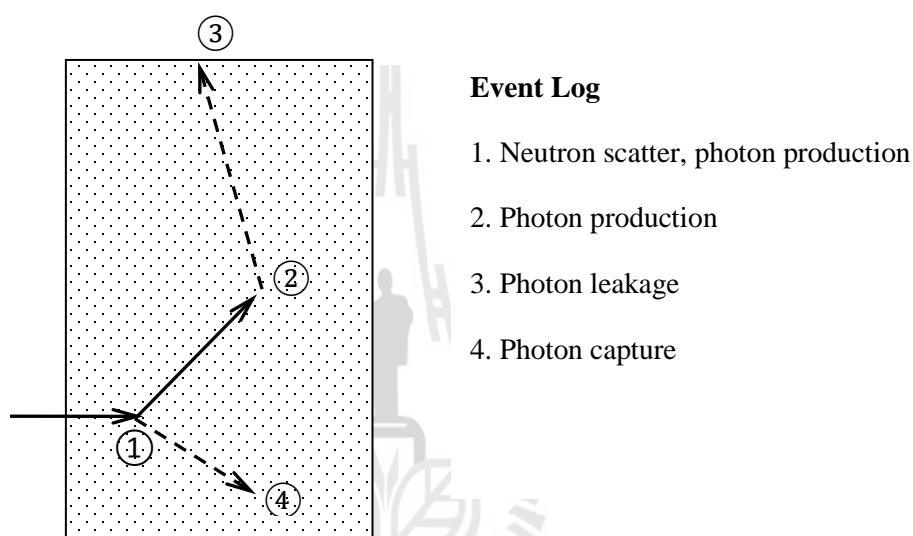
Figure 3.1   The random history of a neutron incident on a bulk of sample as an example of the particle transport, solid line are neutron and dash line are photon.

3.3   MCNP Features

There are many features in MCNP that the user should know. These features include nuclear data and reactions, source specification, tally and output, estimation of error, and variance reduction technique. The details of these features can be obtained from MCNP's manual (X-5 Monte Carlo Team, 2003).

3.4 MCNP Geometry

The geometry of MCNP is treated with an arbitrary three-dimensional configuration of user-defined materials in geometric cells bounded by first- and second-degree surfaces and fourth-degree elliptical tori. The cells are defined by the intersections, unions, and complements of the regions bounded by the surfaces. Surfaces are defined by supplying coefficients to the analytic surface equations or, for certain types of surfaces, known points on the surfaces. MCNP also provides a macro body capability, where basic shapes such as spheres, boxes, cylinders, etc., may be combined using Boolean operators. MCNP has a more general geometry than is available in most combinatorial geometry codes. In addition to the capability of combining several predefined geometrical bodies, as in a combinatorial geometry scheme, MCNP gives the user the added flexibility of defining geometrical regions from all the first- and second degree surfaces of analytical geometry and elliptical tori and then of combining them with Boolean operators. The details of cell and surface definitions are discussed in MCNP's manual. The reader is recommended to read them from MCNP's manual.

3.5 MCNP Input

The main input file for the MCNP's user is INP (the default name). The INP input file consists of a deck of input cards which contains the input information to describe the problem. Below is the form of the deck of input cards, in which, the detailed specification of all input cards are discussed in Chapter III and summarized in Table 3.8 starting on page 3148 of the MCNP user manual. The form of an input file of MCNP is as follow:

Message Block (optional)

Blank Line Delimiter (optional)

One Line Problem Title Card

Cell Cards

::

Blank Line Delimiter

::

Surface Cards

::

Blank Line Delimiter

Data Cards

::

Blank Line Terminator (optional)

The units used for variables in the input cards are as follow:

1. lengths in centimeters,

2. energies in MeV,

3. times in shakes (10^{-8} sec),

4. temperatures in MeV (kT),

5. atomic densities in units of atoms/barn-cm,

6. mass densities in g/cm^3,

7. cross sections in barns (10^{-24} cm^2),

8. heating numbers in MeV/collision, and

9. atomic weight ratio based on a neutron mass of 1.008664967 amu. In these units, Avogadro's number is $0.59703109 \times 10^{24}$.

An example of the input file for the simulation of the TNT-landmine detection by NaI(Tl) gamma-ray detector is shown below. In this example, ^{252}Cf is used as the neutron source which produces neutrons with the Watt fission energies, ranging from 0-14 MeV. The anti-tank landmine, burying under sand-formation at 5 cm deep, has diameter of 16.7 cm and height of 6 cm. Its density is 1.65 g/cm^3. The gamma-ray detector has diameter of 12.7 cm and height of 12.7 cm. There are two types of gamma-ray tallies requested by the user: the track length estimate of cell flux (F-4 tally) and the energy distribution of pulses created in the detector (F-8 tally). The geometry model used for the simulation has cylindrical shape with dimensions as discussed in Section 3.6.

```
c CYLINDRICAL MODEL
c cell cards
1 3 -3.67 -7 5 -6 imp:n,p=1
2 4 -11.35 7 -8 4 -6 imp:n,p=1
3 2 -1.65 -10 11 -12 imp:n,p=1
4 5 -2.12 -1 2 -9 #3 imp:n,p=1
5 1 -0.0013 1 -3 -9 #1 #2 imp:n,p=1
6 0 -13 #1 #2 #3 #4 #5 imp:n,p=1
7 0 13 imp:n,p=0
c end of cell cards for sample problem
blank line delimiter
c surface cards
1 pz 1
```

2 pz -40

3 pz 60

4 pz 19

5 pz 20

6 pz 32.7

7 cz 6.35

8 cz 8.35

9 cz 30

10 pz -5

11 pz -12.75

12 cz 10

13 so 70

c end of cube surface

blank line delimiter

c mode card

MODE n p

c material cards

m1 8016 -0.000301 7014 -0.000976 $air (d=0.0013 g/cm^3)

m2 6012 0.02 1001 0.37 7014 0.19 8016 0.42 $TNT (C7H5N3O6 d=1.65 g/cm^3)

m3 11023 0.4995 53127 0.4995 $ detector (NaI(Tl) d=3.67 g/cm^3)

m4 82207 1 $Pb -11.35

m5 14000 0.47 8016 0.53 $Sand (SiO2 d=2.12 g/cm^3)

c source definition

sdef pos= 0 0 5 erg=d1 dir=-1 vec= 0 0 1 par=1

si1   0.01e-6 0.025e-6 1e-6 1 24i 14

sp1   -3   1.025   2.926

f4:n 3

 e04 0 2.5e-8 1.0e-6 5.0e-6 1.0e-5 1.0e-4 1.0e-3 1024i 12

f14:p 1

 e14 0 2.5e-8 1.0e-6 5.0e-6 1.0e-5 1.0e-4 1.0e-3 1024i 12

f28:p 1

 ft28 geb 2.5e-3 55.05e-3 0.52365e-6

 e28 0 2.5e-8 1.0e-6 5.0e-6 1.0e-5 1.0e-4 1.0e-3 1024i 12

nps 5e8

blank line delimiter (end of optional)

All input lines are limited to 80 columns. Alphabetic characters can be upper, lower, or mixed case. A $ (dollar sign) terminates data entry on a line. Anything on the line that follows the $ is interpreted as a comment. Blank lines are used as delimiters and as an optional terminator. Data entries are separated by one or more blanks.

Cell Cards

The cell number is the first entry and must begin in the first five columns. The next entry is the cell material number, which is arbitrarily assigned by the user. The material is described on a material card (Mn) that has the same material number. If the cell is a void, a zero is entered for the material number. The cell and material numbers cannot exceed 5 digits each. Next is the cell material density. A positive entry is interpreted as atom density in units of 10^{24} atoms/cm^3. A negative entry is interpreted

as mass density in units of g/cm^3. No density is entered for a void cell. A complete specification of the geometry of the cell follows. This specification includes a list of the signed surfaces bounding the cell where the sign denotes the sense of the regions defined by the surfaces. The regions are combined with the Boolean intersection and union operators. A space indicates an intersection and a colon indicates a union. Optionally, after the geometry description, cell parameters can be entered. The form is keyword=value. The following line illustrates the cell card format:

1 3 -3.67 -7 5 -6 imp:n,p=1

Cell 1 is formed by the intersection of the region inside cylindrical (negative sense) surface 7 with the region to above (positive sense) of surface 5, intersected with the region below (negative sense) surface 6 and this cell contains material 3 with density 3.67 g/cm^3, are bounded by surfaces 7, 5, 6 and has an importance of 1. If cell 1 were a void, the cell card would be

1 0 -7 5 -6 imp:n,p=1

Surface Cards

The first- and second-degree surfaces plus the fourth-degree elliptical and degenerate tori of analytical geometry are all available in MCNP. The surfaces are designated by mnemonics such as C/Z for a cylinder parallel to the z-axis. A cylinder at an arbitrary orientation is designated by the general quadratic (GQ) mnemonic. A paraboloid parallel to a coordinate axis is designated by the special quadratic (SQ) mnemonic. A planes normal to axes (PX, PY, or PZ), the definition gives positive sense for points with x, y, or z values exceeding the intercept of the plane, The following line illustrates the surface card format:

5 pz 20

This describes a plane normal to the z-axis at z = 20 with positive sense for all points with z > 20, and 5 is the surface number. The 29 mnemonics representing various types of surfaces are listed in Table 3.1 on page 3-13 of the MCNP user manual.

3.6   Geometry Models for the Simulation

In using MCNP for the simulation of a physical system, the geometry model of the simulation must be specified. There are two types of geometry models used for the simulations in this thesis.

3.6.1 Spherical Model

1. Void
2. Single-element
3. Void/air
4. Spherical detector

.S   Point source
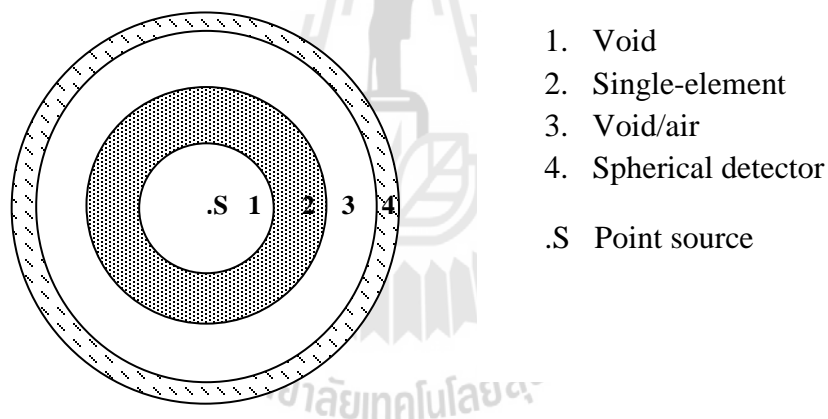
Figure 3.2 Spherical Geometry Models.

Figure 3.2 shows the spherical geometry model. In this model, the source (labeled .S) locates at the center of the model, while the single-element (labeled 2), which surrounds the source, locates between the inner void (labeled 1) and the outer void (labeled 3). At the outermost of the model is the position of the spherical detector (labeled 4). The thicknesses of both the inner and outer voids are 10 cm, while, the thicknesses of the target and the detector are 10 cm and 5 cm, respectively. The

objective of this model is to increase the detection efficiency of the gamma-ray detector which has spherical shape enclosing the radioactive source and target. Any gamma rays originated from the radioactive source would be detected by the detector with very high efficiency. This model should guarantee that all types of gamma-rays induced from the interaction between the neutron and the target material are detected by the gamma-ray detector. The simulation results should allow us to investigate that all of the resulted gamma-ray energies agree with those of theory.

3.6.1 Cylindrical Model
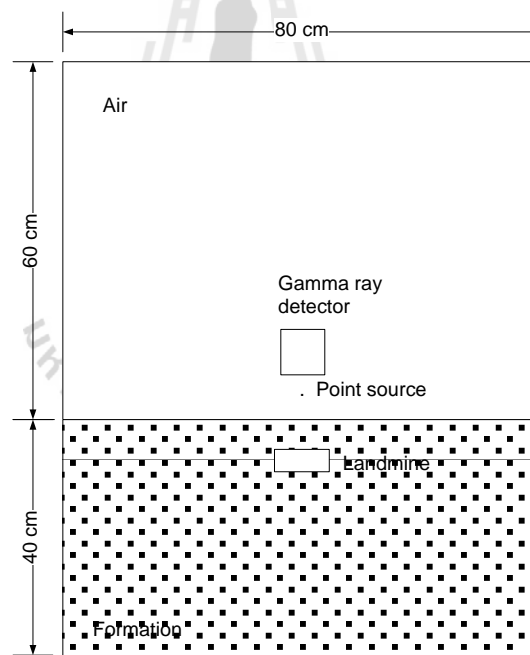
Figure 3.3 Cylindrical Geometry Model.

Figure 3.3 shows the cylindrical simulation model that similar to the real model for landmine detection by using nuclear techniques. In this model, the landmine is buried at 5 cm under the formation surface. The radioactive point source, which is 5

cm below the gamma-ray detector, locates at 5 cm above the formation. While the diameter of the cylindrical model is 50 cm, the heights of the formation and the air-void are 40 cm and 60 cm, respectively.

3.7 MCNP Simulations of Landmine Detection by Using Nuclear Techniques

As mentioned earlier in this thesis, the simulation of the landmine detection by using nuclear techniques is performed by using MCNP5. Components of the simulation system consist of the type of radioactive sources, the type of gamma-ray detectors, the type of formations and the type of landmine. Since there are two types of neutron sources (^{252}Cf and ^{241}Am-^{9}Be), three types of gamma-ray detectors (NaI(Tl), BGO, LaBr$_3$:Ce), two types of ground formations (SiO$_2$, CaCO$_3$,clay) and a types of landmine (TNT) used for the simulation, the combinations of simulation components make the total number of simulations close to 100. The results of some selected simulations will be presented and discussed in Chapter IV.

CHAPTER IV

RESULTS AND DISCUSSION

In this chapter, results of MCNP simulations of the landmine detection by using nuclear technique are discussed. The simulations started with the simulations of single elements and followed by the simulations of materials. The following sections show the results of these simulations.

4.1 Simulation of Single-Element Detection

In the simulation , the detection of elemental compositions of TNT-landmine and of ground- formations (sand, calcium carbonate and clay) are simulated. These elements include hydrogen (H), carbon (C), nitrogen (N), oxygen (O), silicon (Si), aluminum (Al) and calcium (Ca). The simulations of these elements are based on using spherical-geometry model with the dimensions as specified in Chapter III. ^{252}Cf that locates at the center of the model, is used as the point-neutron source, emitting 0-14 MeV neutrons in forward direction toward the single-element direction. Each type of element is put at the single-element position, one by one, for each simulation. The hypothetical gamma-ray detector (without a crystal) has a ring shape with 5-cm thickness enclosing the gamma-ray source and target. It locates at the outermost of the model. The simulated gamma-ray output is in the form of average flux over the surface (F-2 tally). The following sections give the results of each simulation cases. Theoretical energies and cross sections of gamma-rays resulting from various neutron

interaction types with single elements are given in Table 4.1 for comparisons with those resulting from simulations.

Table 4.1 Neutron induced gamma-ray energies and cross sections for various types of neutron interactions with TNT's elemental compositions (Simakovl et al., 1998; Choi et al., 2006).

Eγ (MeV)	Reaction	σγ (b)
0.90	$^{16}O\ (n, n'\gamma)\ ^{16}O$	0.0100
1.68	$^{14}N\ (n, \gamma)\ ^{15}N$	0.0063
1.88	$^{14}N\ (n, \gamma)\ ^{15}N$	0.0147
2.13	$^{14}N\ (n, \alpha)\ ^{11}B$	0.0180
2.22	$^{1}H\ (n, \gamma)\ ^{2}H$	0.3320
2.31	$^{14}N\ (n, n'\gamma)\ ^{14}N$	0.0500
2.52	$^{14}N\ (n, \gamma)\ ^{15}N$	0.0044
3.53	$^{14}N\ (n, \gamma)\ ^{15}N$	0.0071
3.68	$^{14}N\ (n, \gamma)\ ^{15}N$	0.0115
4.44	$^{12}C\ (n, n'\gamma)\ ^{12}C$	0.180-0.430
4.51	$^{14}N\ (n, \gamma)\ ^{15}N$	0.0132
5.11	$^{14}N\ (n, n'\gamma)\ ^{14}N$	0.0620
5.28	$^{14}N\ (n, \gamma)\ ^{15}N$	0.0236
5.53	$^{14}N\ (n, \gamma)\ ^{15}N$	0.0155
6.13	$^{16}O\ (n, n'\gamma)\ ^{16}O$	0.1650
6.32	$^{15}N\ (n, \gamma)\ ^{16}N$	0.0145
6.92	$^{16}O\ (n, n'\gamma)\ ^{16}O$	0.0520
7.12	$^{16}O\ (n, n'\gamma)\ ^{16}O$	0.0640
7.30	$^{14}N\ (n, \gamma)\ ^{15}N$	0.0075
8.31	$^{14}N\ (n, \gamma)\ ^{15}N$	0.0033
10.83	$^{14}N\ (n, \gamma)\ ^{15}N$	0.0113

4.1.1 Simulation Result of Hydrogen-Detection
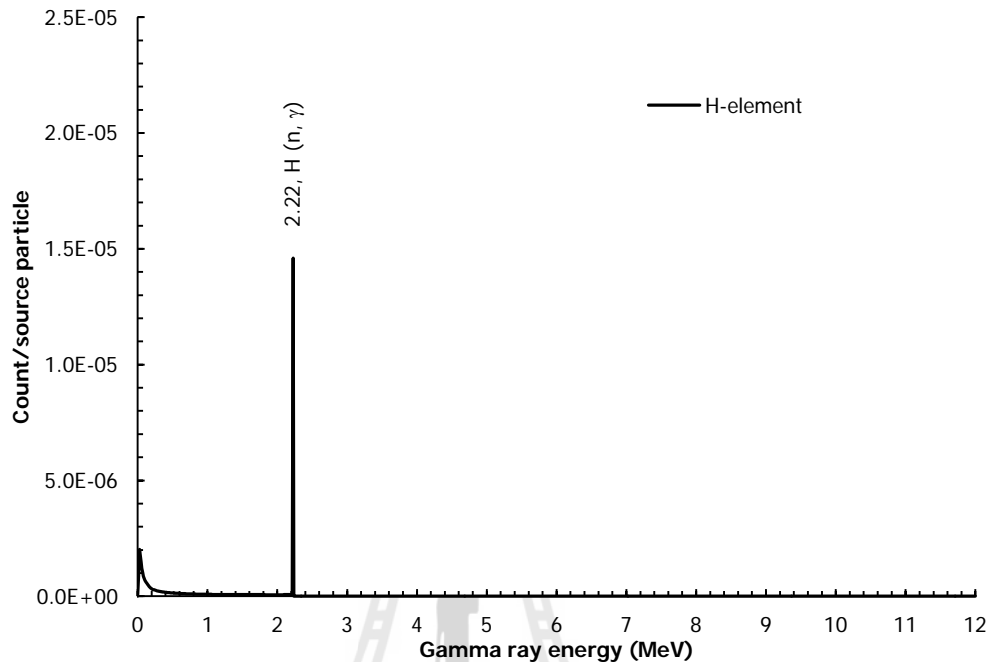
Figure 4.1 Simulated gamma-ray spectrum resulting from the detection of H.

Figure 4.1 describes the simulated spectrum resulting from the detection of H. Only the 2.22 MeV gamma-ray line with cross section of 0.332 b from the neutron-capture interaction with H, $^1H(n, \gamma)^2H$, appeared in the spectrum. This appearance illustrates that most fast neutrons emitted from the neutron source are rapidly thermalized when interact with H. This type of interaction is sometime referred to as thermal neutron activation (TNA). This simulation result agrees with theory for showing that neutrons have high elastic scattering probability with low-atomic number elements.

4.1.2 Simulation Result of Carbon-Detection
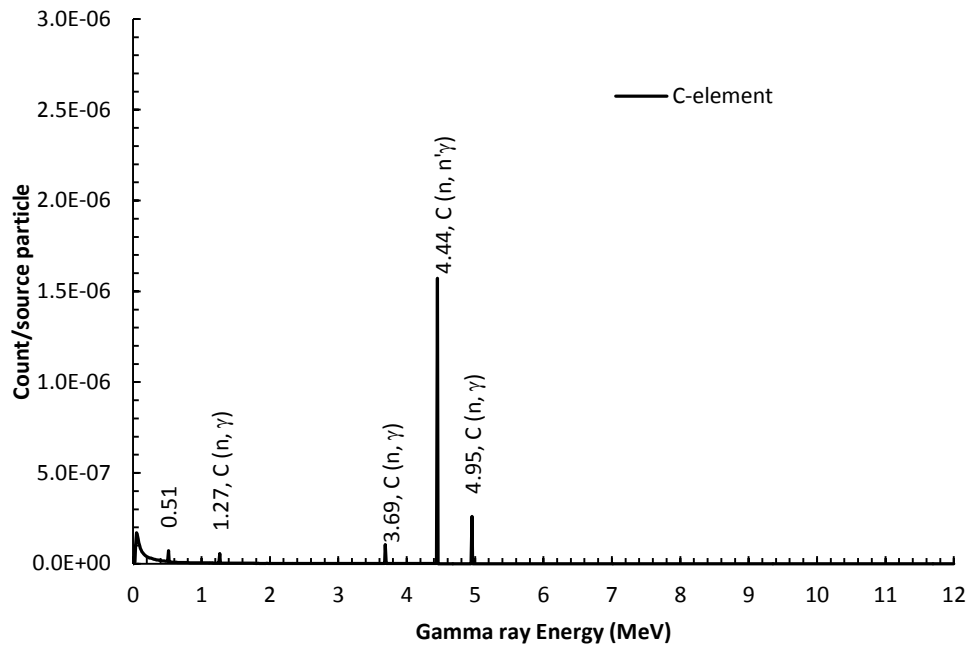
Figure 4.2 Simulated gamma-ray spectrum resulting from the detection of C.

As shown in the spectrum, the prominent 4.44 MeV gamma-ray with the cross section of 0.18 b from the neutron- inelastic interaction with C, $^{12}C(n, n'\gamma)^{12}C$, appeared in the spectrum. This type of interaction is sometime called fast neutron activation (FNA). Other neutron- capture interactions with low cross sections also occurred in the simulation as shown in Figure 4.2.

4.1.3   Simulation Result of Nitrogen-Detection
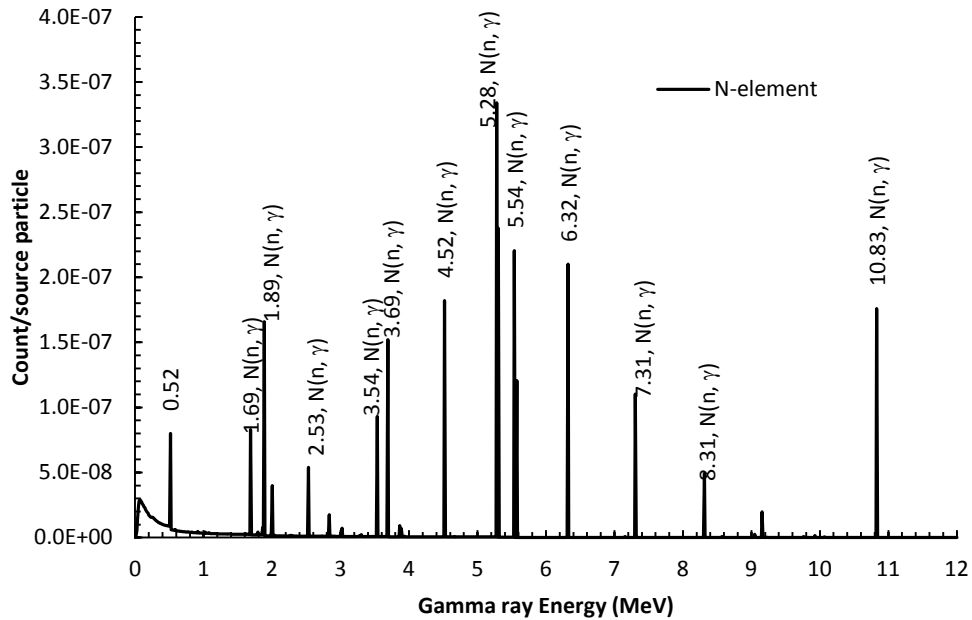
Figure 4.3 Simulated gamma-ray spectrum resulting from the detection of N with thermal (0.025 eV) neutrons.

Figure 4.3 shows the simulated results from the detection of N with thermal (0.025 eV) neutrons. The objective of this simulation is to investigate what kind of gamma-ray energies occur from the thermal neutron activation of N. As expected, the 10.83 MeV gamma-ray appeared alone at the high energy end of the spectrum. This gamma-ray line is well recognized as the most important index for the detection of landmine based on TNA technique. Some others gamma-rays with comparable cross sections to that of the 10.8 MeV also appeared on the spectrum. However, these gamma-rays locate at the energy region which may be interfered with gamma-rays resulting from the neutron activation of other TNT's elemental compositions.
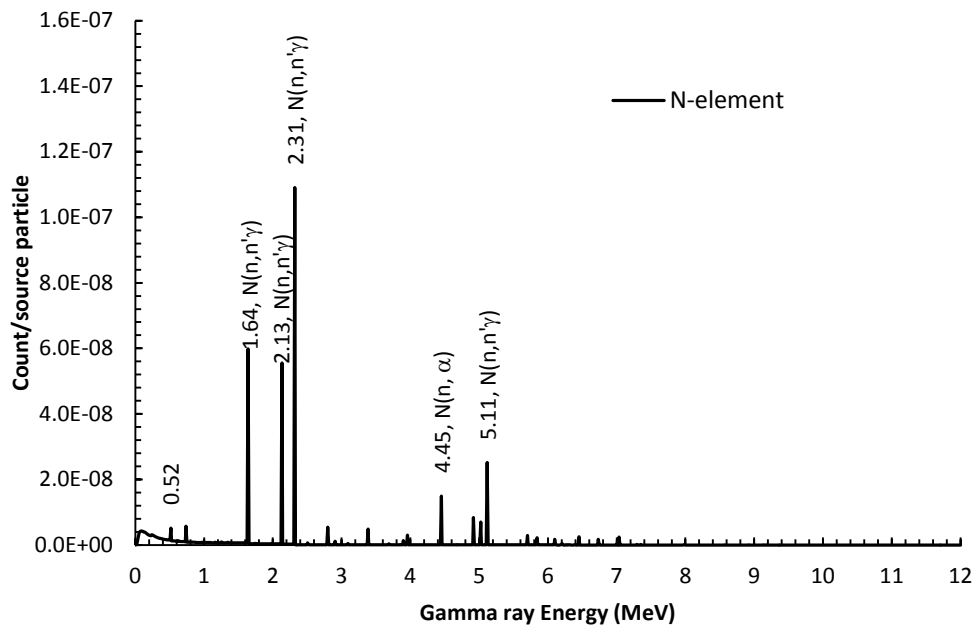
Figure 4.4 Simulated gamma-ray spectrum resulting from the detection of N with fast neutron emitted from ^{252}Cf-neutron source.

Figure 4.4 shows the gamma-ray spectrum resulting from the detection of N with fast neutrons emitted from ^{252}Cf-neutron source. Most of the gamma-rays resulting from this simulation have low cross section, except the 2.31 MeV which has energy close to the 2.22 MeV. This gamma-ray may be a source of interference of the prominent gamma-ray resulting from neutron activations of others elemental compositions of TNT-landmine. The 4.45 MeV gamma-ray from the ^{15}N (n, α)^{13}C-interaction and the 5.11 MeV gamma-rays from the ^{15}N (n, n′γ)^{15}N-interactions also appeared in the spectrum. They could also give interfering problems. Their cross section can be obtained from Table 2.1.

4.1.4 Simulation Result of Oxygen-Detection
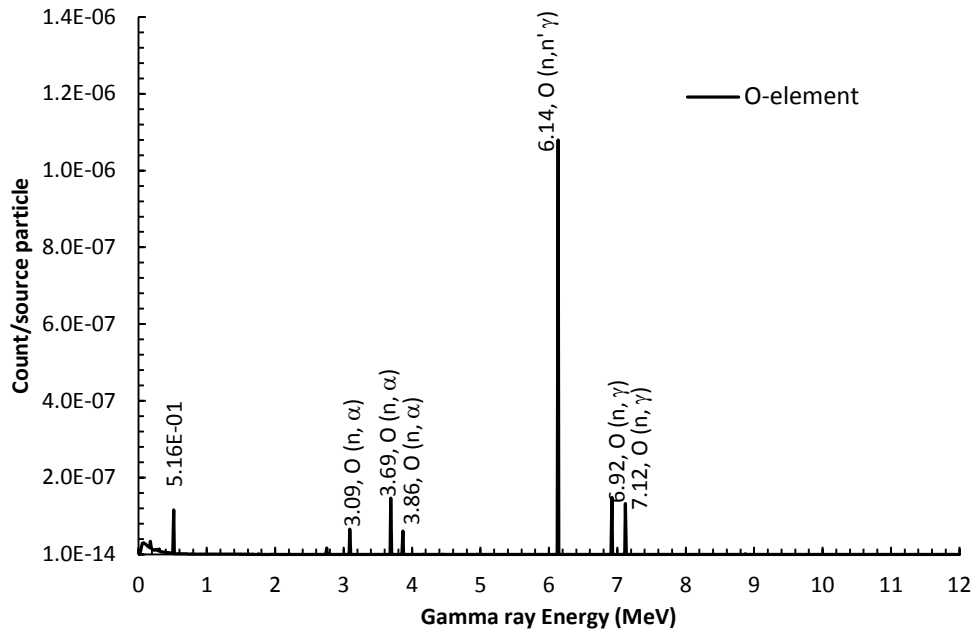
Figure 4.5 Simulated gamma-ray spectrum resulting from the detection of O.

As shown Figure 4.5, the 6.13 MeV gamma-ray appeared in the spectrum. This gamma-ray is the result of the ^{16}O (n, n$'\gamma$)^{16}O-interaction with quite high cross section as show in Table 4.1. It can give a serious interfering problem to the TNT-landmine detection because it also come from O of sand-formation. Moreover, the alpha particle-induced ^{16}O(n, α)^{12}C-interaction also appeared in the spectrum. This interaction leads to the creation of ^{12}C, which in turn, can further give the 4.4 MeV gamma-ray energy through the ^{12}C(n, n$'\gamma$)^{12}C-interaction. The ^{16}O(n, α)^{12}C-interaction is definitly a source of interference with the 4.4 MeV gamma-ray resulting from C.

4.1.5 Simulation Result of Silicon-Detection

(a)

(b)

(c)
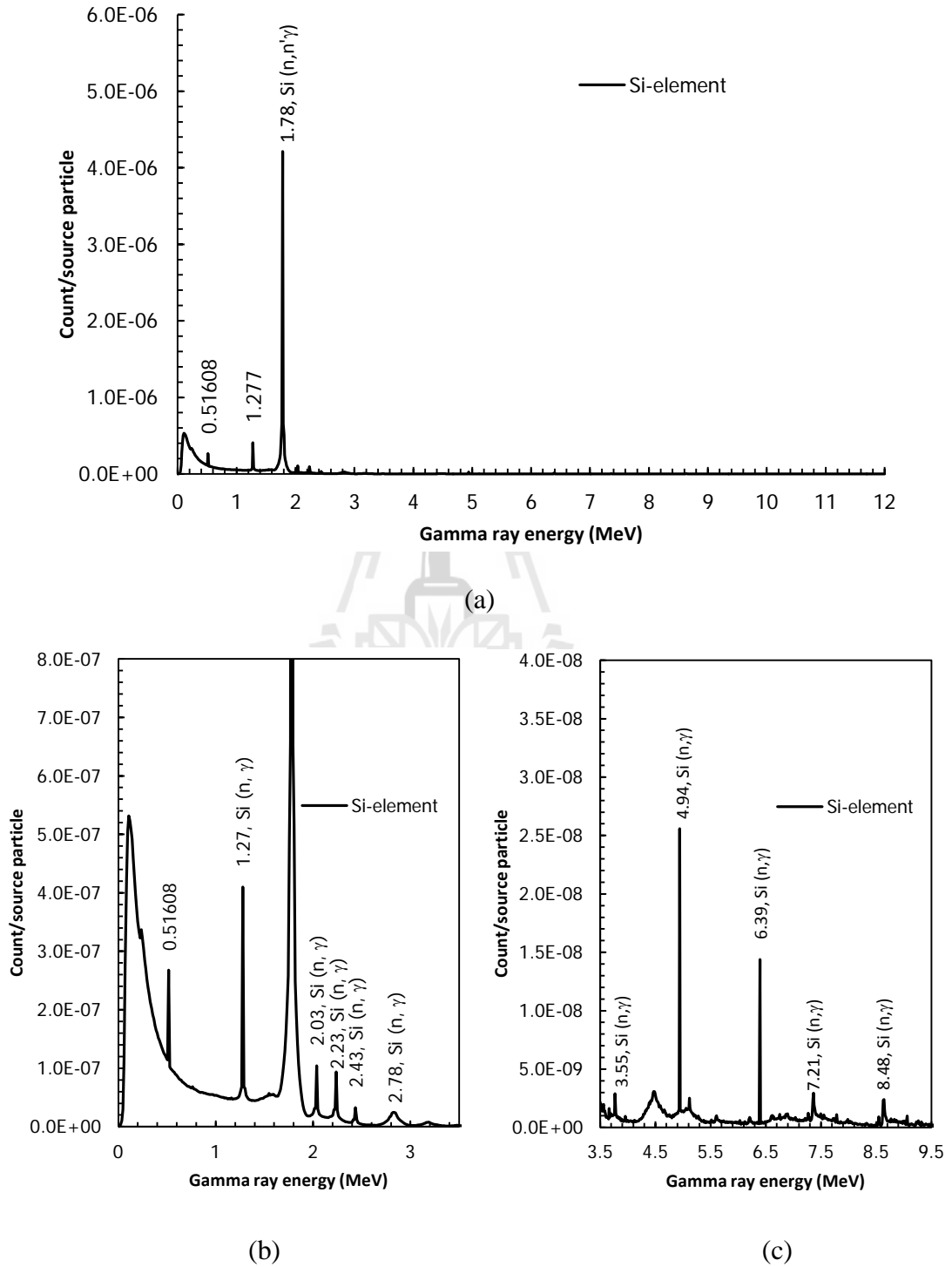
Figure 4.6 Simulated gamma-ray spectrum resulting from the detection of Si.

Figure 4.6 represents the gamma-ray spectrum resulting from the detection of Si, an elemental compositions of sand-formation. As shown in the spectrum, there is a prominent gamma-ray line at 1.78 MeV with the cross section of 0.41 b. Since this gamma-ray is well separated from TNT's elemental compositions gamma-rays, it is not expected to be a source of interference for the landmine detection. The expanded spectrum of Figure 4.6 (b) shows the 2.23 MeV from the neutron capture interaction with Si which has similar energy to that of the 2.22 MeV from H. It therefore can be an interfering problem to the detection of TNT based on TNA technique.

4.1.6 Simulation Results of Calcium-Detection
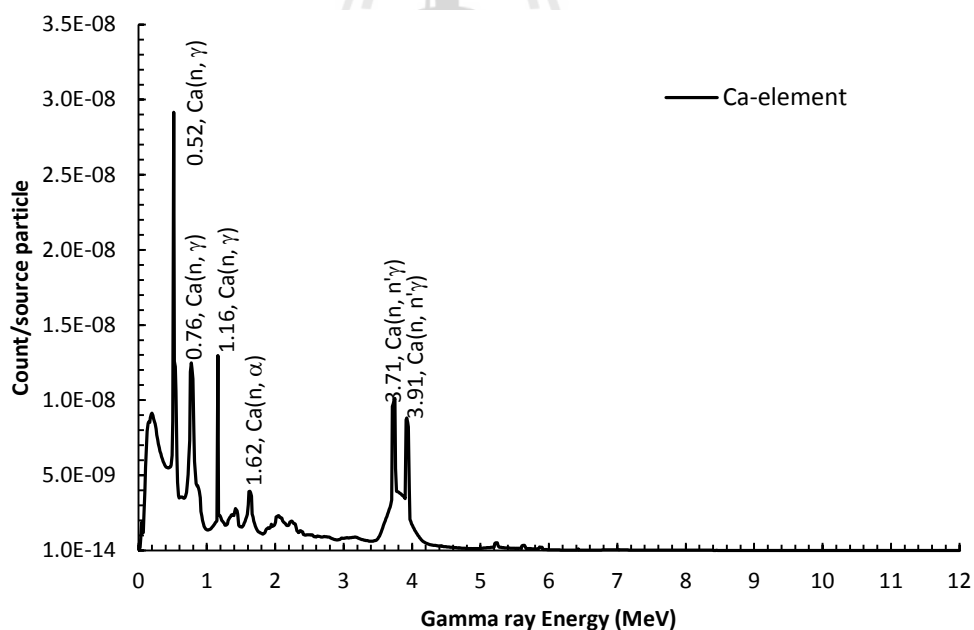
Figure 4.7 Simulated gamma-ray spectrum resulting from the detection of Ca

Figure 4.7 shows the gamma-ray spectrum resulting from the detection of Ca, an elemental composition of calcium carbonate-formations. As shown in the

spectrum, there are a couple of low energy gamma-rays which have quite low cross sections. Therefore, the interference from these gamma-rays should not be expected.

4.1.7   Simulation Results of The Aluminum-Detection
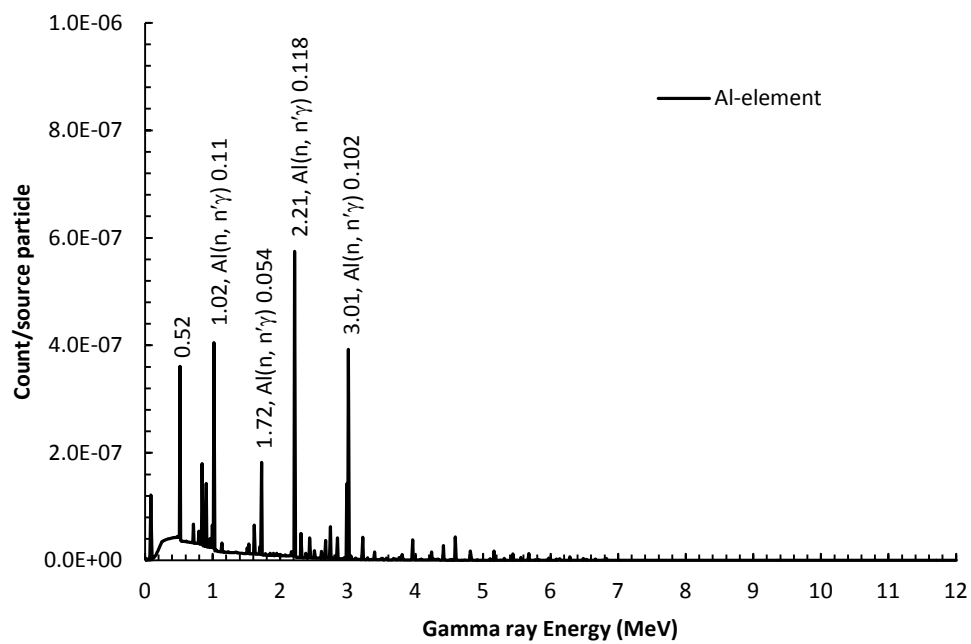
Figure 4.8 Simulated gamma-ray spectrum resulting from the detection of Al.

Figure 4.8 describes the gamma-ray spectrum resulting from the detection of Al, an elemental composition of clay-formation. As shown in the spectrum, there are a couple of low energy gamma-rays with low cross section values, including the 2.21 MeV line from the ^{27}Al(n, n′γ)^{27}Al-interaction. These gamma-rays are not expected to interfere with the gamma-rays induced from the elemental composition of TNT, except with the 2.22 MeV from H.

4.2   Simulation of Materials Detection

In this section, the detection of TNT-landmine and ground-formations, in the form of materials, are simulated. These simulations are based on using the cylindrical-geometry model with the dimensions as specified in Chapter III. The TNT-landmine that has a cylindrical shape with 8-cm diameter and 4-cm height has the varying masses. The different mass values of TNT are obtained by changing density of TNT from 1.64-5.11 g/cm^3,while keeping the landmine volume the same. Doing this, the varying masses of TNT from 290-3,000 g are obtained. Two radioactive sources, ^{252}Cf and ^{241}Am-^{9}Be are used in the simulation, generating fast neutrons for the simulation. The neutron source which locates at 5-cm above ground- formation and 5-cm below the gamma-ray detector front face, emits neutrons in the forward direction toward the landmine direction. For each simulation case, the total number of neutron per second, emitted from source, is 5×10^8. The simulated statistical error of most simulated gamma-rays are about 5%, except those of the 10.8 MeV lines which may marginally exceed the 5% limit. Three types of gamma-ray detectors, namely, NaI(Tl), BGO and LaBr$_3$:Ce are used in the simulation. All of them have the same dimensions, being 12.7-cm diameter and 12.7-cm height. The simulated gamma-ray outputs are in two forms, namely, the average flux over a cell (F-4 tally) and the energy distribution of pulses created in a detector (F-8 tally). Energies and cross sections of gamma-rays induced from interactions between neutrons and materials are given in Table 4.1 for the reference. The following sections give the result of each simulation.

4.2.1 Simulation Results Based on Using NaI(Tl)-Detector

For the simulation based on using NaI(Tl) gamma-ray detector, there are various combinations of the detection's components, the following sections give the simulation results of those combinations.

4.2.1.1 Simulation Results of The NaI(Tl)/^{252}Cf/Sand-Combination

(a)
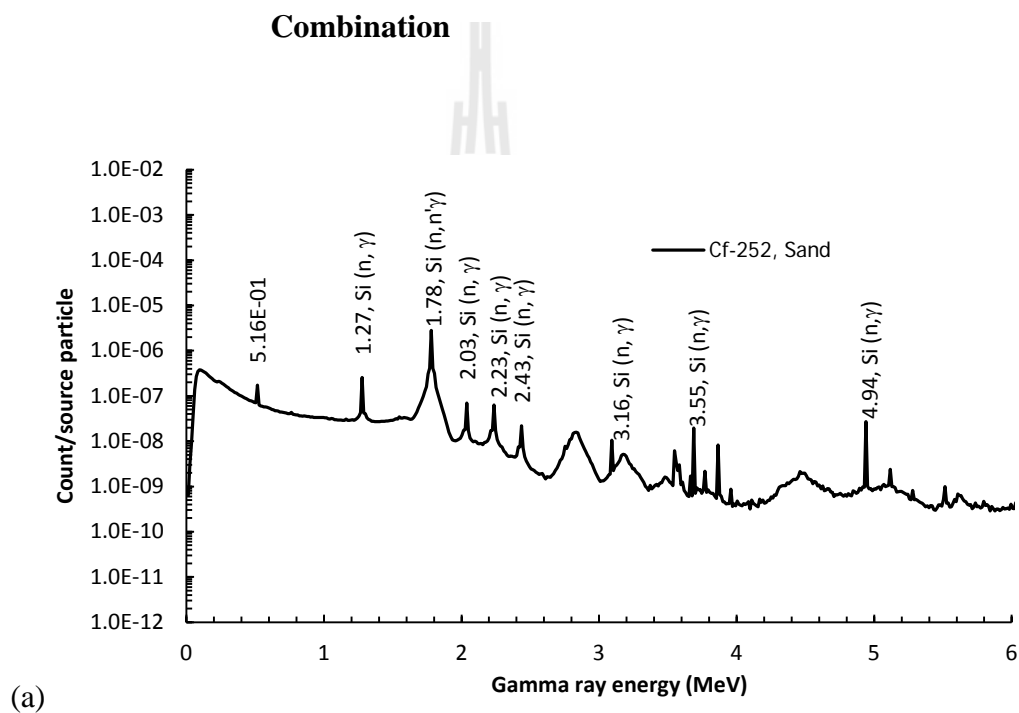
Figure 4.9   Simulated gamma-ray spectra resulting from using the NaI/^{252}Cf-detector head to detect sand-formation without TNT-landmine: (a) and (b) are the F-4 tally gamma ray spectra for low and high-energy, (c) is the F-8 tally gamma ray spectrum.

(b)

(c)
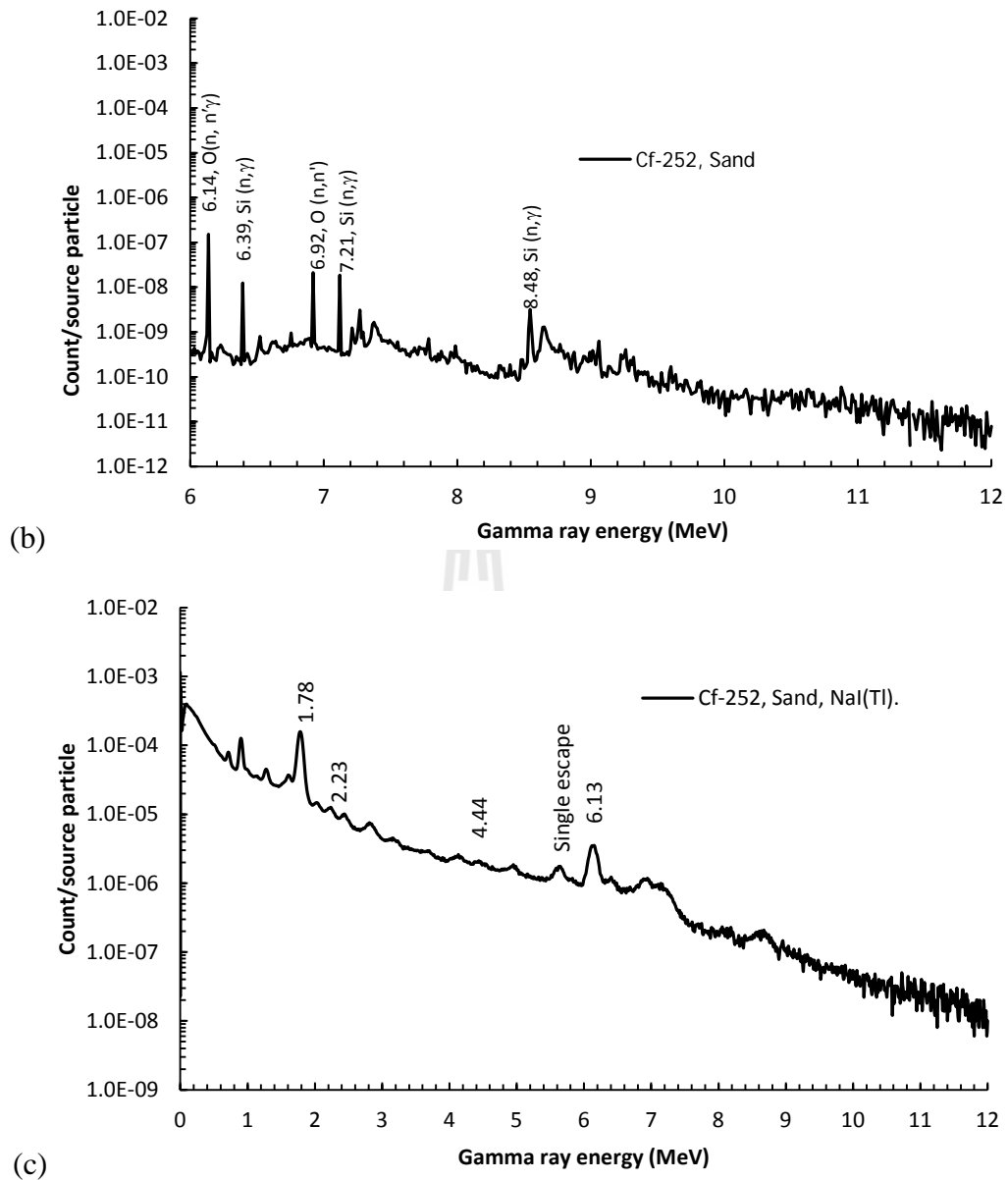
Figure 4.9 (Continued) Simulated gamma-ray spectra resulting from using the NaI/ ^{252}Cf- detector head to detect sand-formation without TNT-landmine: (a) and (b) are the F-4 tally gamma ray spectra for low and high-energy, (c) is the F-8 tally gamma ray spectrum.

Figure 4.9 shows the simulated gamma-ray spectra resulting from using the NaI(Tl)/^{252}Cf- detector head to detect sand-formation without TNT-landmine. In Figure 4.9 (a) and (b) show the F-4 tally gamma-ray spectra in the low- and high-energy regions, respectively, while (c) shows the F-8 tally gamma-ray spectrum. In Figure 4.9 (a), the 2.237 MeV gamma-ray with cross section of 0.025 b from the ^{28}Si(n, γ)^{29}Si-interaction showed up. This gamma-ray can be a source of interference of the 2.22 MeV gamma-ray from ^{1}H(n, γ)^{2}H-interaction, one of the promising indicator for the TNA-based landmine detection technique. Though it has very low cross section comparing to that of the 2.22 MeV gamma-rays (0.332 b), it can give such a problem because the sand-formation contains a lot more numbers of sand's Si-nuclei than the numbers of TNT's N-nuclei. The real interfering source is definitely the 6.13 MeV gamma-rays from ^{16}O (n, n′γ)^{16}O-interactions as already mentioned in Section 4.1.2. Therefore the 6.13 gamma-ray line can't be used for the landmine detection based on the FNA-detection technique definitely.

4.2.1.2 Simulation Results of The NaI(Tl)/^{252}Cf/Sand/TNT-Combination

(a)

(b)
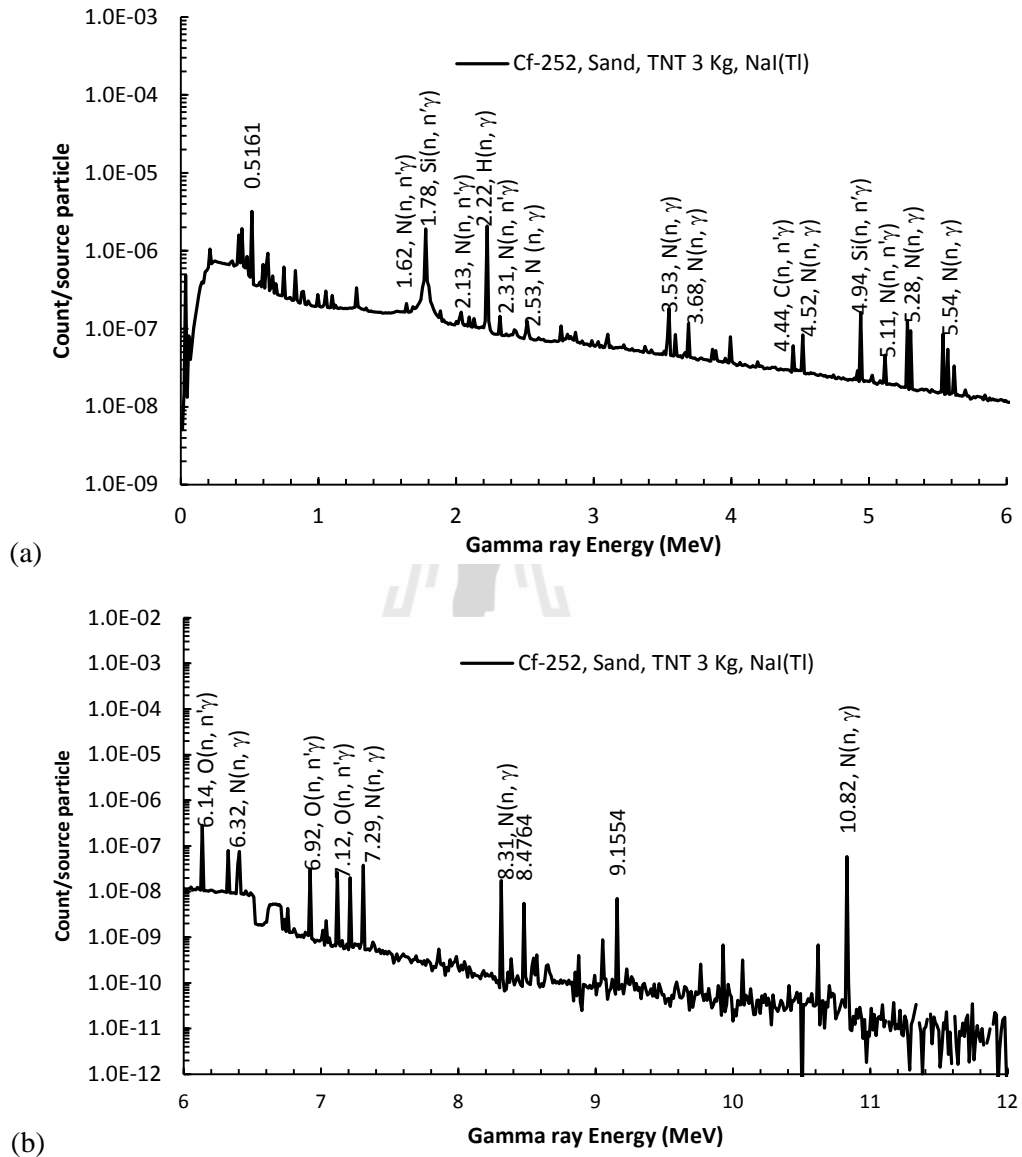
Figure 4.10 Simulated gamma-ray spectra resulting from using the NaI(Tl)/^{252}Cf-detector head to detect 3 kg TNT-landmine buried under sand-formation at 5 cm deep: (a) and (b) are the F-4 tally gamma ray spectra for low and high-energy regions, respectively, (c) is the F-8 tally gamma ray spectrum.

(c)
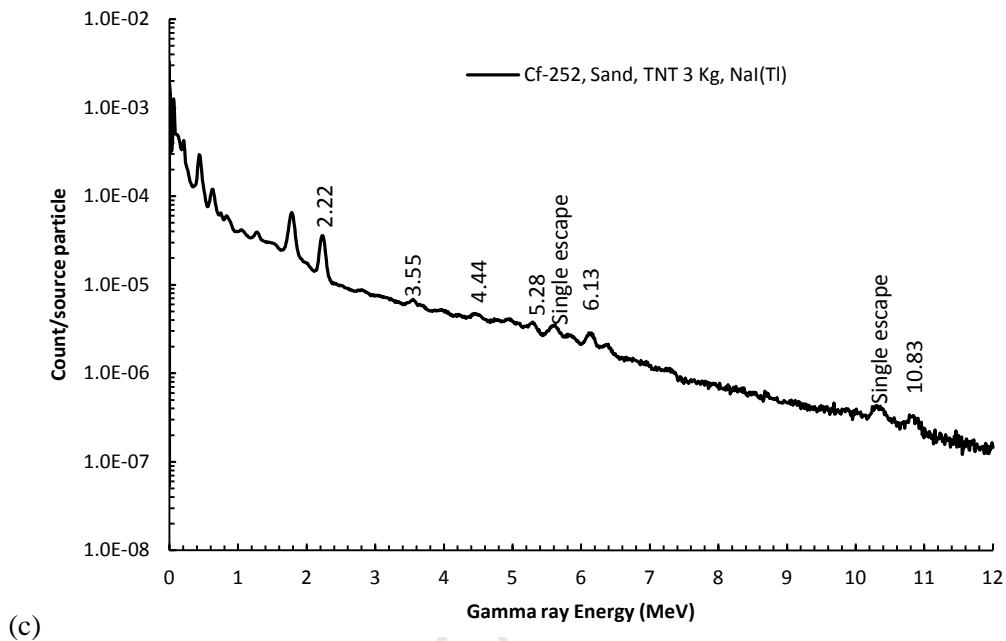
Figure 4.10 (Continued) Simulated gamma-ray spectra resulting from using the NaI(Tl)/^{252}Cf- detector head to detect 3 kg TNT-landmine buried under sand-formation at 5 cm deep: (a) and (b) are the F-4 tally gamma ray spectra for low and high-energy regions, respectively, (c) is the F-8 tally gamma ray spectrum.

Figure 4.10 shows the simulated gamma-ray spectra resulting from using the NaI(Tl)/^{252}Cf-detector head to detect 3 kg TNT-landmine buried under sand-formation at 5 cm-deep. Figure 4.10 (a) and (b) show the F-4 tally gamma-ray spectra in the low- and high- energy regions, respectively, while Figure 4.10 (c) shows the F-8 tally gamma-ray spectrum. Most of the gamma-ray energies arising from neutron interactions with TNT and sand's elemental compositions appeared in the F-4 spectra. These gamma-ray energies agree with those listed in Table 4.1. However, only some prominent gamma-ray lines appeared in the F-8 spectrum because some of the small peaks are buried under spectrum's Compton continuum. The prominent gamma-ray lines that appeared in the F-8 spectrum are the 2.22 MeV from ^{1}H(n, γ)^{2}H, the 4.44

MeV from ^{12}C (n, n'γ)^{12}C, the 6.13 MeV from ^{16}O (n, n'γ)^{16}O and the 10.83 MeV from ^{1}H(n, γ)^{2}H-interactions. The low intensities gamma-ray lines, such as the 3.55, 5.28 MeV including the two single escapes of the 6.13 and 10.8 MeV lines, also appeared in the F-8 tally spectrum ray.
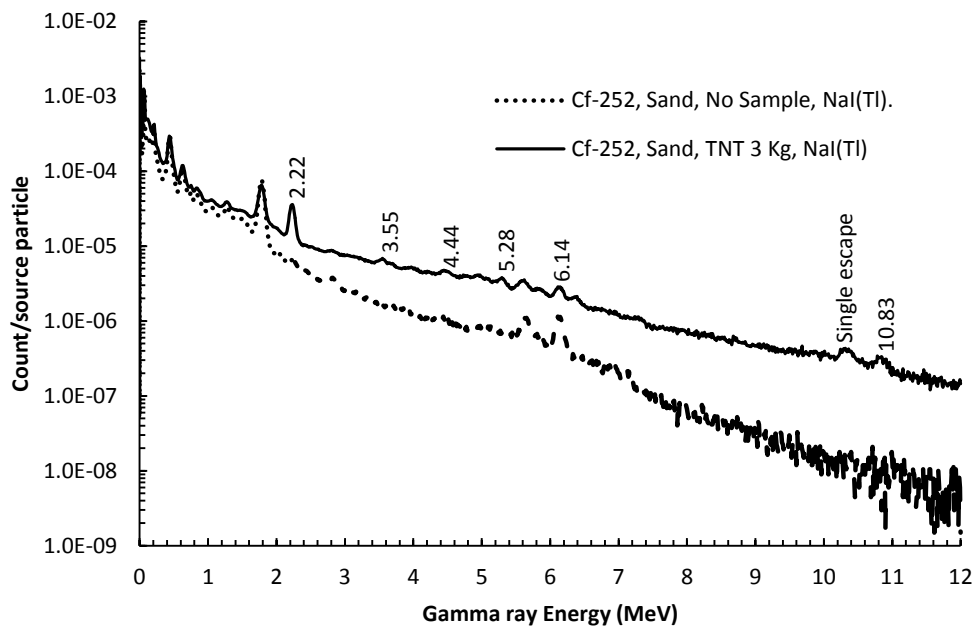
Figure 4.11 Comparison between gamma-ray spectra resulting from the detections of TNT-landmine (3 kg) buried under sand-formation and those of the sand-formation.

Figure 4.11 represents the comparison between gamma-ray spectra resulting from the the detections of TNT-landmine (3 kg) buried under sand-formation and those of the sand-formation without TNT. Notice that the TNT-based spectrum has higher Compton continuum than that of the sand-formation spectrum. This effect is the result of the thermalization of fast neutrons by TNT which contain high number of H-elements, the most effective neutron moderator. Notice that while the 2.2 and 10.8

MeV gamma-ray peaks which appeared in TNT-landmine based spectrum, there is no such peaks appeared in the sand-formation-based spectrum. However, both spectra show the existence of gamma-rays from C and O, the elemental compositions of both TNT and sand.
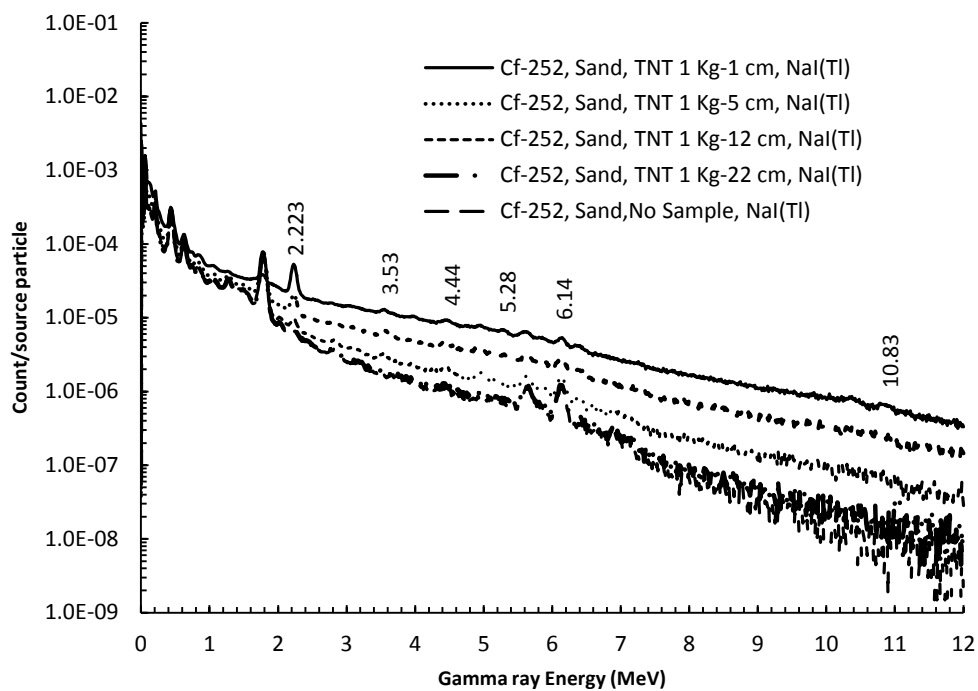
Figure 4.12 Comparison between gamma-ray spectra resulting from the detections of TNT-landmine (1 kg) buried under sand-formation at different depths ranging from 1 to 22 meters.

Figure 4.12 shows the comparison between gamma-ray spectra resulting from the detections of TNT-landmine (1 kg) buried under sand-formation at different depths ranging from 2 to 22 meters. Notice that the Compton continuum for the shallower depth spectrum has higher intensities than those of the deeper depth spectrum. This effect can be explained that TNT is a good neutron moderator,

creating more thermal neutrons when it locates near ground surface. These thermal neutrons give rise to more gamma-ray energies that may under goes elastic scattering throughout the detector medium.

Figure 4.13 describes the variations of net areas of the 2.2, 4.4, 6.1 and 10.8 MeV gamma-rays. The 2.22 and 10.83 MeV decrease very fast with depth, while the 4.44 and 6.13 MeV decrease slowly with depth. This results show that there are more fast neutrons at deeper depth; therefore, there are more of the 4.44 and 6.13 MeV created. Another effect comes to play the role in the high intensities of the 6.13 MeV. It is also due to the high number of O-nuclei of sand-formation. Notice that intensities of the 10.8 MeV gamma-rays decrease very fast with depth, being zero at 12 cm depth. This gamma-ray is not detectable when TNT's buried depth is higher at 12 cm.
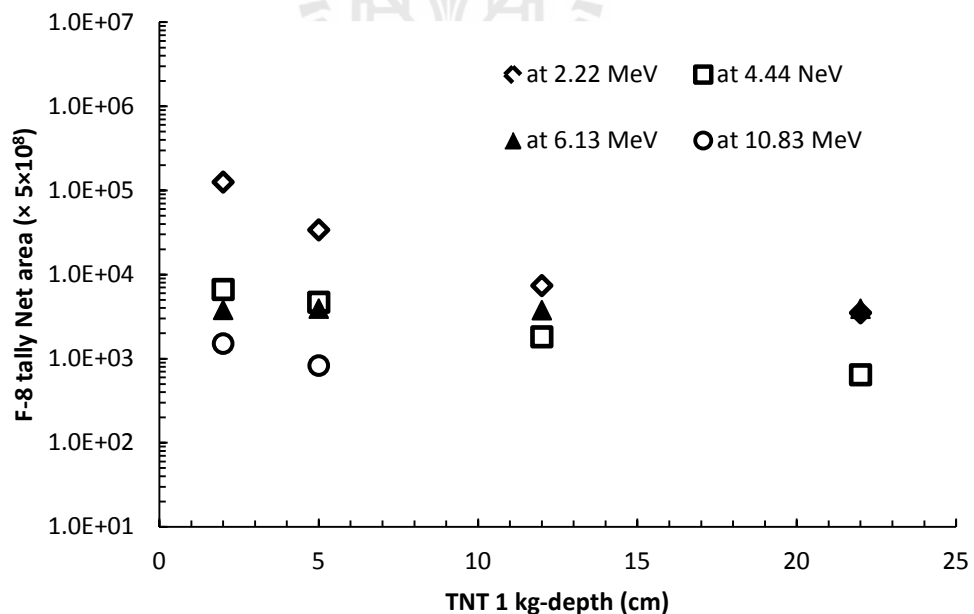
Figure 4.13 Net areas of the 2.2, 4.4, 6.1 and 10.8 MeV gamma-rays resulting from the detection of TNT-landmine buried at 2, 5, 12 and 22 cm deep based on using ^{252}Cf/NaI(Tl)- detector head.

4.2.1.3 Simulation Results of The NaI/^{241}Am-^{9}Be/Sand/TNT-Combination

In the simulation, the simulation compositions are the same as that of Section 4.2.1.2 except the neutron source is replaced with ^{241}Am-^{9}Be. The simulation results of this section are similar to that of Section 4.2.1.2. A comparison between gamma-ray spectra resulting from the detections of TNT-landmine buried under sand-formation at 5 cm based on using ^{252}Cf and ^{241}Am-^{9}Be neutron sources is shown in Figure 4.14. Generally, these gamma-ray spectra show similar characteristics. However, the ^{241}Am-^{9}Be-based spectrum shows higher Compton continuum. This effect is due to the higher intensity of fast neutrons from ^{241}Am-^{9}Be. The higher the neutron energies the higher the gamma-ray intensity induced.
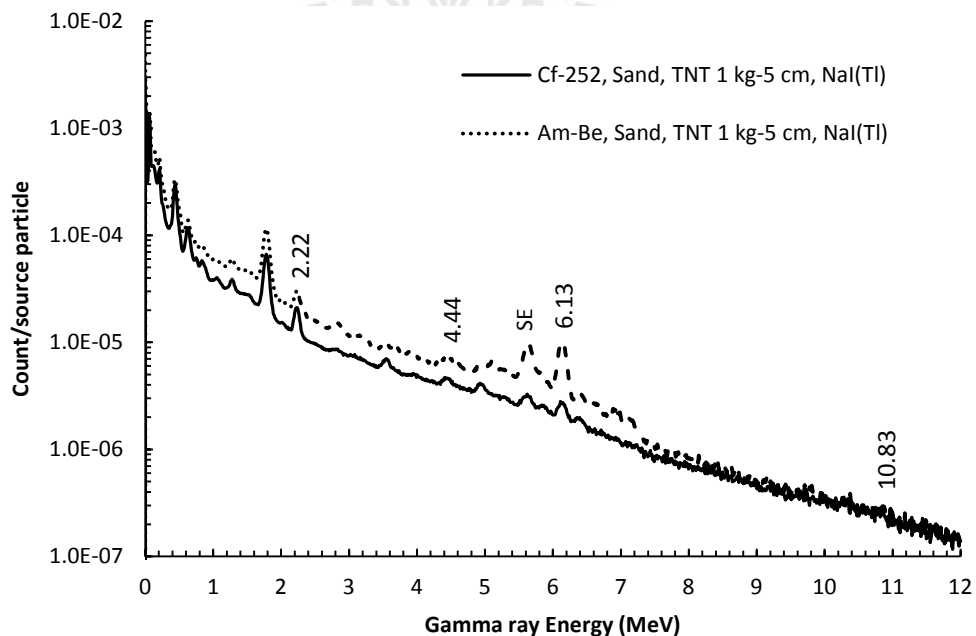
Figure 4.14 Comparison between gamma-ray spectra resulting from the detections of 1 kg TNT-landmine buried at 5-cm under sand-formation based on using ^{52}Cf and ^{241}Am-^{9}Be as neutron sources.

Figure 4.15 shows the comparison of gamma-ray spectra resulting from the detections of TNT-landmine buried under sand-formation at 2, 5, 12 and 22 m deep. The results of these simulations show that the induced gamma-rays intensities decrease with depth. At 22-m buried depth, the induced gamma-ray spectrum characteristics are almost the same as those of the sand-formation simulation. This result implies that the limit of buried depth for landmine detection based on using ^{241}Am-^{9}Be as the neutron source is 22 cm.
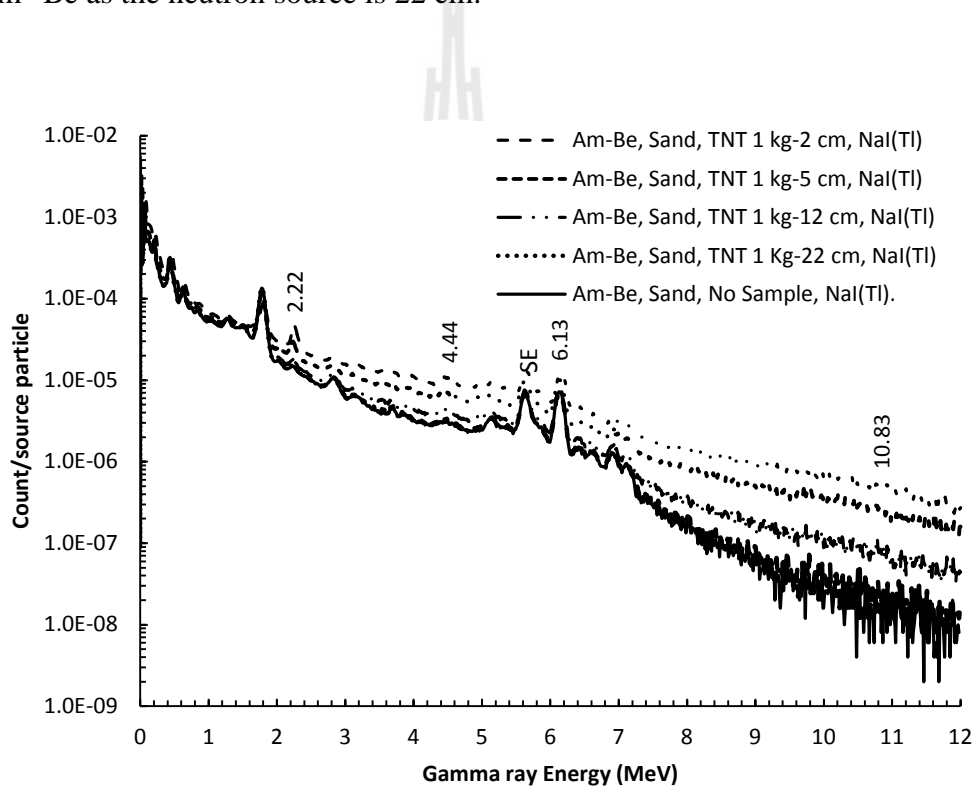
Figure 4.15   Comparison of gamma-ray spectra resulting from the detections of 1 kg TNT-landmine buried under sand-formation at different depths ranging from 2 to 22 cm based on using ^{241}Am-^{9}Be as the neutron source.

Figure 4.16 represents the deduced net areas of the 2.22, 4.44, 6.13 and 10.83 MeV gamma-rays of Figure 4.15. It is shown that the net areas decrease with depth.

The different of this simulation when compare to that of Figure 4.13 is the net area at 12 cm deep is not zero. This result implies that ^{241}Am-^{9}Be can detect TNT-landmine at higher depth than that of ^{252}Cf.
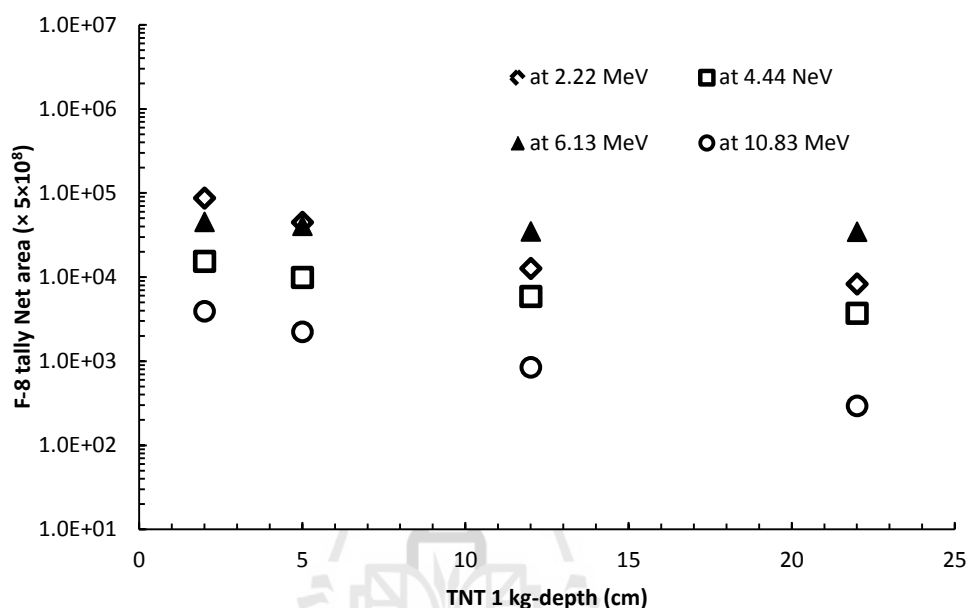
Figure 4.16   Net areas of the 2.2, 4.4, 6.1 and 10.8 MeV gamma-rays resulting from the detection of TNT-landmine buried at 2, 5, 12 and 22 cm deep based on using the ^{241}Am-^{9}Be/NaI(Tl)-detector head.

To investigate the minimum mass detectable limit of the landmine detection, the simulations of the detections of 290-g TNT by using both neutron sources are performed. Figure 4.17 shows the simulated gamma-ray spectra of different energy regions, resulting from the detection of 290-g TNT buried under sand-formation at 5-cm depth by using ^{252} Cf.

(a)

(b)

(c)

(d)
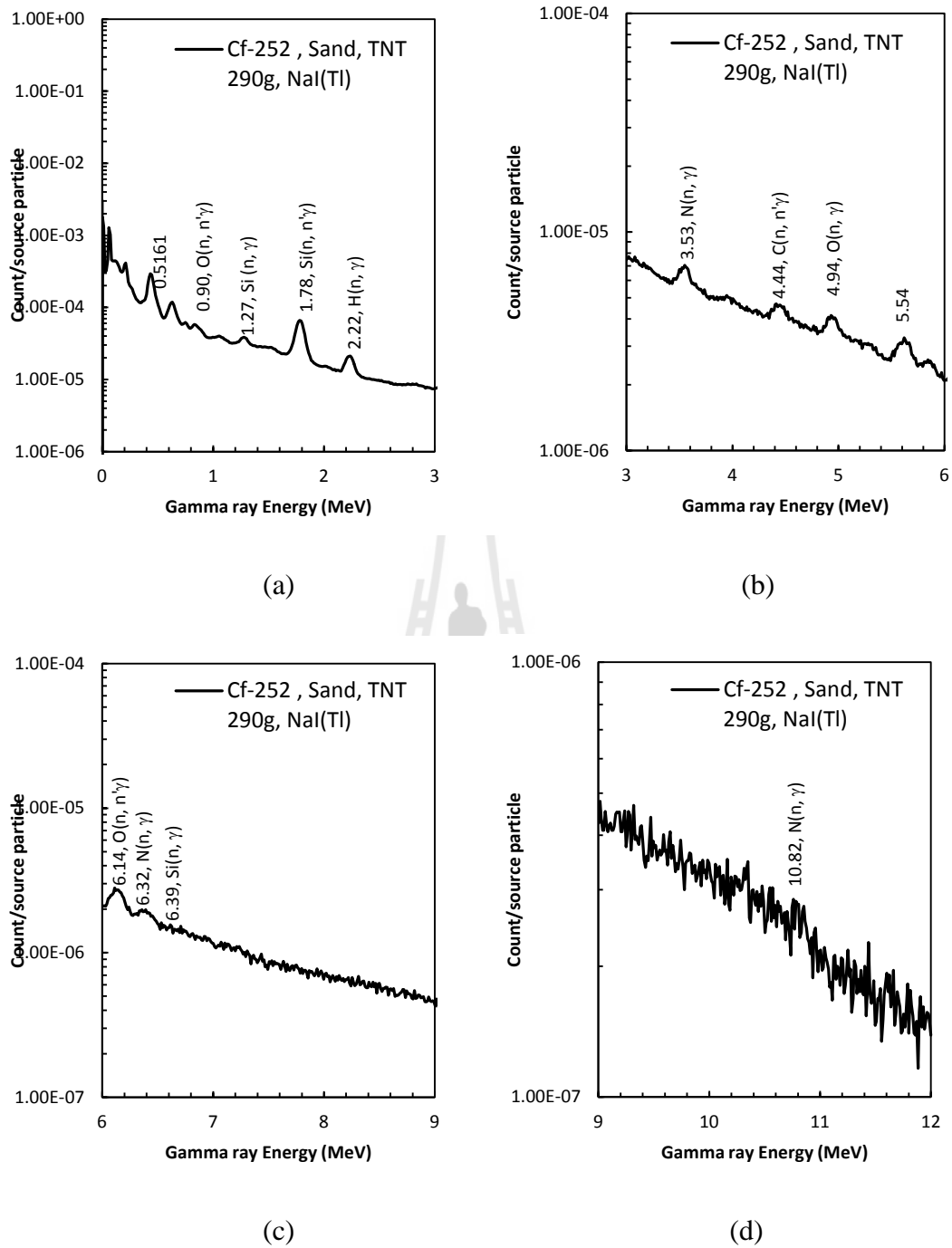
Figure 4.17 Simulated gamma-ray spectra of different energy regions, resulting from the detection of 290-g TNT buried under sand-formation at 5-cm deep based on using [252] Cf as the neutron source.

Most of the prominent gamma-rays, the 2.22, 4.44 and 6.13 MeV show up in the spectrum while the 10.81 MeV gamma-ray is missing. However, the 2.22 MeV gamma-ray intensity is less than that of the sand-formation detection. This effect may be due to the interference between gamma-rays resulting from neutron-interactions with the H-elemental composition of TNT and those of the Si-elemental composition of sand-formation. When TNT is put under the sand-formation for detection, a volume of sand is reduced, making the number of Si-nuclei reduced. This reduction reduces the interfering gamma-ray intensities induced from Si, which in turn, reducing the 2.2 MeV gamma-ray intensities. A similar problem arises when ^{241}Am-^{9}Be is used as the neutron source. These results implied that, the complementary FNA-TNA technique may not be able to use to detect the small- size landmine (290-g) buried under sand-formation at 5-cm depth with NaI- gamma-ray detector.

4.2.1.4 Simulation Results of The NaI(Tl)/^{252}Cf/CaCO$_3$/TNT- Combination

(a)

(b)
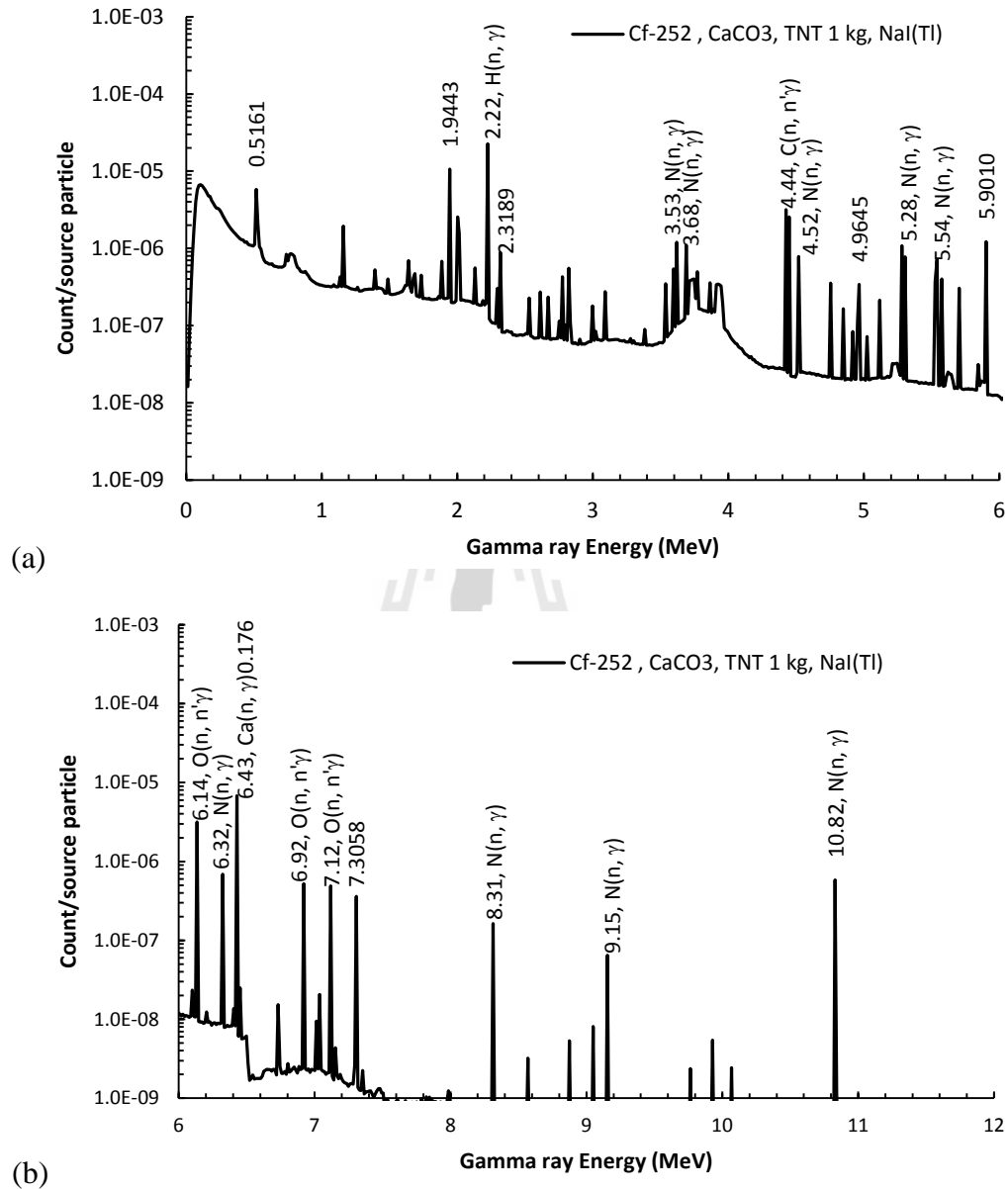
Figure 4.18 Simulated F-4 Tally gamma-ray spectra results from using ^{252}Cf to detect 1 kg TNT-landmine buried under CaCO$_3$-formation at 5 cm-depth.

In the simulation, the detection compositions are the same as that of Section 4.2.1.3, except the sand-formation is replaced with $CaCO_3$. Figure 4.18 (a) and (b) show the F-4 tally gamma-ray spectra in the low- and high- energy regions, respectively. In these spectra, all gamma-rays resulting from neutron activations of ^{28}Si are missing but the 1.94, 4.41 and 6.42 MeV, resulting from neutron activations of ^{40}Ca showed up. Among these gamma-rays, only the 4.41 MeV with cross section of 0.071 b may give interfering problem to the 4.44 MeV gamma-ray (with 0.18-0.38 b) from ^{12}C. No to forget, this kind of interfering problem already existed due to gamma-rays from the neutron activation of ^{12}C, the elemental composition of $CaCO_3$-formation. Since $CaCO_3$ also contain oxygen, the 6.13 MeV gamma-rays resulting from neutron activations of ^{16}O from both the TNT and formation should be expected. Therefore, the complementary FNA-TNA technique should not be qualified for the detection of landmine with the $NaI(Tl)/^{252}Cf/CaCO_3/TNT$-combination. Another simulation similar to this combination is performed but with $^{241}Am-^9Be$ as the neutron source. In this simulation, the same interfering problem existed. Therefore, the complementary FNA-TNA technique based on using the $NaI(Tl)/^{241}Am-^9Be$ $/CaCO_3/TNT$-combination should not be qualified to detect landmine either.

4.2.1.5 Simulation Results of The $NaI(Tl)/^{252}Cf/Clay/TNT$-Combination

In the simulation, the detection compositions are the same as that of Section 4.2.1.4, except the sand-formation is replaced by Clay which contains oxygen, silicon, aluminum and hydrogen with weight % of 56, 36, 7 and 1, respectively. Figure 4.19 shows the simulated F-4 tally gamma-ray spectra resulting from using the

NaI(Tl)/^{252}Cf/Clay/TNT-combination to detect 1 kg TNT-landmine buried under clay-formation at 5 cm depth. Figure 4.19 (a) and (b) show the F-4 tally gamma-ray spectra in the low- and high- energy regions, respectively. In the low energy region, the 2.22, 2.31 and 4.44 MeV gamma-rays showed up, while the 6.13 and 10.83 MeV, showed up in the high ender region. These gamma-rays are the results of neutron activations of H-, Si- and N-elemental compositions of TNT and formation. However, at 2.22 MeV line, there is interference from the 2.21 MeV, resulting from the neutron activation of Al, an elemental composition of formation. Since there is no interference at both the 4.44 and 10.83 MeV regions, these two gamma-rays should be qualified to be used in the complementary FNA-TNA technique for the landmine detection. For completeness, the ^{241}Am-^{9}Be-neutron source is also used to simulate the detection of 1 kg-TNT buried under clay-formation at 5-cm depth. The same result as that of ^{252}Cf is obtained.

(a)
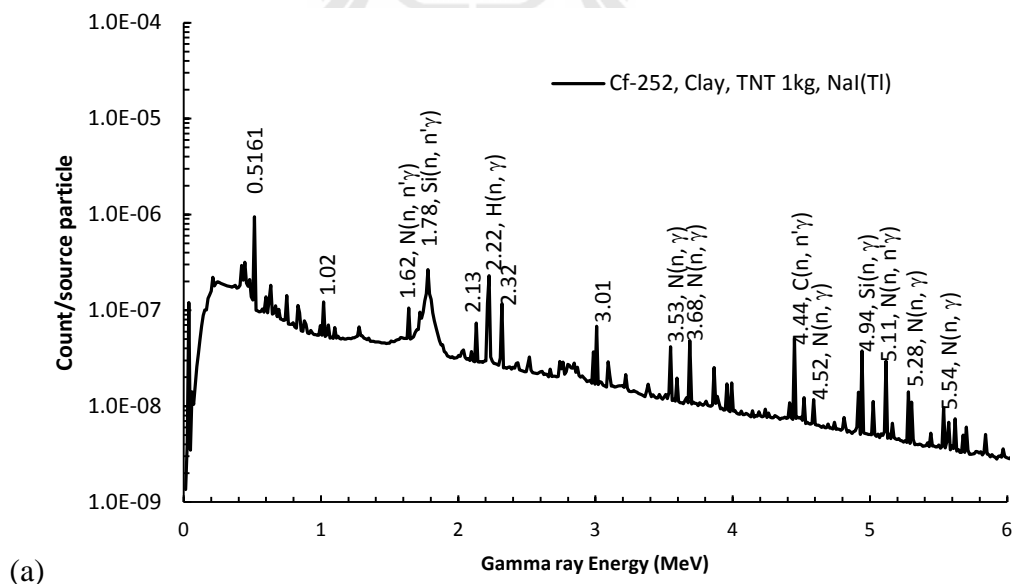
Figure 4.19 Simulated F-4 tally gamma-ray spectra based on using the NaI(Tl)/^{252}Cf/Clay/TNT-combination to detect 1 kg TNT-landmine buried under clay-formation at 5-cm depth.
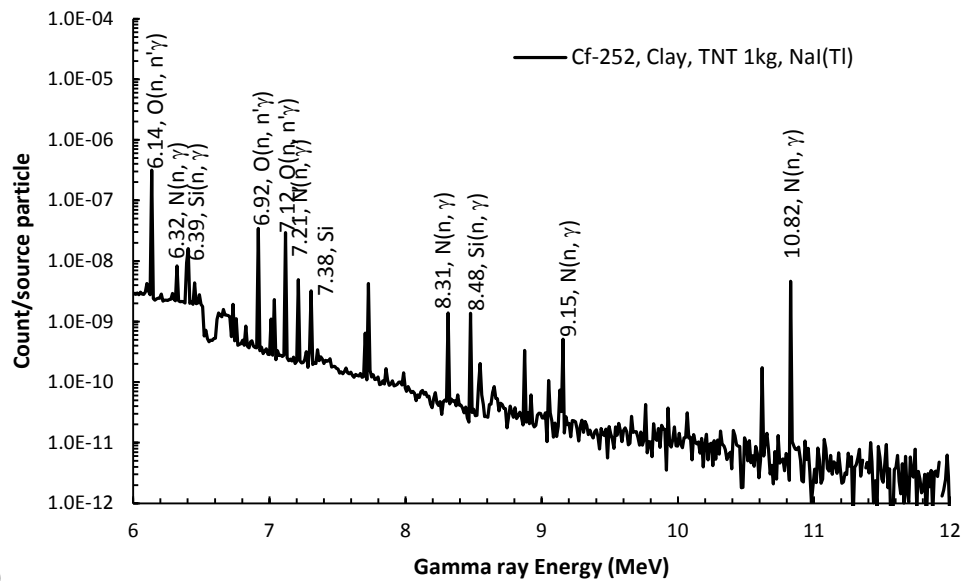
(b)

Figure 4.19 (Continued) Simulated F-4 tally gamma-ray spectra based on using the NaI(Tl)/^{252}Cf/Clay/TNT-combination to detect 1 kg TNT-landmine buried under clay-formation at 5-cm depth.

4.2.2 Simulation Results Based on Using BGO

For the simulation based on using BGO as the gamma-ray detector, there are various combinations of the landmine detection's components. The following sections give the simulation results of those combinations.

4.2.2.1   Simulation Results of The BGO/-252Cf/Sand-Combination

(a)

(b)
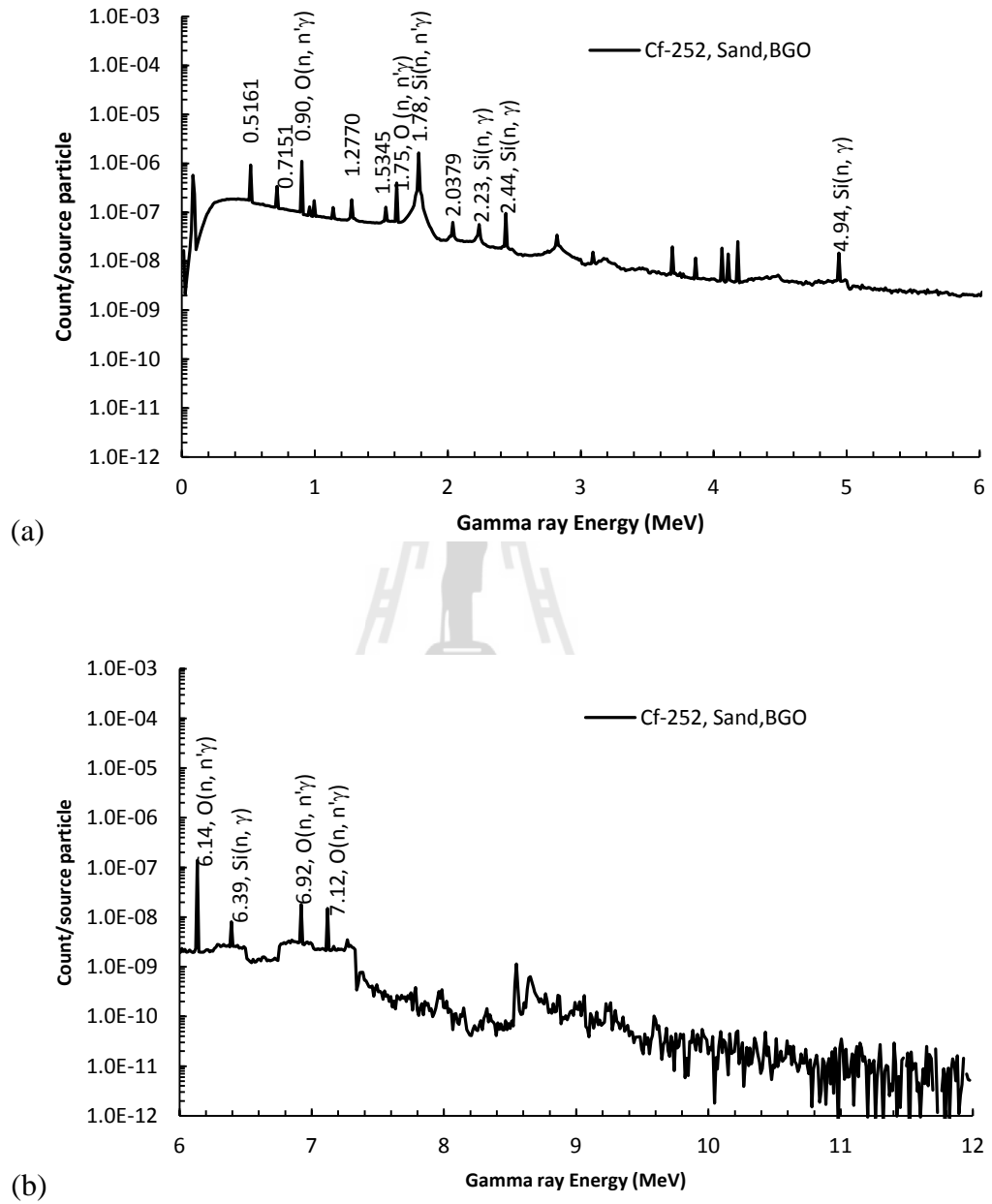
Figure 4.20   Simulated gamma-ray spectra resulting from using [252]Cf as the neutron source.
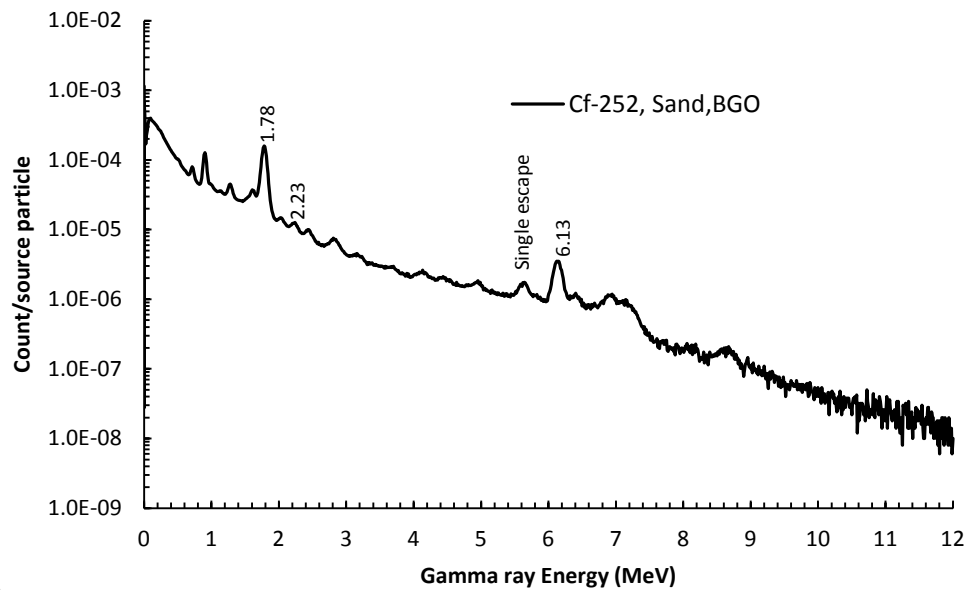
(c)

Figure 4.20 (Continued) Simulated gamma-ray spectra resulting from using ^{252}Cf as the neutron source.

In the simulation, this detection component is similar to that of Section 4.2.1.1, except that the gamma-ray detector is replaced with BGO. Figure 4.20 shows the simulated gamma-ray spectra resulting from the detection of sand formation by using the BGO/^{252}Cf- detector head. Figure 4.20 (a) and (b) show the F-4 tally gamma-ray spectra in low- and high- energy regions, respectively, while Figure 4.20 (c) shows the F-8 tally gamma-ray spectrum. The result of this simulation is similar to that of Section 4.2.1.1, in which, the 2.23 and 6.13 MeV gamma-rays occurred. These gamma-rays that are the results of the ^{28}Si(n, γ)^{29}S and ^{16}O (n, n′γ)^{16}-interactions, respectively, can be the sources of interferences of gamma-rays which are expected to be used as the landmine detection indicators. By eye inspection in Figure 4.20 (c), the corresponding F-8 tally gamma-ray spectrum of the 2.23 and 6.13 MeV gamma-ray peaks are clearly shown.

4.2.2.2 Simulation Results of The BGO/$^{-252}$Cf/Sand/TNT-Combination

In this section, the landmine detection compositions are similar to those of Section 4.2.2.1, except that the TNT-landmine of 3-kg is put under sand formation at 5-cm deep. Figure 4.21 shows the simulated gamma-ray spectra based on using the BGO/^{252}Cf-detector head to detect sand-formation with 3-kg TNT-landmine buried under sand-formation at 5-cm deep. The F-4 gamma-ray spectra in the low-and high-energy regions are shown in Figures 4.21 (a) and (b), respectively, while the F-8 gamma-ray spectrum is shown in Figure 4.21 (c).

(a)
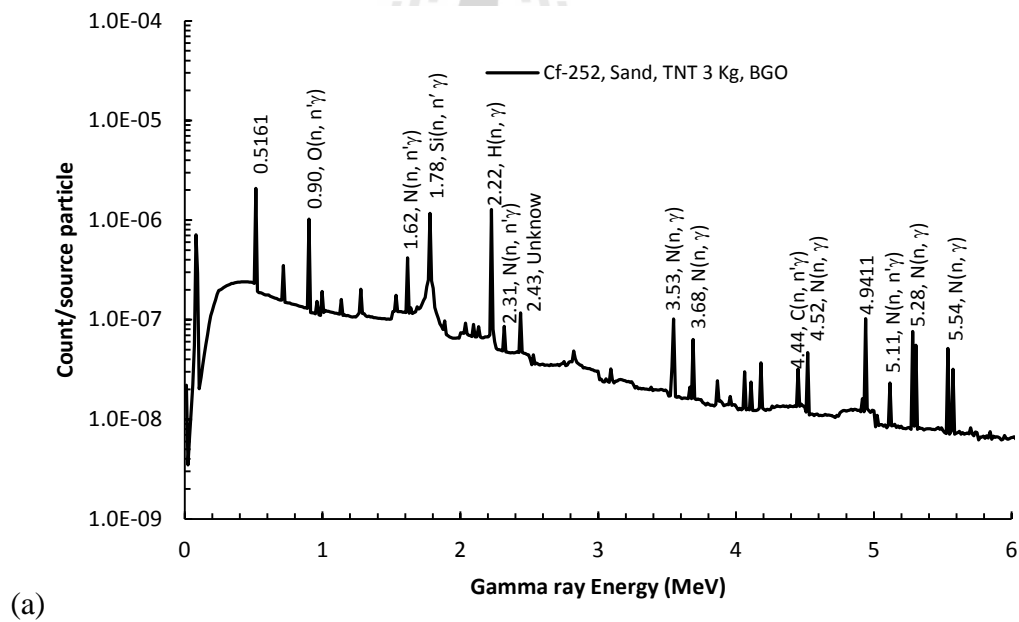
Figure 4.21 Simulated gamma-ray spectra based on using ^{252}Cf to detect sand-formation with 3-kg TNT-landmine buried under sand-formation at 5-cm depth.

(b)

(c)
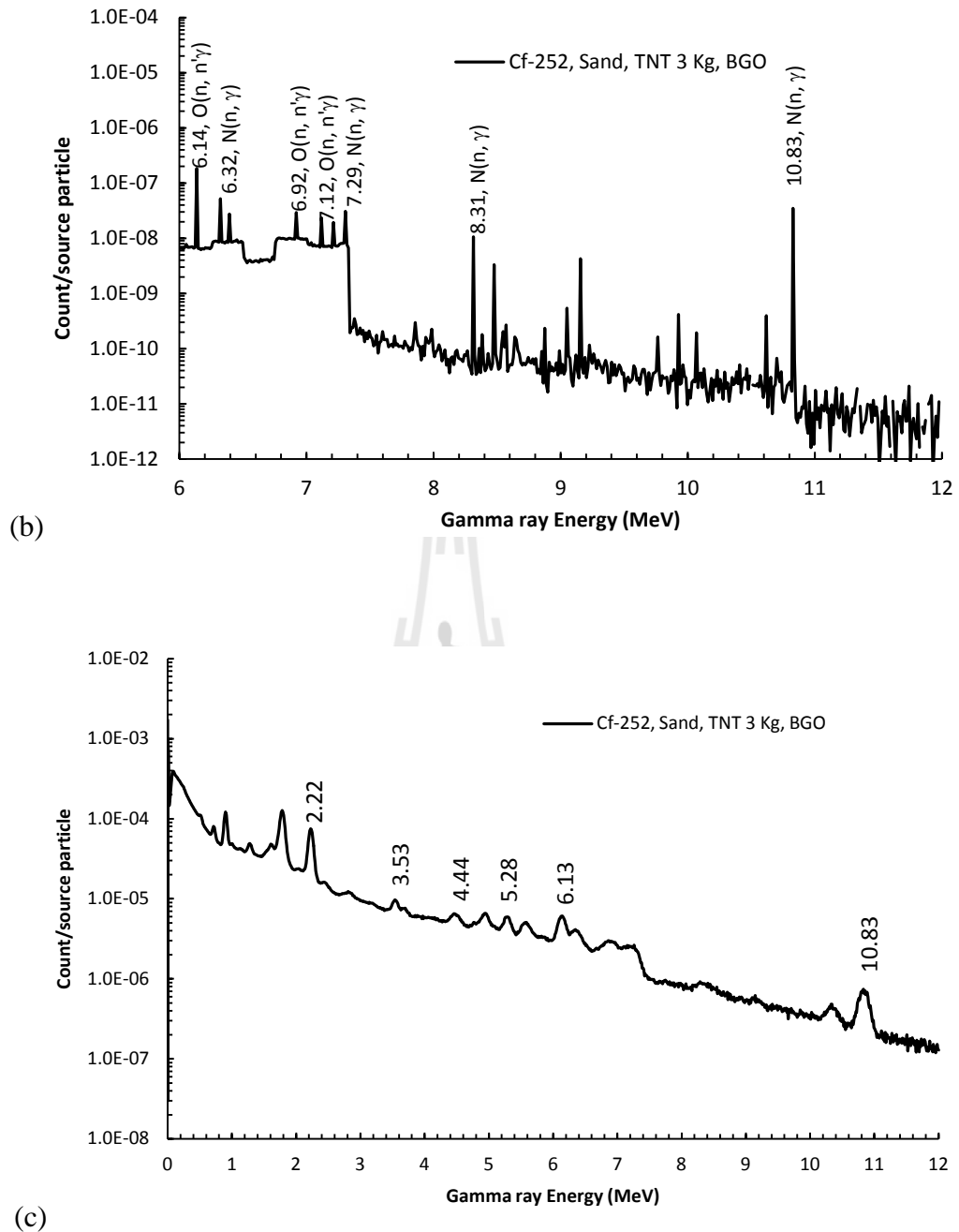
Figure 4.21 (Continued) Simulated gamma-ray spectra based on using ^{252}Cf to detect sand-formation with 3-kg TNT-landmine buried under sand-formation at 5-cm depth.

In these figures, most of the prominent gamma-rays relevant to the landmine detection based on the complementary FNA-TNA technique, occured. They are the

2.22, 4.44, 6.13 and 10.8 MeV gamma-rays. As discussed earlier many time, these gamma-rays are the results of the neutron-induced of the elemental compositions of TNT-landmine. Additionally, the 3.53 and 5.28 MeV gamma-rays, resulting from the neutron capture interactions, ^{14}N $(n,\gamma)^{15}N$, also appeared in Figure 4.21. These gamma-rays can be additional indicators for the complementary FNA-TNA landmine detection technique. By eye inspection in Figure 4.21 (c), it is quite clear that the BGO-detector has the better detection efficiency than that of the NaI-detector. The detailed analysis will be discussed later in this Chapter.
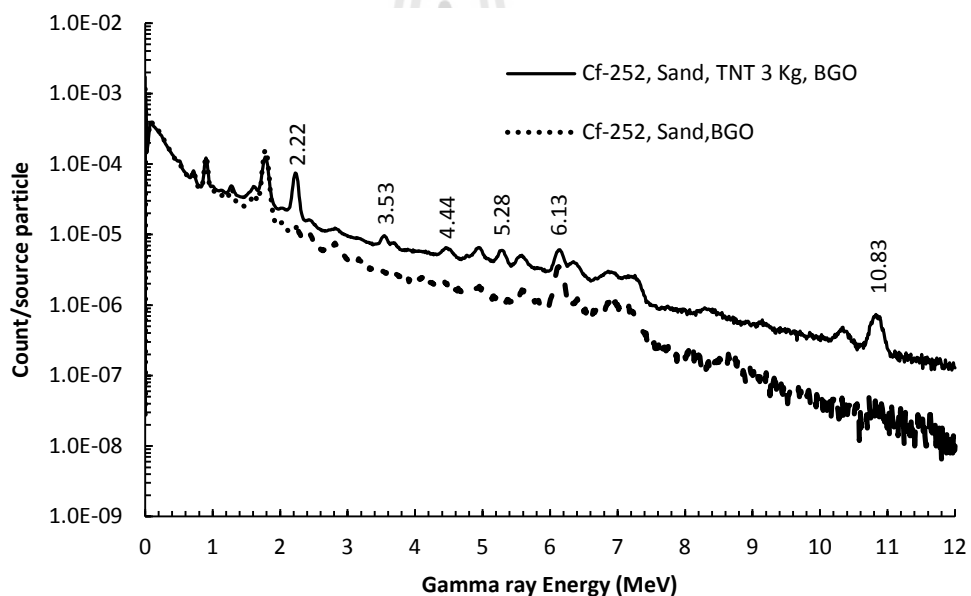
Figure 4.22 Shows the comparison between gamma-rays resulting from the simulations of the 3-kg TNT-landmine buried under-formation.

Figure 4.22 depicts the comparison between gamma-rays spectra resulting from the detections of 3-kg TNT-landmine and sand-formation. By eye inspection, it is quite clear that the 2.22, 3.53, 4.44, 5.28 and 10.83 MeV gamma-rays are missing

from the sand-formation spectrum as expected because sand doesn't have H, C and N as it elemental compositions.

To compare characteristics of gamma-ray spectra based on using the BGO- and NaI- detectors, the gamma-ray spectra resulting from the detections of 3-kg TNT-landmine based on these detectors are shown in Figure 4.23. It is quite clear that the BGO-gamma-ray detector has higher efficiency than that of the NaI- detector. Both of them show agreement in regard to the type of gamma-ray energies occurred.
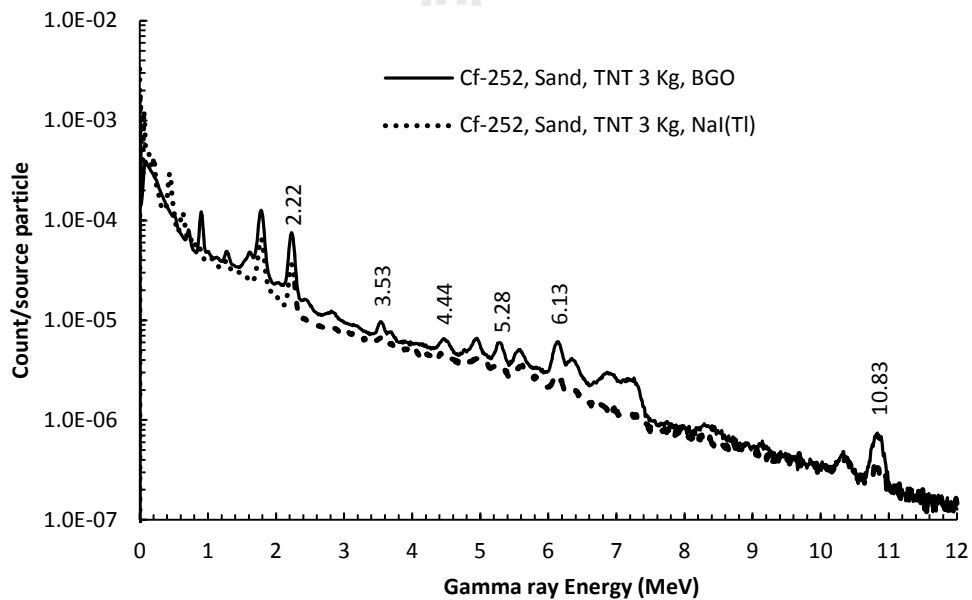
Figure 4.23 Comparison between gamma-rays spectra resulting from the detections of 3-kg TNT-landmine by using BGO and NaI(Tl) detectors.

To investigate the characteristics of gamma-ray spectra resulting from the detections of TNT-landmine with different masses based on using the BGO-detector, the simulations of the detections of TNT-landmines of masses ranging from 290g-3 kg are performed and their results are shown in Figure 4.24 for the masses of 290-900

g and in Figure 4.25 for the masses of 1-3 kg. The net areas or fluxes of the prominent gamma-ray energies are deduced from the gamma-ray spectra and the deduction results are shown in Table 4.2.

(a)

(b)
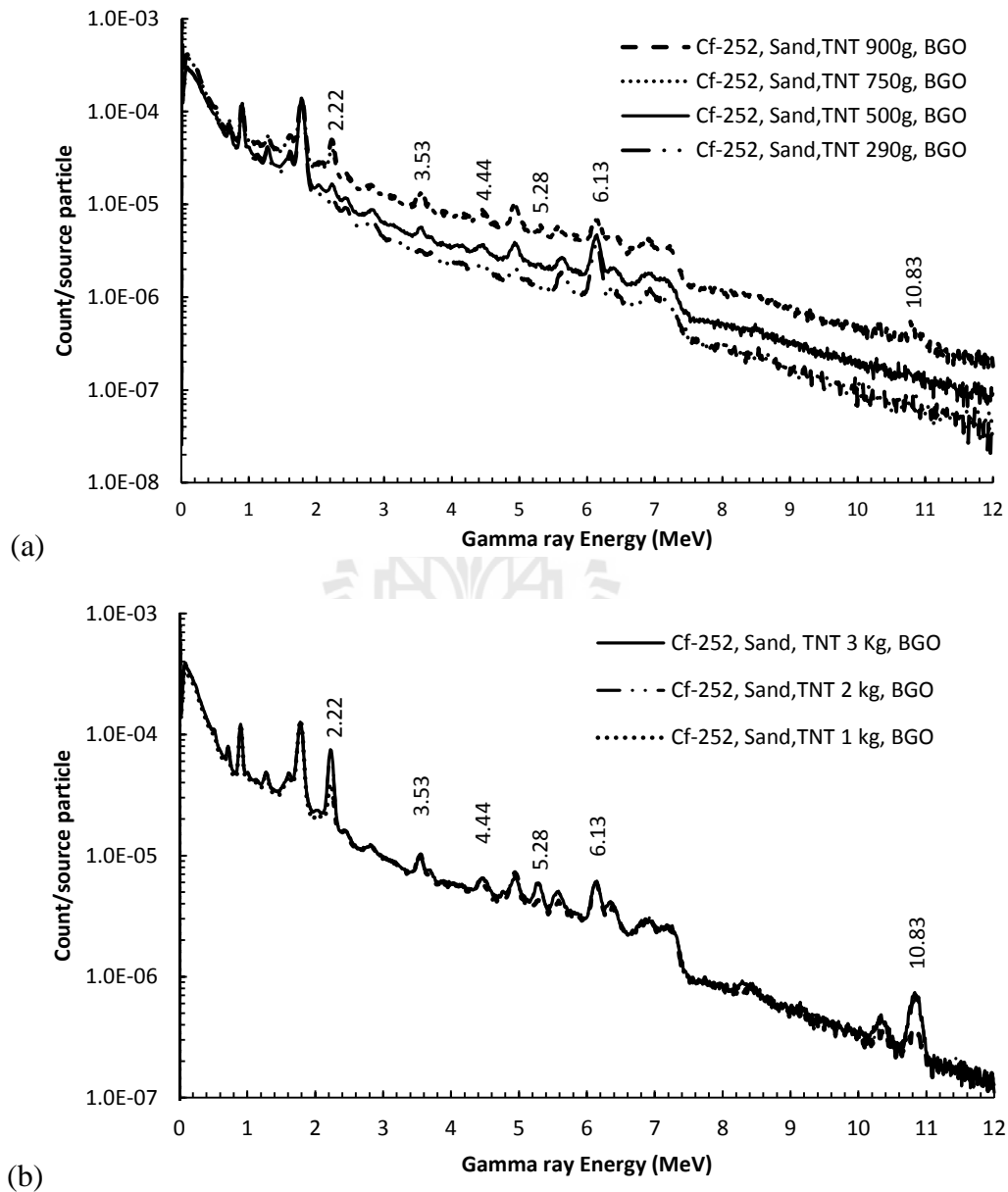
Figure 4.24 Comparison between gamma-ray spectra Resulting from the detections of TNT-landmines with varying masses ranging from 290-3,000 g.

Table 4.2 Comparison between gamma-ray spectra resulting from the detections of TNT-landmine of varying masses from 295-3,000 g.

MASS (g)	Tally 8 -Net Area ($\times 5\times10^8$)			
	2.22 MeV	4.44 MeV	6.13 MeV	10.83 MeV
295	7,007	1,699	15,511	0
500	14,732	4,111	15,771	0
750	64,376	9,746	15,918	874
900	95,759	11,422	14,993	1,389
1,000	79,065	7,511	14,261	1,889
2,000	181,771	9,473	13,996	3,518
3,000	205,793	9,677	13,981	3,779
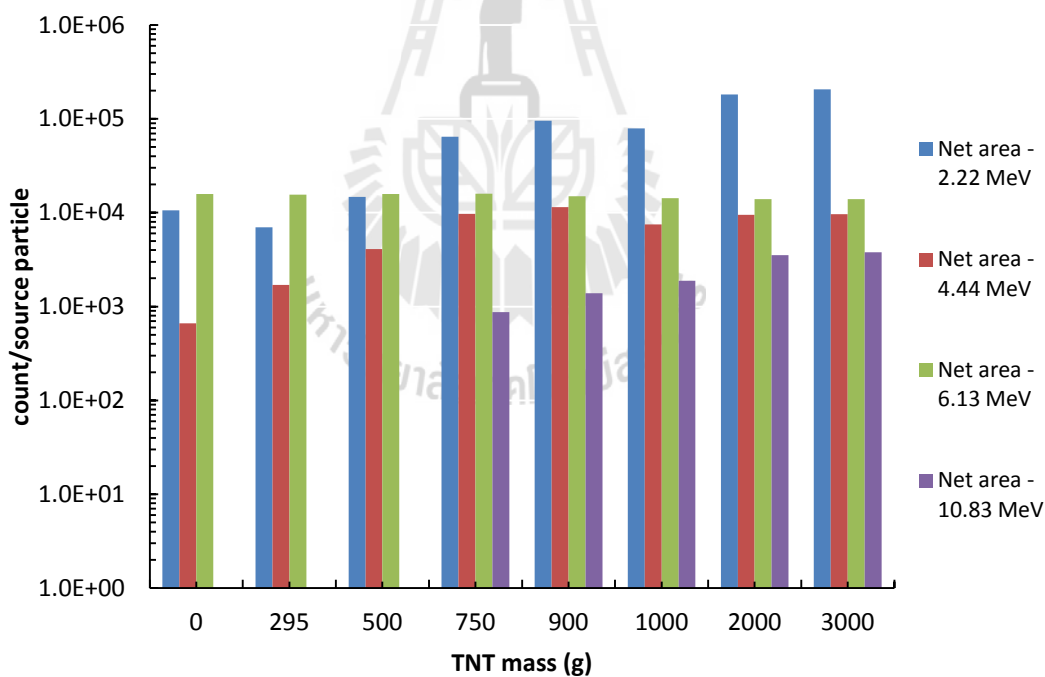
Figure 4.25 Comparison between net areas of the prominent gamma-rays resulting from the detections of TNT of difference masses ranging from 0-3,000 g.

Figure 4.26 shows a histogram of the prominent gamma-ray fluxes deduced from the gamma-ray spectra as shown in Table 4.2. Basically, the 2.2 and 4.4- MeV gamma-ray fluxes increases with TNT-mass, except the small drop at 900 g and increase again after that mass value. The 6.13 MeV gamma-rays show small fluctuations of gamma-ray fluxes with TNT mass. The 10.83 MeV increases with TNT mass. The nature of this variation is not yet known but it can relate to three factors: the self-neutron moderation of TNT- mass, the self-neutron absorption of TNT-mass and the gamma-ray attenuation by sand-formation. The mechanisms of these factors need to be studied in more details.

The effect of varying depth is studied next by putting 1 kg TNT under sand-formation with the buried depths ranging from 2-22 cm. The BGO/^{252}Cf-detector head is used in this simulation. Figure 4.26 shows the gamma-ray spectra resulting from the simulation, while Figure 4.28 shows the comparison between net areas of the prominent gamma-rays deduced from Figure 4.27. Figure 4.28 shows that most prominent gamma-rays intensities decrease with mass, except that of the 6.13 MeV. This simulation indicate that the the BGO/^{252}Cf-detector head can detect 1 kg TNT-landmine buried under sand-formation as deep as 22 cm.
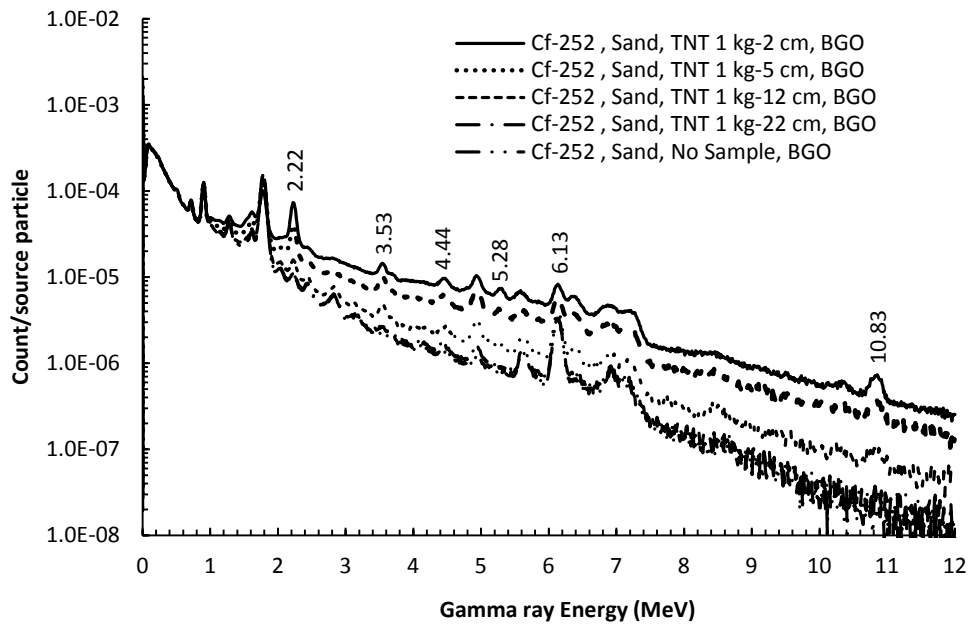
Figure 4.26   Comparisons of gamma-ray spectra resulting from the detections of 1-kg TNT-landmine buried under sand-formation with different depths ranging from 2-22 cm.
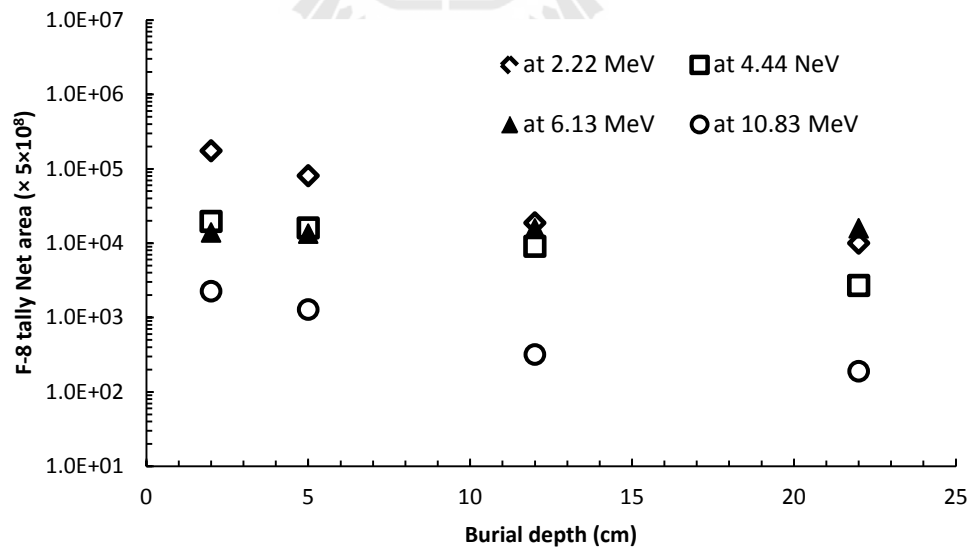
Figure 4.27   Comparisons between net areas of the 2.2, 4.4, 6.1 and 10.8 MeV gamma-rays deduced from the spectra of Figure 4.27.

4.2.2.3 Simulation Results of The BGO/^{241}Am-^{9}Be/TNT-Combination

In the simulation, the detection compositions are the same as those of Section 4.2.2.2, except the neutron source is replaced with ^{241}Am-^{9}Be. The objective of this simulation is to investigate the characteristics of gamma-ray spectra resulting from using the BGO/ ^{241}Am-^{9}Be detector-head to detect 1-kg TNT-landmine buried under sand-formation at 5-cm depth.
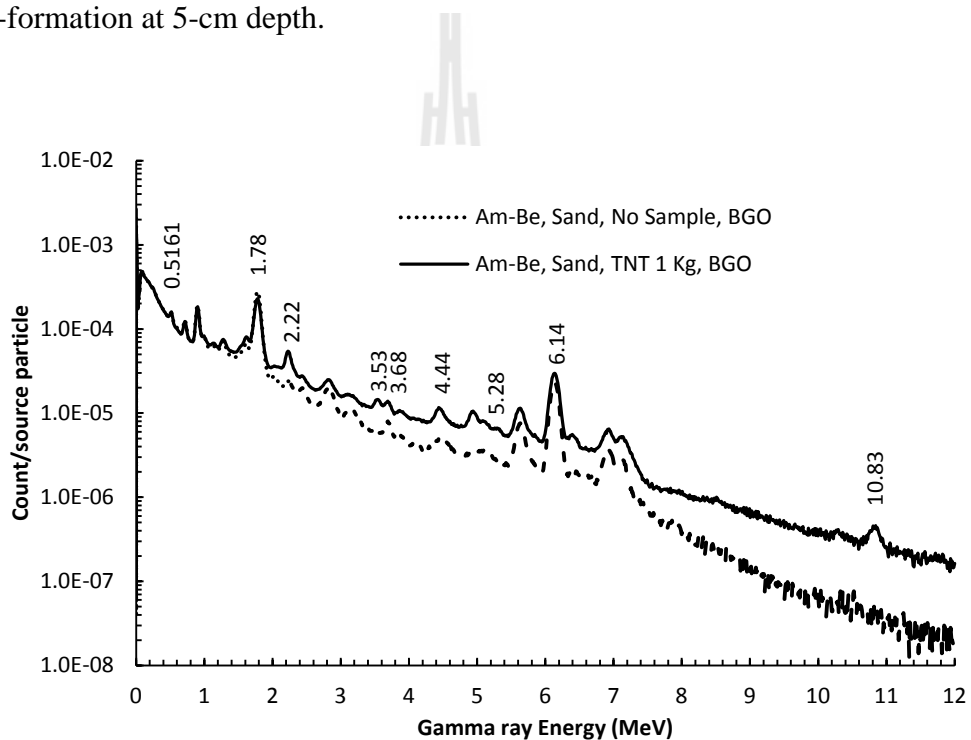
Figures 4.28 Comparisons between gamma-ray spectra resulting from the detection of 3-kg TNT-landmine with sand-formation.

Figures 4.29 represent comparisons between gamma-ray spectra resulting from the detections of 1-kg TNT-landmine buried under sand-formation at 5-cm deep and that of sand-formation. By eye inspection in these two figures, it is clear the all the prominent gamma-rays (2.22, 4.44, 6.13 and 10.83 MeV) appeared in the

spectrum. Since ^{241}Am-^{9}Be emits neutrons with higher energies than those of ^{252}Cf, it can induce these gamma-rays with higher intensities.

Figure 4.30 shows the comparison of gamma-rays spectra resulting from the detections of 1-kg TNT buried under sand-formation at different depths ranging from 2-12 cm. Net areas of these gamma-ray energies are deduced with the results compared in Figure 4.31. The net areas of all prominent gamma-rays decrease with buried depths, except the 6.13 MeV which showing almost constant value.
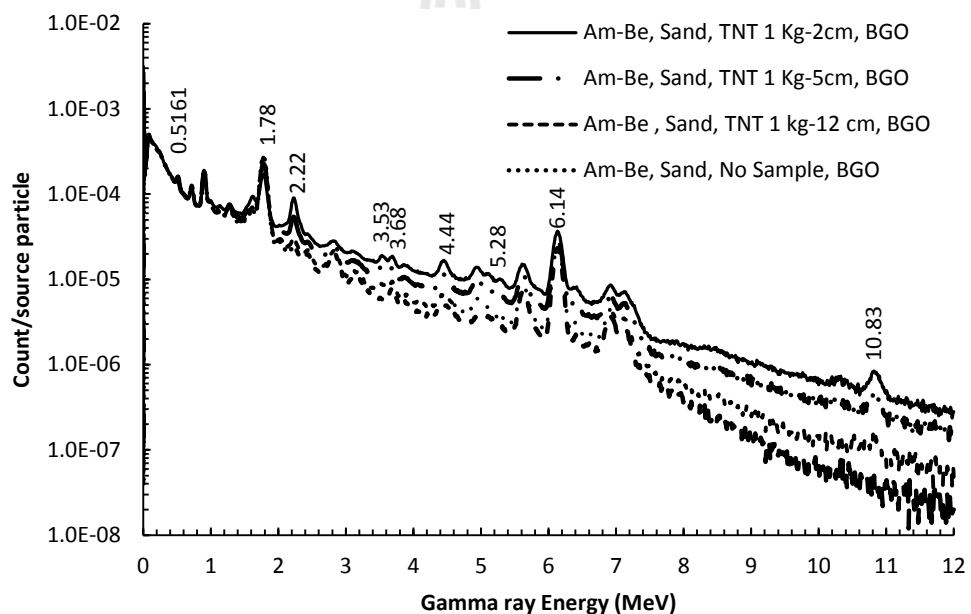
Figure 4.29 Comparisons between gamma-ray spectra resulting from the detections of 1 kg TNT-landmine buried under sand-formation with different depths ranging from 2 to 12 cm.
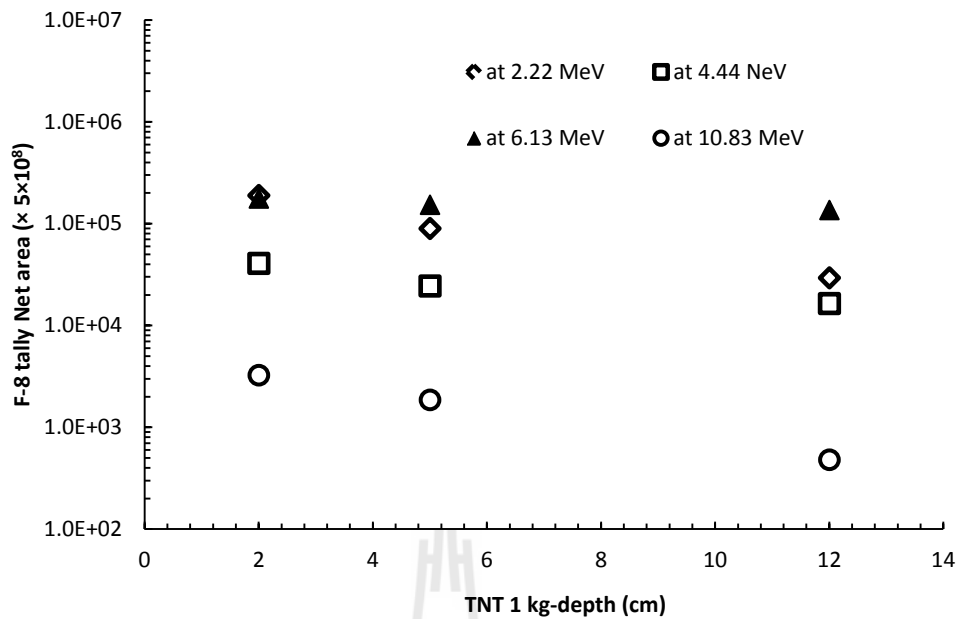
Figure 4.30 Comparisons of net areas of the 2.2, 4.4, 6.1 and 10.8 MeV gamma-rays resulting from the detections of 1kh TNT-landmine buried under sand-formation at depth raging from 2-12 cm.

4.2.2.4 Simulation Results of The BGO/$^{-252}$Cf/CaCO$_3$/TNT-Combination

In the simulation, the detection combination is the same as that of Section 4.2.2.2, except that the formation is replaced with CaCO$_3$. The objective of this simulation is to investigate the characteristic of gamma-ray spectra, resulting from the detection of TNT-landminne burying under CaCO$_3$-formation at 5-cm depth. Figure 4.32 shows the comparison between gamma-ray spectra resulting from the detection of the F-8 tally gamma-ray spectra, resulting from the detections of 1-kg TNT-landmine under CaCO$_3$-formation at 5-cm depth.
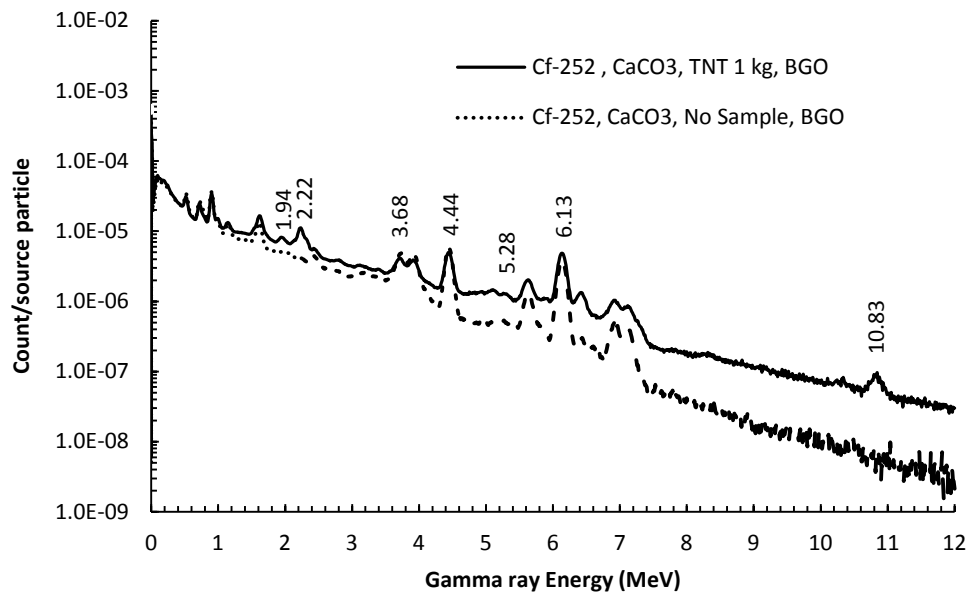
Figures 4.31 Comparisons between gamma-rays spectra resulting from the detections of 1-kg TNT-landmine buried under $CaCO_3$-formation at 5-cm deep.

In the simulation, all of the prominent gamma-rays (2.22, 4.44, 6.13 and 10.8 MeV) showed up in the spectrum of TNT. Some of the gamma-rays that do not interfere with the major ones, including the 3.68 MeV from $^{16}O(n,\alpha)^{13}C$-interaction with cross section of 0.064 b, also showed up in the spectrum. However, since $CaCO_3$ contains Ca, C and O as its elemental compositions, the 4.44 and 6.13 MeV gamma-rays will not be useful for the landmine detection.

4.2.2.5 Simulation Results of The BGO/^{241}Am-^{9}Be/$CaCO_3$/TNT-Combination

In the simulation, the detection combination is the same as that of Section 4.2.2.4, except that the neutron source is replaced with ^{241}Am-^{9}Be. The objective of this simulation is to investigate the characteristic of gamma-ray spectra, resulting

from the detection of TNT-landmine buried under $CaCO_3$-formation at 5-cm depth. Figure 4.33 shows the comparison of the F-8 tally gamma-ray spectra, resulting from the detections of 1 kg TNT-landmine under $CaCO_3$-formation at 5-cm deep.
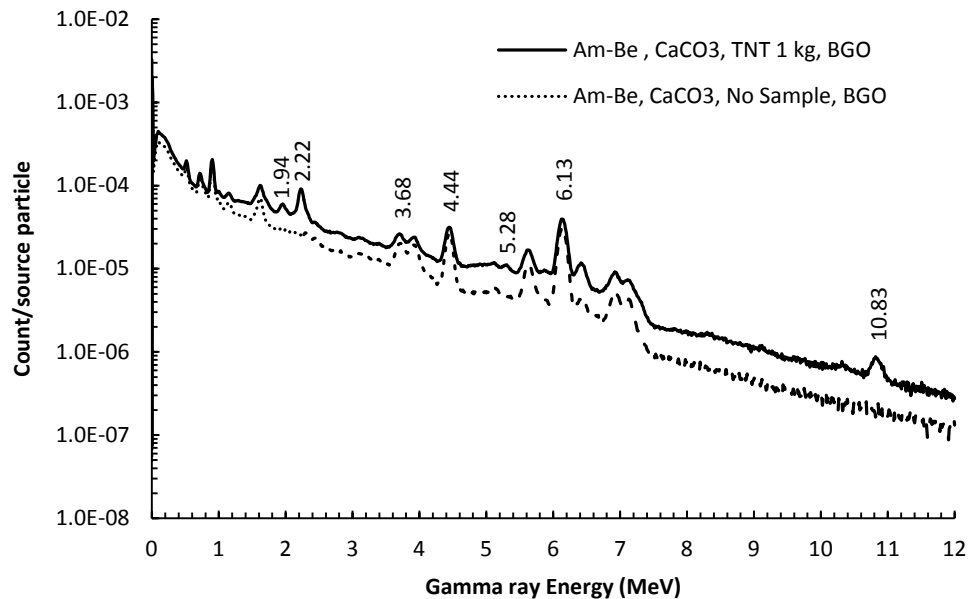
Figures 4.32 Comparisons between gamma-rays spectra resulting from the detections of 1 kg TNT-landmine buried under $CaCO_3$-formation at 5-cm deep.

In the simulation, all of the prominent gamma-rays (2.22, 4.44, 6.13 and 10.8 MeV) showed up in the spectrum. Since ^{241}Am-^{9}Be emits neutrons with higher energies than those from ^{252}Cf, the resulting gamma-ray intensities based on using ^{241}Am-^{9}Be are higher than those from ^{252}Cf. Since $CaCO_3$ contains Ca, C and O as its elemental compositions, the 4.44 and 6.13 MeV gamma-rays will not be useful for the landmine detection.

4.2.2.6 Simulation Results of The BGO/^{252}Cf/Clay/TNT-
Combination

In this simulation, the detection combination is the same as that of Section 4.2.2.4, except that the formation is replaced with clay. The objective of this simulation is to investigate the characteristic of gamma-ray spectra, resulting from the detection of TNT-landmine, burying under clay-formation at 5-cm depth. Figure 4.34 shows the comparison of the F-8 tally gamma-ray spectra, resulting from the detections of 1 kg TNT-landmine under clay-formation at 5 cm deep.
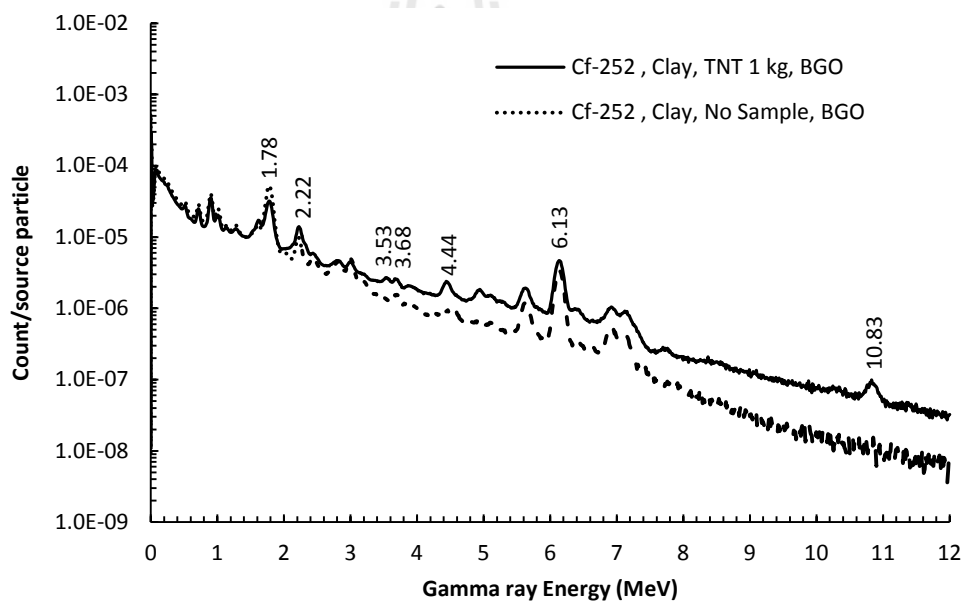
Figures 4.33 Comparisons between gamma-rays spectra resulting from the detections of 1-kg TNT-landmine under clay-formation at 5-cm deep.

In the simulation, all of the prominent gamma-rays (2.22, 4.44, 6.13 and 10.8 MeV) showed up in the spectrum. However, since clay contain O, Si, Al and H as was discussed in Section 4.2.1.5, the 2.22 and 6.13 MeV gamma-rays should not be

qualify to be used for the landmine detection. Nevertheless, the combination of the 4.44 and 10.83 MeV gamma-rays should be good enough to be used for landmine detection

4.2.2.7 Simulation Results of The BGO/ ^{241}Am-^{9}Be/Clay/TNT-Combination

In the simulation, the detection combination is the same as that of Section 4.2.2.6, except that the neutron source is replaced with ^{241}Am-^{9}Be. The objective of this simulation is to investigate the characteristic of gamma-ray spectra, resulting from the detection of TNT-landmine, burying under clay-formation at 5-cm depth. Figure 4.35 shows the comparison of the F-8 tally gamma-ray spectra, resulting from the detections of 1 kg TNT-landmine buried under clay-formation at 5 cm deep.
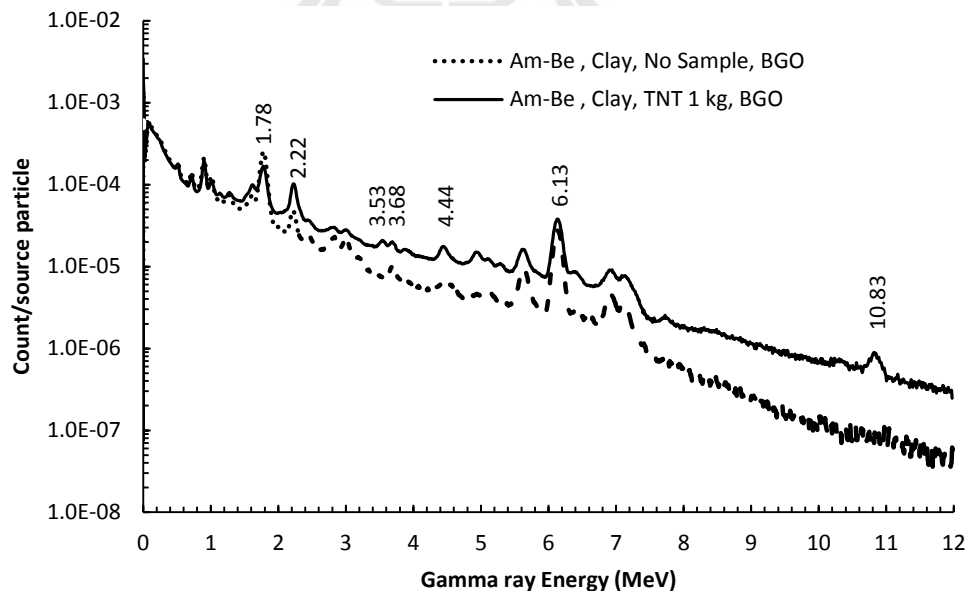
Figures 4.34 Comparison between gamma-ray spectra resulting from the detections of 1 kg TNT-landmine buried under clay-formation at 5-cm deep.

The same as in Section 4.2.2.6, all of the prominent gamma-rays (2.22, 4.44, 6.13 and 10.8 MeV) showed up in the spectrum. As was discussed in last section, the 2.22 and 6.13 MeV gamma-rays can't be used for the landmine detection because they are the source of interferences. However, the combination of the 4.44 and 10.83 MeV gamma-rays should be good enough to be used for landmine detection

4.2.3 Simulation Results Based on Using LaBr$_3$:Ce

The same as the simulation in Sections 4.2.1 and 4.2.2, the simulations of landmine detection based on using LaBr$_3$:Ce consist four combinations of detection's components. These combinations are simulated in this section. The following sections give the simulation results of these detection combinations.

4.2.3.1 Simulation Results of The LaBr$_3$:Ce/^{252}Cf/Sand-Combination

This simulation is similar to that of Section 4.2.2.1, except that the gamma-ray detector is replaced with LaBr$_3$:Ce. Figure 4.36 (a) and (b) show the simulated gamma-ray spectra based on using ^{252}Cf to detect sand-formation with TNT-landmine of 1-kg, buried under sand-formation at 5-cm depth. By eye inspection, Figure 4.36 shows that all four prominent gamma-ray occurred in the spectrum with some interferences occur at the 2.22 and 4.44 MeV lines. The interference at 2.22 MeV comes from the 2.31 MeV of the ^{14}N(n, n′γ)^{14}N- interaction, while that at 4.44 MeV comes from the 4.52 MeV of the ^{14}N(n,γ)^{15}N- interactions. However, there is no interference at both the 6.13 and 10.83 MeV.
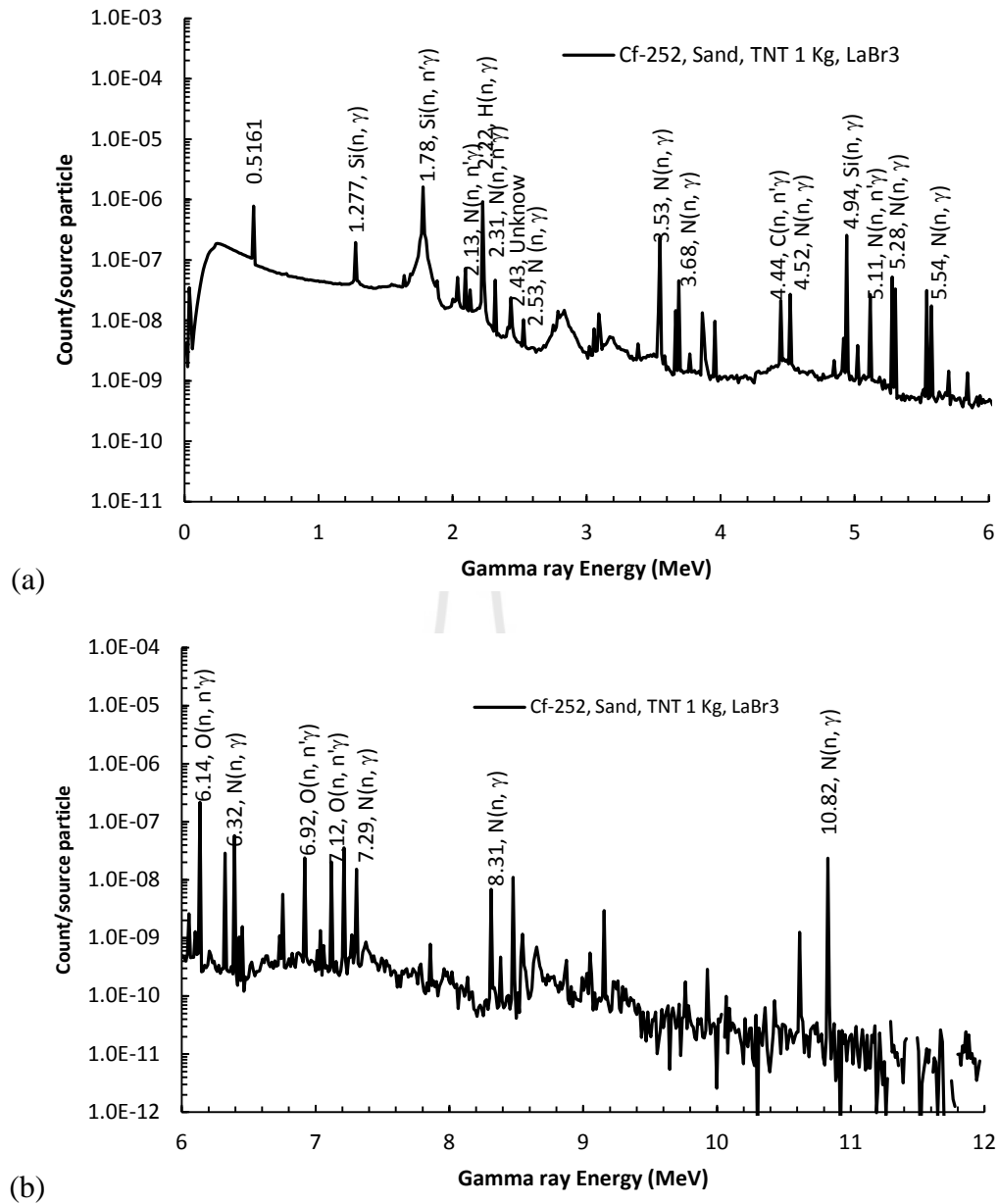
Figure 4.35 Simulated gamma-ray spectra, resulting from the detections of sand-formation by using ^{252}Cf-neutron source.

Figure 4.37 depicts comparisons of the simulated F-8 tally gamma-ray spectra resulting from the detections of 1-kg TNT-landmine buried under sand-formation by using three gamma-ray detectors, NaI(Tl), BGO and LaBr$_3$:Ce These spectra show that the LaBr$_3$:Ce -gamma-ray detector has higher resolution than those of NaI(Tl) and

BGO detectors. It also has lower Compton continuum. These characteristics may make the LaBr$_3$:Ce -gamma-ray detector suitable for the detection of TNT-landmine.
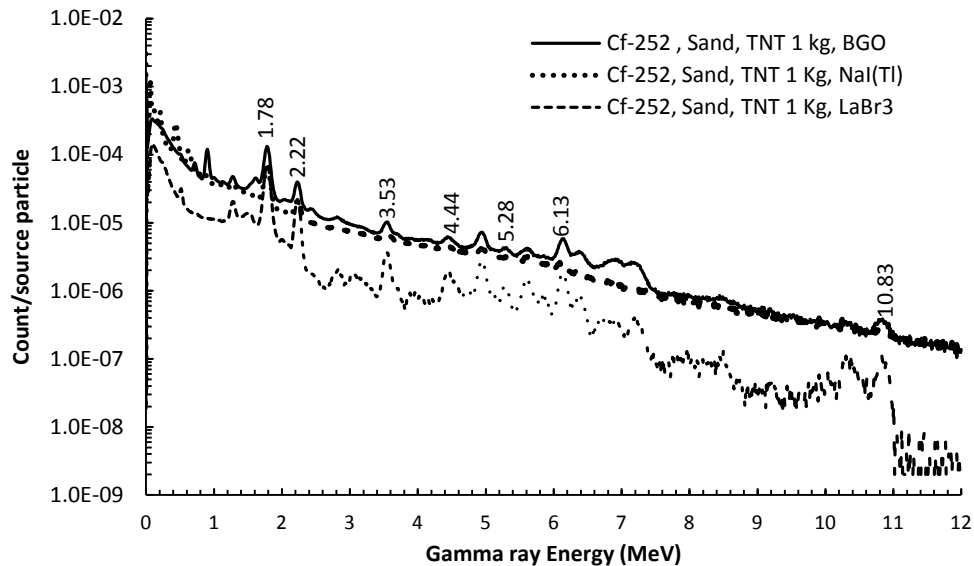
Figure 4.36   Comparisons of the simulated F-8 tally gamma-ray spectra resulting from the detections of 1-kg TNT-landmine buried under sand-formation at 5-cm deep by using NaI(Tl), BGO and LaBr$_3$:Ce- gamma-ray detectors.

Figure 4.39 shows the comparison of the simulated gamma-rays spectra resulting from the detections of TNT-landmines of 290 g and 1,000 g buried under sand-formation at 5-cm depth with the sand-formation alone. The characteristic of the 290 g-spectrum is almost the same as that of the sand-formation spectrum. This characteristic implies that the detection of small landmine buried at 5-cm depth is rather difficult or the detection mass limit of TNT- landmine is about 290g. Figure 4.40 shows the comparison of net areas or the gamma-ray intensities of the 2.22, 4.44, 6.13 and 10.83 MeV.
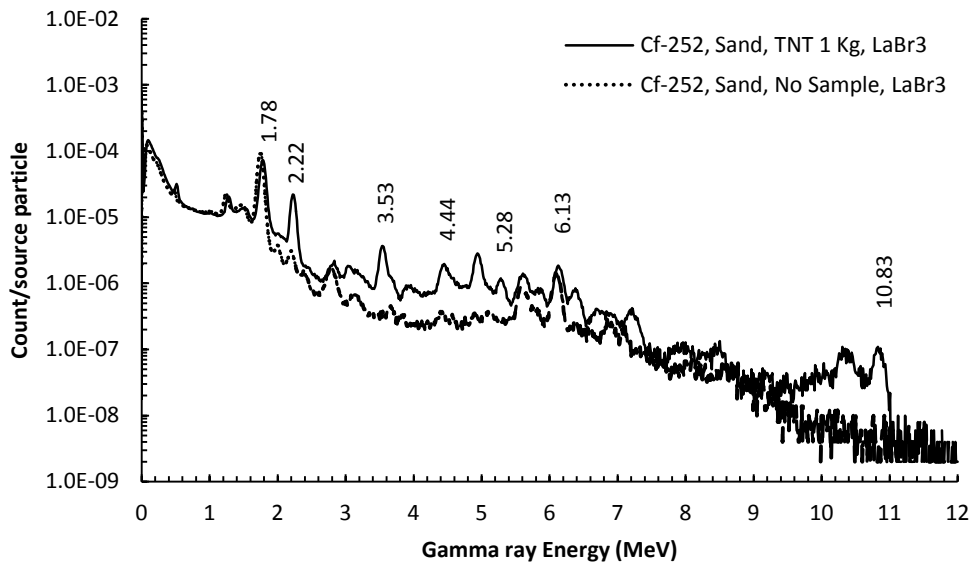
Figure 4.37   Comparison between the F-8 gamma-rays spectra resulting from the detections of 1-kg TNT-landmine buried under sand-formation at 5-cm and from sand-formation.
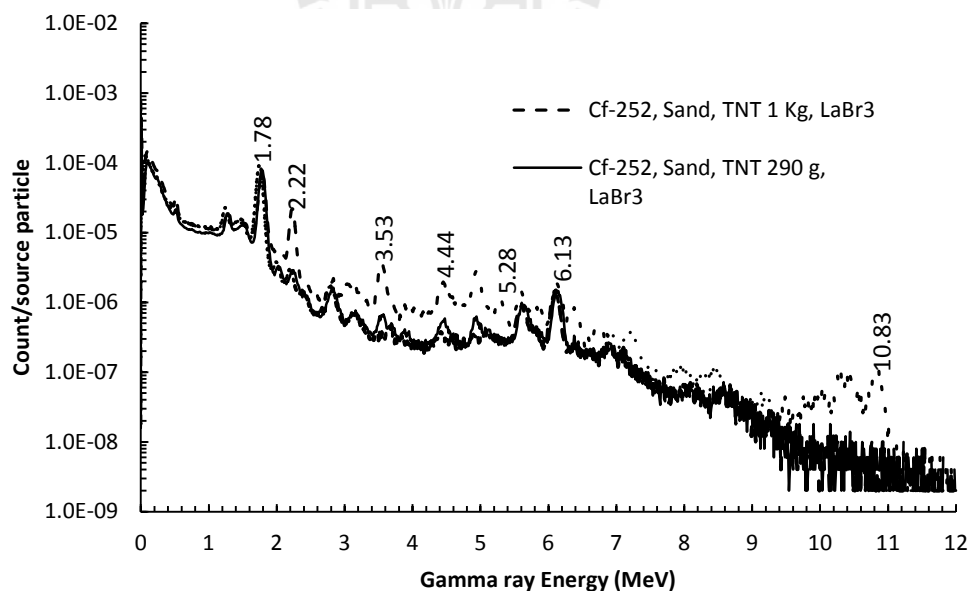
Figure 4.38   Comparisons between gamma-ray spectra resulting from the detections of TNT-landmines with masses of 290g and 1,000g.

It was found that the TNT-based 2.22 MeV line has lower intensity than that of sand-formation alone, while the 10.8 MeV line shows some net area when TNT-landmine mass is 290g. Net areas of the 4.44 MeV increases with mass, while the 6.13 MeV net area shows some fluctuations.
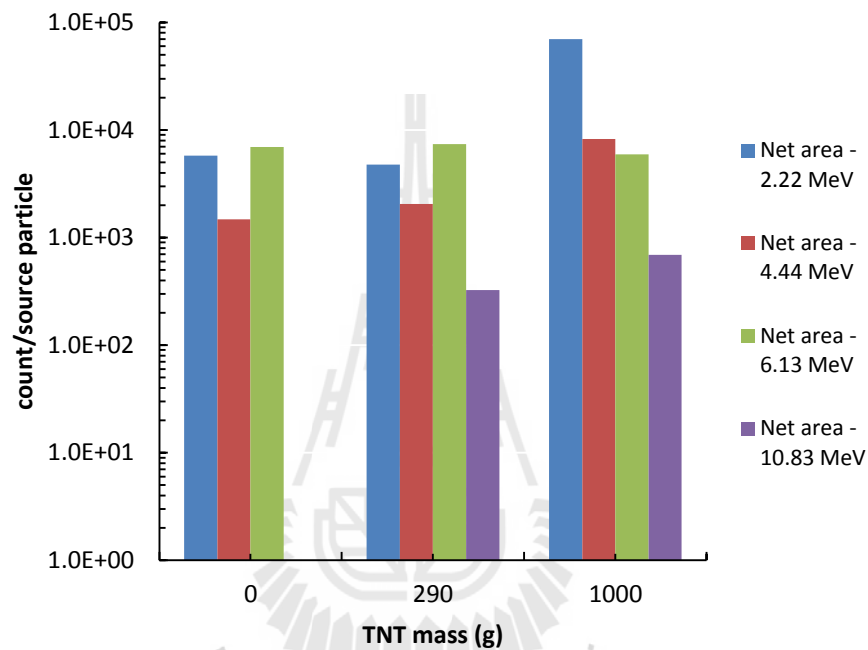
Figure 4.39 Histogram of the net areas of the 2.22, 4.44, 6.13 and 10.8 MeV gamma-rays resulting from the detections of TNT-landmines of 290 and 1,000g and sand-formation alone.

4.3   Discussion

In Section 4.1, the simulations of the detections of elemental compositions of TNT-landmines and ground-formations: H, C, N, O, Si, Al and Ca, were performed. The objective of these simulations is to investigate the characteristics of gamma-ray spectra resulting from the detections of the mentioned elements. The results of these

simulations give us the types of gamma-ray energies which arise from neutron interactions of H, C, N, O, Si, Al and Ca. The sources of interferences between the arising gamma-rays are learned, which in turn, give us ideas of how to resolve the interferences.

In Section 4.2, simulations of the detections of TNT-landmine and ground-formations (sand, $CaCO_3$, clay), in the form of materials, were performed. The objective of these simulations is to investigate the characteristics of the gamma-ray spectra resulting from the detections of TNT-landmine and ground formations. The results of these simulations give us the major gamma-ray fluxes resulting from the activations of those materials' elemental compositions. Net areas, which equivalent to fluxes of the prominent gamma-rays are deduced and the results tabulated. The results from Sections 4.2 and 4.3 will be used to estimate the simulated ratios of gamma-ray fluxes resulting from the neutron interactions of TNT's elemental compositions for comparisons with the respective theoretical ratios. The following sections give the derivation of the theoretical gamma-ray flux ratios and the comparisons of the theoretical gamma-ray flux ratios with the simulated gamma-ray flux ratios

4.3.1 Derivation of the Theoretical Gamma-Ray Flux Ratios

In this section, the theoretical gamma-ray flux ratios between gamma-rays resulting from the neutron interactions with TNT's elemental compositions are derived. Assuming that n_i is the number of nuclei of the ith-elemental compositions of TNT-landmine. The number of gamma-rays resulting from the neutron interaction of the ith-elemental compositions, N_i, can be written as

$$N_i \propto \sigma_i n_i \qquad (4.1)$$

where σ_i is the cross-section of the ith-neutron-interaction type. The number of nuclei of the ith-elemental compositions of TNT-landmine can be written as

$$n_i = \frac{\rho N_A A_i}{M} \tag{4.2},$$

where ρ is the density of the TNT-landmine, N_A is the Avogadro's number (0.6022×10^{24} atoms/mol), A_i is the number of atoms of the ith-elemental compositions of the TNT- molecule and M is the molecular weight of TNT. Substitution of Eq. (4.2) into Eq. (4.1), then, gives the number of the resulting gamma-rays,

$$N_i = \sigma_i \frac{\rho N_A A_i}{M} \tag{4.3}.$$

These gamma-rays are created at the TNT-landmine position which may not be detected by the gamma-ray detector that locates at a certain position away from the TNT-landmine position. The number of gamma-rays detected by the gamma-ray detector can be written as

$$C_i = N_i \in_i \Omega_d f_i \tag{4.4},$$

where $\in_i$, Ω_d, f_i are the detection efficiency, the detector solid angle and the gamma-ray attenuation factor of the gamma-ray detector, respectively. The gamma-ray attenuation factor is given by

$$f_i = \exp\left[-\frac{\mu}{\rho} \rho x\right] \tag{4.5},$$

where μ is the gamma-ray attenuation coefficient, ρ is the density of TNT-landmine and x is the distance between the gamma-ray detector and the TNT-landmine. Substitution of Eq. (4.3) in Eq. (4.4), we obtain

$$C_i = \sigma_i \in_i \Omega_d f_i \frac{\rho N_A A_i}{M} \tag{4.6}.$$

For the 2.22 MeV gamma-ray which result from the ^{1}H(n, γ) ^{2}H-interaction, the number of gamma-rays detected by the gamma-ray detector can be written as

$$C_H = \sigma_H \in_H \Omega_d f_H \frac{\rho_{TNT} N_A A_H}{M} \qquad (4.7).$$

For other prominent gamma-ray energies, the 4.44 and 10.83 MeV, the detected numbers can be written in the same way. The ratio between the 2.22 MeV and 10.83 MeV gamma-rays can, then, be written as

$$\frac{C_H}{C_N} = \frac{\sigma_H \in_H \Omega_d f_H \dfrac{\rho_{TNT} N_A A_H}{M}}{\sigma_N \in_N \Omega_d f_N \dfrac{\rho_{TNT} N_A A_N}{M}} \qquad (4.8).$$

After the same parameters are canceled out, Eq. (4.8) becomes

$$\frac{C_H}{C_N} = \frac{\sigma_H f_H \in_H A_H}{\sigma_N f_N \in_N A_N} \qquad (4.9).$$

Similarly, the gamma-ray ratio between the 4.44 MeV and 10.83 MeV is given by

$$\frac{C_C}{C_N} = \frac{\sigma_C f_C \in_C A_C}{\sigma_N f_N \in_N A_N} \qquad (4.10).$$

In case of the 2.22 MeV and the 4.44 MeV, their ratio can be written as

$$\frac{C_H}{C_C} = \frac{\sigma_H f_H \in_H A_H}{\sigma_C f_C \in_C A_C} \qquad (4.11).$$

4.3.2 Comparisons Between Theoretical and Simulated Gamma-Ray Flux Ratios

In this section, the comparisons between theoretical and simulated gamma-ray flux ratios are performed. The theoretical ratios are calculated by using equations in Section 4.2.1 while the simulated ratios are estimated by taking the ratios of the

deduced net areas of the gamma-ray peaks resulting from MCNP-simulations. Parameters required for calculations of theoretical ratios of gamma-ray fluxes resulting from 1 kg of TNT-landmine ($C_7H_5O_6N_3$) detection are given in Table 4.3. Detection parameters required for the calculations of the theoretical ratios are given in Table 4.3 while the deduced net areas or the gamma-ray fluxes required for the estimation of the simulated ratios based on using ^{252}Cf- and ^{241}Am-^{9}Be-neutron sources are given in Table 4.4 and 4.5, respectively

Table 4.3   Parameters required for calculations of theoretical ratios of gamma-ray fluxes resulting from 1-kg of TNT-landmine ($C_7H_5O_6N_3$.) detection.

Energy (MeV)	$\in(E\gamma)$			$\sigma\gamma(b)$	$f_i(E\gamma)$	A_i
	BGO	NaI(Tl)	LaBr$_3$:Ce			
H-2.22	1.00	1.00	1.00	0.33	0.62	5
C-4.44	0.92	0.98	0.67	0.18-0.43	0.72	7
O-6.13	0.54	0.95	0.57	0.165	0.75	6
N-10.83	0.54	0.96	0.34	0.11	0.79	3

Table 4.4   Net areas used for the estimation of the simulating ratios based on using ^{252}Cf

Energy	^{252}Cf		
	BGO	NaI(Tl)	LaBr$_3$:Ce
2.22	78255.00±279.74	30211.00±173.81	69958.00±264.50
4.44	7460.00±86.37	3319.00±57.61	7689.00±87.69
10.83	1274.00±35.69	826.00±28.74	623.00±24.96

Table 4.5   Net areas used for the estimation of the simulated ratios based on using
^{241}Am-^{9}Be

Energy	^{241}Am-^{9}Be		
	BGO	NaI(Tl)	LaBr$_3$:Ce
2.22	85446.00±292.31	22760.00±150.86	60868.00±246.71
4.44	7460.00±86.37	7522.00±86.73	14437.00±120.15
10.83	1404.00±37.47	490.00±22.14	528.00±22.98

Since the 6.13 MeV gamma-rays resulting from the ^{16}O(n, n′γ)^{16}O-neutron interaction of TNT-landmine has a high level of interferences from gamma-rays resulting from ^{16}O, the sand-formation's elemental composition, they are not used for comparisons in this thesis. Only three gamma-ray flux ratios are used for comparisons in this thesis:

1) Ratios between the 2.22 and 10.83 MeV gamma-ray fluxes (C_H/C_N),

2) Ratios between the 4.44 and 10.83 MeV gamma-ray fluxes (C_C/C_N),

3) Ratios between the 2.22 and 4.44 MeV gamma-ray fluxes (C_H/C_N).

Table 4.6   Theoretical ratios of gamma-ray fluxes resulting from the detection of
1-kg TNT-landmine based on using BGO, NaI and LaBr$_3$:Ce gamma-ray detectors.

Ratio	BGO	NaI(Tl)	LaBr$_3$:Ce
C_H/C_N	72.67	40.88	115.41
C_C/C_N	58.63	35.13	67.81
C_H/C_C	1.24	1.16	1.70

Table 4.7   Comparisons of the theoretical and simulated gamma-ray flux ratios
resulting from the detections of 1-kg TNT-landmine based on using the BGO, NaI(Tl)
and LaBr$_3$:Ce gamma-ray detectors and ^{252}Cf- and ^{241}Am-^{9}Be- neutron sources.

Ratio	BGO		
	Theory	^{252}Cf	^{241}Am-^{9}Be
C_H/C_N	72.67	61.42±1.73	60.86±1.64
C_C/C_N	58.63	5.86±0.18	5.31±0.15
C_H/C_C	1.24	10.49±0.13	11.45±0.14
Ratio	NaI(Tl)		
	Theory	^{252}Cf	^{241}Am-^{9}Be
C_H/C_N	40.88	36.58±1.29	46.45±2.12
C_C/C_N	35.13	4.02±0.16	15.35±0.72
C_H/C_C	1.16	9.10±0.17	3.03±0.04
Ratio	LaBr$_3$:Ce		
	Theory	^{252}Cf	^{241}Am-^{9}Be
C_H/C_N	115.41	112.29±4.52	115.28±5.04
C_C/C_N	67.81	12.34±0.36	27.34±1.21
C_H/C_C	1.70	9.10±1.74	4.22±0.04

As shown in Table 4.6, agreements between the theoretical and simulated
ratios within their error limits are obtained in the C_H/C_N ratio based on using the
LaBr$_3$:Ce/^{252}Cf- and LaBr$_3$:Ce/^{241}Am-^{9}Be-detector-heads. However, the simulated
C_H/C_N ratio based on using BGO and NaI(Tl)- detectors do not agree with those of
theoretical ratios within their error limits, though they are quite close. Notice the large
disagreements between the C_C/C_N ratios, in which, the largest disagreement can be up
to about 10 times. In the case of C_H/C_C ratios, though most of them show large
disagreements but those of the NaI(Tl)/^{241}Am-^{9}Be- and LaBr$_3$/^{241}Am-^{9}Be-detector-
heads show only about 2 times different. The large disagreements of the C_C/C_N and
C_H/C_C ratios may result from the high level of gamma-ray interferences due to some

other types of neutron interactions which have similar gamma-ray energies to those of the ^{12}C(n, n'γ)^{12}C- and ^{1}H(n, γ) ^{2}H-interactions. Next section will discuss about the correction of the simulated gamma-ray flux ratios due to these interferences.

4.3.3   Correction of the Simulated Gamma-Ray Flux Ratios due to Interferences

There are two methods used for the correction of the simulated gamma-ray flux ratios due to interferences.

4.3.3.1   Ratios Based on Cell Flux.

Tables 4.8 and 4.9 show the sources of interferences on the 2.223 MeV and 4.439 MeV gamma-rays which effect the correctness of the simulated gamma-ray ratios, C_H/C_N, C_C/C_N and C_H/C_C. This effect can be estimated by subtracting out the interfering contributions of the 2.237 MeV from the ^{28}Si (n,γ)^{29}Si-interaction and those of neutron interactions appearing in Table 4.8. The interfering contribution of the 2.237 MeV is proportional to the number of ^{28}Si-nuclei of the sand-formation, while interfering contributions of the 2.237 MeV are proportional to the number of ^{16}O nuclei of the sand-formation and ^{14}N of the TNT-landmine. The volume of the cell in front of the detector is used to estimate the numbers of silicon and oxygen nuclei with the results (N_i) shown in Table 4.8 and 4.9. Multiplying these numbers with their respective cross sections, we obtain the percentages of interferences for the 2.237 and 4.439 MeV gamma-rays of about 1 and 29% respectively. Subtracting out these interferences from the 2.237 and 4.439 MeV gamma-rays, we obtain the

simulation corrected gamma-ray ratios as shown in Table 4.11. Comparing these corrected ratios to those of Table 4.7, we found that they show higher disagreements.

Table 4.8   The sources of interferences on the 2.223 MeV .

Eγ(MeV)	Element/Matt.	Reaction Type	$\sigma\gamma$(b)	n_i(atom)	$N_i = \sigma\gamma\, n_i$
2.223	H/TNT	^{1}H(n, γ)^{2}H	0.333	1.363×10^{25}	4.538×10^{24}
2.237	Si/SiO$_2$	^{28}Si(n,γ)^{29}Si	0.003	1.348×10^{25}	4.043×10^{22}

Table 4.9   The sources of interferences on the 4.439 MeV.

Eγ(MeV)	Element/Matt.	Reaction Type	$\sigma\gamma$(b)	n_i(atom)	$N_i = \sigma\gamma\, n_i$
4.439	C/TNT	^{12}C(n, n'γ)^{12}C	0.178	1.908×10^{25}	3.397×10^{24}
4.445	N/TNT	^{14}N(n,α)^{11}B	0.059	8.177×10^{24}	4.825×10^{23}
4.439	N/TNT	^{14}N(n, t)^{12}C	0.036	8.177×10^{24}	2.944×10^{23}
4.439	O/TNT	^{16}O(n, n'α)^{12}C	0.014	1.635×10^{25}	2.289×10^{23}
4.439	O/SiO$_2$	^{16}O(n, n'α)^{12}C	0.014	2.695×10^{25}	3.773×10^{23}

Table 4.10   The sources of interferences on the 6.13 MeV.

Eγ (MeV)	Element/Matt.	Reaction Type	$\sigma\gamma$(b)	n_i(atom)	$N_i = \sigma\gamma\, n_i$
6.13	O/TNT	^{16}O(n,n'γ)^{16}O	0.180	1.635×10^{25}	2.943×10^{24}
6.13	O/SiO$_2$	^{16}O(n,n'γ)^{16}O	0.180	2.695×10^{25}	4.851×10^{24}

Table 4.11   Comparisons of the corrected ratios by Cell flux method of the theoretical and simulated gamma-ray flux ratios resulting from neutron activations of 1-kg TNT-landmine based on using the BGO, NaI(Tl) and LaBr$_3$:Ce gamma-ray detectors and the ^{252}Cf- and ^{241}Am-^{9}Be-neutron sources.

Ratio	BGO		
	Theory	^{252}Cf	^{241}Am-^{9}Be
C_H/C_N	72.67	60.81±1.71	60.25±1.62
C_C/C_N	58.63	4.15±0.12	3.77±0.11
C_H/C_C	1.24	14.15±0.18	15.97±0.19
Ratio	NaI(Tl)		
	Theory	^{252}Cf	^{241}Am-^{9}Be
C_H/C_N	40.88	36.21±1.28	45.98±2.09
C_C/C_N	35.13	2.85±0.11	4.22±0.06
C_H/C_C	1.16	12.69±0.23	10.90±0.04
Ratio	LaBr$_3$:Ce		
	Theory	^{252}Cf	^{241}Am-^{9}Be
C_H/C_N	115.41	111.17±4.47	114.13±4.99
C_C/C_N	67.81	8.76±0.25	19.41±0.86
C_H/C_C	1.70	12.68±2.43	5.76±0.25

4.3.3.2 Ratios based on F-4 tally and cross section

In this method, the ratios of the F-4 tallies and cross sections of gamma-rays resulting from the detections of TNT-landmine are used to estimate the interfering contributions from the 2.237 and 4.439 MeV gamma-rays. The same sources on interferences as of the cell flux method are shown in Table 4.8 and 4.9. The interference contributions of the 2.23 MeV can be estimated by taking the ratio of the F-4 gamma-ray flux of the 2.237 with respect to that of the 2.237 MeV. In case of the 4.439 MeV from the ^{12}C(n, n'γ)^{12}C-interaction, the interfering contributions can be estimated by taking the ratios of its cross sections to those of its interfering gamma-

rays. By using this method, we obtain the gamma-ray interfering contributions of the 2.237 and 4.439 MeV of about 14 and 59%, respectively. Subtracting these interfering contributions from the 2.23 and 4.44 gamma-rays, the simulated gamma-ray ratios become as shown in Table 4.12. The results of this method also make comparisons with the theoretical ratios worse.

Table 4.12 Comparison of the F-4 tally and cross section method of the theoretical and simulated gamma-ray flux ratios resulting from neutron activations of 1 kg TNT-landmine based on using the BGO, NaI(Tl) and LaBr$_3$:Ce gamma-ray detectors and the ^{252}Cf- and ^{241}Am-^{9}Be- neutron sources.

Ratio	BGO		
	Theory	^{252}Cf	^{241}Am-^{9}Be
C_H/C_N	72.67	52.82±1.49	52.34±1.40
C_C/C_N	58.63	3.46±0.10	3.14±0.09
C_H/C_C	1.24	15.26±0.18	16.66±0.20
Ratio	NaI(Tl)		
	Theory	^{252}Cf	^{241}Am-^{9}Be
C_H/C_N	40.88	31.45±1.11	39.59±1.82
C_C/C_N	35.13	2.38±0.05	9.08±0.42
C_H/C_C	1.16	13.24±0.24	4.40±0.06
Ratio	LaBr$_3$:Ce		
	Theory	^{252}Cf	^{241}Am-^{9}Be
C_H/C_N	115.41	96.57±3.88	99.14±4.33
C_C/C_N	67.81	7.31±0.21	16.17±0.71
C_H/C_C	1.70	13.23±2.53	6.13±0.06

CHAPTER V

CONCLUSIONS

The conclusions of this thesis are presented in this chapter with the following sections

5.1 Simulation Results Based on the F-4 Tally

In this thesis, simulations based on F-4 tallies are used to explore types of gamma-ray energies and intensities, resulted from the neutron-interactions of TNT-landmines and ground-formations. As discussed in Sections 4.1 and 4.2, the simulation results of the detections of TNT-landmine and sand- formation's elemental compositions show that all four major gamma-rays (2.22, 4.44, 6.13 and 10.83 MeV) occurred in the simulation spectra with fluxes correspond to their cross sections as shown in Table 4.1. These gamma-rays are the results of the neutron interactions of H, C, N and O, the elemental compositions of TNT-landmine. Some low intensities gamma-rays with energies close to those of the major gamma-rays due to neutron activations of both TNT-landmine and sand-formation's elemental compositions also occurred. These gamma-rays may give interfering problem to those of the major gamma-rays. However, because the intensities of these gamma-rays are low, the interfering problems are limited. The real interfering problem is due to the 6.13 MeV gamma-rays, resulted from the neutron interactions of oxygen in sand-formation. This

interfering problem is unavoidable for the detection of landmine buried under sand-formation.

5.2   Simulation Results Based on F-8 Tally

The simulation based on F-8 tally is used to explore the characteristic or shape of the gamma-ray spectra in this thesis. As discussed in Section 4.2, gamma-ray spectra resulted from the detections of TNT-landmines and ground-formations show the occurrence of all four major gamma-rays. In these spectra, an interfering problem show up at the upper shoulder of the 2.22 MeV due to the 2.23 MeV gamma-ray from neutron activation of silicon nuclei from sand-formation. Another interfering problem existed at the 4.44 MeV due to four low cross-section gamma-rays as shown in Table 4.9. In the case of the 6.13 MeV gamma-ray, resulted from the neutron activation of oxygen nuclei, the interfering problem is unavoidable because both TNT-landmine and sand-formation contain oxygen as their elemental compositions. There is no interfering problem at the 10.83 MeV gamma-rays which appeared alone at the high end of the spectra. Because of these interfering problems, some of the C_H/C_N, C_C/C_N and C_H/C_C do not agree with each other as discussed in Chapter IV. However, the C_H/C_N ratio based on using the LaBr3:Ce Gamma-ray detector show agreement between theory and simulation within their error limits.

5.3   TNT-Landmine Detection Limits

In this thesis, simulations of the TNT-landmine detections with varying mass and depth are performed. As discussed in Section 4.2.3, the LaBr$_3$:Ce/^{252}Cf detector head can detect 290g TNT-landmine buried under sand-formation at 5-cm with net

area of 235. Therefore, the mass limit of TNT-landmine detection by using the LaBr$_3$:Ce/^{252}Cf detector head is 290g. This limit is based on using TNA technique. In the case of depth limit, the simulation results in Sections 4.2.2 and 4.2.3 show that the TNA technique can detect 1 kg TNT-landmine at 22-cm with NaI(Tl)/^{241}Am-^{9}Be-, BGO/^{252}Cf- and BGO/^{241}Am-^{9}Be-detector heads. The depth detection limit is therefore 22-cm with TNA technique. However, since detection simulation based on varying mass and depth by using LaBr$_3$:Ce/^{252}Cf- and LaBr$_3$:Ce/^{241}Am-^{9}Be- detector heads were not performed in this thesis, the detection limits of these detector heads are not available.

5.4 Final Conclusion and Suggestion for Further Study

The simulation results in this thesis suggested that the complementary FNA-TNA technique which utilizes the detections of thermal and fast neutron activation of TNT-landmine's elemental compositions can't be used to detect TNT-landmine efficiently. However, the TNA technique which utilizes the detections of the 2.22 and 10.83 MeV gamma-rays concurrently can be used to detect 1 kg TNT-landmine very efficiently. Moreover, our simulation results indicate that the TNA technique may be able to detect TNT-landmine with mass down to 750g with about 5% error. The detector of better resolution and efficiency are required to make the complementary FNA-TNA technique useful for the efficient detection of TNT-landmine. However, the results of this simulation should be tested experimentally.

REFERENCES
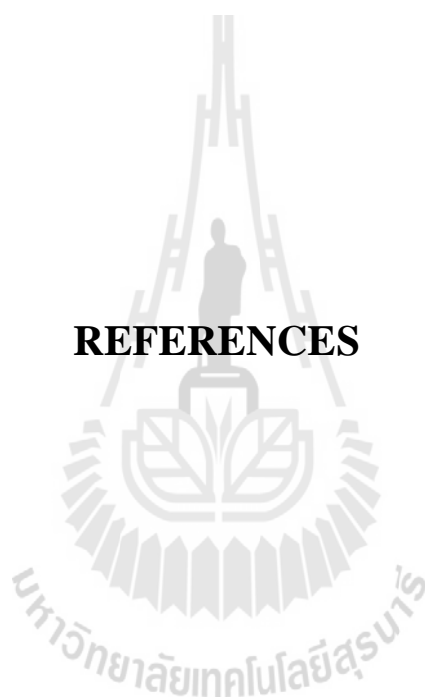
REFERENCES

Bartle, C.M., Purcell, C.R., and Wilson, A. (1990). Determination of the moisture content of wheat, using the NEUGAT technique. **Nucl. Instr. & Meth. A.** 291: 655-661.

Bom, V.R., Ali, M.A., and van Eijk, C.W.E. (2006). Land mine detection with neutron back scattering imaging using a neutron generator. **IEEE Transactions on Nuclear Science.** 53: 356-360.

Bom, V.R., Datema, C.P., and van Eijk, C.W.E. (2004). The status of the Delft University Neutron Backscatter Landmine Detector (DUNBLAD). **Appl. Radiat. Isot.** 61: 21-25.

Brooks, F.D., Drosg, M., Buffler, A., and Allie M.S. (2004). Detection of anti-personnel landmines by neutron scattering and attenuation. **Appl. Radiat. Isot.** 61: 27-34.

Brooks, F.D., Drosg, M. (2005). The HYDAD-D antipersonnel landmine detector. **Appl. Radiat. Isot.** 63: 565-574.

Buffler, A. (2004). Contraband detection with fast neutrons. **Radiat. Phys. Cham.** 71: 853-861.

Buffler, A., Brooks, F.D., Allie, M., Bharuth-Ram, K., and Nchodu, M.R. (2001). Material classification by fast neutron scattering. **Nucl. Instr. & Meth. B.** 173: 483-502.

Choi, H.D., Firestone, R.B., Lindstro, R.M., Molná, G.L., Mughabghab, S.F., Paviotti-Corcuer, R., Réva, Zs., Trko, A., and Zhou, C.M. (2006). Nuclear Data service., **Database of Prompt Gamma Rays from Slow Neutron Capture for Elemental Analysis. IAEA.** Vienna.

Csikai, J., Doczi, R., and Kiraly, B. (2003). Investigations on landmine detection by neutron-based techniques. In: Proceedings of the final RCM on the application of nuclear techniques to anti-personnel landmines identification, IAEA, Vienna.

Csikai, J. (2004). Application of nuclear techniques to anti-personnel landmines identification. **Appl. Radiat. Isot.** 61: 1.

Csikai, J., Hussein, E., and Rosengard, U. (Eds.). (2004). Applications of nuclear techniques to anti-personnel landmine identification, **Appl. Radiat. Isotope.** 61: 1-81

Clifford, E.T.H., J.E. McFee, H. Ing, H.R. Andrews, D. Tennant, E. Harper, and Faust, A.A. (2007). A militarily fielded thermal neutron activation sensor for landmine detection. **Nucl. Instr. Meth. A.** 579: 418-425.

Datema, C.P., Bom, V.R., and van Eijk, C.W.E. (2001). Landmine detection with the neutron backscattering method, **IEEE Trans. Nucl. Sci.** 48:1087-1091.

Datema, C.P., Bom, V.R., and van Eijk, C.W.E. (2002). Experimental results and Monte Carlo simulations of a landmine localization device using the neutron backscattering method. **Nucl. Instr. Meth. A.** 488: 441-450

Favalli, V., Mehner, H. C., and Simonelli, F. (2008). Wide energy range efficiency calibration for a lanthanum bromide scintillation detector. **Radiation Measurements.** 43: 506-509.

Faust, A.A., McFee, J.E., and Tom Cousins. (2004). Feasibility of Fast Neutron Analysis (FNA) for Detection of Buried Landmines. **Bubble Technology Industries Inc. Final report BTI-04/60-30.**

Knoll, G.F. (1989). **Radiation Detection and Measurement, Second edition**, John Willey & Sons, New York.

Hashem Miri-Hakimabad, Hamed Panjeh and Alireza Vejdani-Noghreiyan. (2008). Experimental optimization of a landmine detection facility using PGNAA method. **Nucl . Sci. Technol.** 19: 109-112.

Hashem Miri-Hakimabad, Alireza Vejdani-Noghreiyan and Hamed Panjeh. (2007). Improving the moderator geometry of an anti-personnel landmine detection system. **Appl. Radiat. Isot.** 66: 606-611.

Hatice Akkurt, John Wagner, and Keith Eckerman. (2007). Hand held instruments for landmine detection: View from radiation dosimetry. **Nucl. Instr. Meth. A.** 579: 391-394.

Hussein, E.M.A., and Waller, E.J. (2000). Landmine detection: the problem and the challenge, **Appl. Radiat. Isot.** 53: 557-563.

IAEA. (1999). Proceedings of the First RCM on the Application of Nuclear Techniques to Anti-personnel Landmines Identification, Zagreb, Croatia. IAEA/PS/RC-799.

IAEA. (2001). Proceedings of the Second RCM on the Application of Nuclear Techniques to Anti-personnel Landmines Identification, St Petersburg, Russia. IAEA/PS/RC-799-2.

IAEA. (2003). Proceedings of the Final RCM on the Application of Nuclear Techniques to Anti-personnel Landmines Identification, IAEA, Vienna. 2003.

Kuznetsov, AV., Evsenin, AV., Gorshkov, IY., Osetrov, OI., Vakhtin, DN. (2004). Detection of buried explosives using portable neutron sources with nanosecond timing. **Appl Radiat Isot.** 61: 51-57.

Landmine Impact Survey Report : Kingdom of Thailand. (2001). (on-line). Available from: http://www.sac-na.org/pdf_text/thailand/THA_FinalReport.pdf.

Landmine Monitor Report. (2010). (on-line). Available from: http://www.the-monitor.org/lm/2010/.

Lisa McCoy. (2010). Landmine-affected families arrive to receive support on November 19, 2010. Koas Krala district office, Battambang province, Cambodia. (on-line). Available from: https://picasaweb.google.com/11715984465917 2352279.

Maućec, M., de Meijer, R. J. (2002). Monte Carlo simulations as a feasibility tool for non-metallic land-mine detection by thermal-neutron backscattering. **Appl. Radiat. Isot.** 56: 837-846.

Maućec, M., and Rigollet, C. (2004). Monte Carlo simulations to advance characterisation of landmines by pulsed fast/thermal neutron analysis. **Appl. Radiat. Isot.** 61: 35-42.

Monin, L, and Gallimore, A. (2002). The Devil's Gardens: A history of landmines. London, Pim-lico.

Miranda Leitsinger. (2009). Years after conflict, war legacy kills. (on-line). Available from: http://inthefield.blogs.cnn.com/tag/miranda-leitsinger/.

Orion, I. and Wielopolski, L., (2000). Response Function of the BGO and NaI(T1) Detectors Using Monte Carlo Simulation. **Annals of the New York Academy of Sciences.** 904: 271-275.

Pazirandeh Ali, Azizi Maryam, and Farhad Masoudi S. (2006). Monte Carlo assessment of soil moisture effect on high-energythermal neutron capture gamma-rayby ^{14}N. **Appl. Radiat. Isot.** 46: 1-6.

Perot, B., Carasco, C., Bernard, S., Mariani, A., Szabo, J.-L., Sannie, G., Valkovic, V., Sudac, D., Viesti, G., Lunardon, M., Botosso, C., Nebbia, G., Pesente, S., Moretto, S., Zenoni, A., Donzella, A., Moszynski, M., Gierlik, M., Klamra, W.,Le Tourneur, P. et al. (2008). Measurement of 14 MeV neutron-induced prompt gamma-ray spectra from 15 elements found in cargo containers. **Appl. Radiat. Isot.** 66: 421-434.

Simakovl, S. P., Pavlik, A., Vonach, H., and Hlavac, S. (1998). Status of Experimental and Evaluated Discrete γ-Ray Production at En=14.5 MeV. **Final Report of Research Contract 7809/RB, performed under the CRP on Measurement, Calculation and Evaluation of Photon Production Data.**

Takahashi, Y., Misawa, T., Masuda, K., Yoshikawa, K., Takamatsu, T., Yamauchi, K., Yagi, T., Pyeon, C.H., and Shiroya, S. (2011). Landmine detection method combined with backscattering neutrons and capture γ-rays from hydrogen. **Appl. Radiat. Isot.** 69: 1027-1032.

Takahashi, Y., Misawa, T., Masuda, K., Yoshikawa, K., Takamatsu, T., Yamauchi, K., Yagi, T., Pyeon, C.H., and Shiroya, S. (2010). Development of

landmine detection system based on the measurement of radiation from landmines. **Appl. Radiat. Isot.** 68: 2327-2334.

Tsoulfanidis N., **Measurement and Detection of Radiation, Second edition,** Taylor & Francis, Washington, 1995.

Uchai Worasit, Changkian Sommai, Lihua Zhu and Hancheng Sun. (2008). EXPERIMENT ON THE PERFORMANCE OF THE NEUTRON-BASED EXPLOSIVES DETECTION SYSTEM USING ^{252}Cf AND ^{241}Am/^{9}Be. **Suranaree J. Sci. Technol.** 2: 139-147.

Viesti, G., Lunardon, M., Nebbia, G., Barbui, M., Cinausero, M., D'Erasmo, D., Palomba, D., Pantaleo, A., Obhođaš, J., Valković, V. (2006). The detection of landmines by neutron backscattering: Exploring the limits of the technique. **Appl. Radiat. Isot.** 64: 706-716.

Vourvopoulos, G., Womble, P.C. (2001). Pulsed fast/thermal neutron analysis: a technique for explosives detection. **Talanta.** 54: 459-468.

Vourvopoulos, G., Sullivan, R.A., Knapp, V., and Hrupec, D. (2003). In: Sahli, H., Bottoms, A.M., Cornelis, J. (Eds.), EUDEM2-SCOT-2003, International Conference on Requirements and Technologies for the Detection, Removal and Neutralization of Landmines and UXO, Vrije Universiteit, Brussels, pp. 731-736.

X-5 Monte Carlo Team. (2003). MCNP-A General Monte Carlo N-Particle Trans-port Code., Version5, **Technical Report, Los Alamos National Laboratory**, Los Alamos, New Mexico.

APPENDICES
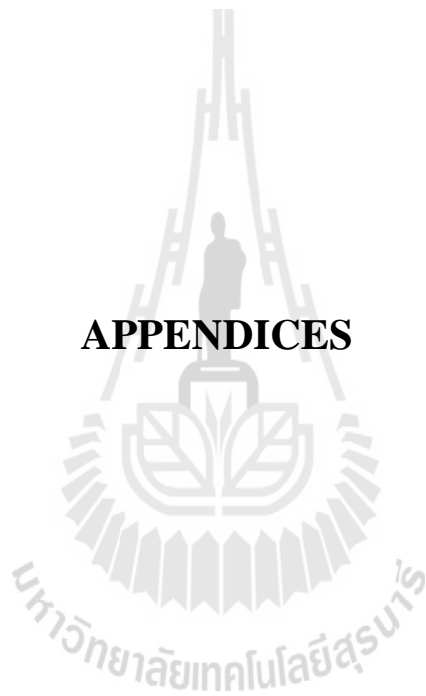
1. F-4 tally Simulation of Spherical Geometry

This input file is ^{252}Cf source in the center of cavity.

c SPHERE MODEL (C-single element)

1 0 -1 imp:n,p=1 $ r=10

2 12 -1 -2 #1 imp:n,p=1 $ r=20 (C-single element)

3 0 -7 #1 #2 imp:n,p=1 $ r=25

4 11 -3.67 -9 #1 #2 #3 imp:n,p=1 $ r=30

5 0 -10 #(-10) imp:n,p=1 $ r=50

6 0 10 imp:n,p=0 $ r=50

c SURFACE

1 so 10

2 so 20

3 so 21

4 so 22

5 so 23

6 so 24

7 so 25

8 so 30

9 so 35

10 so 50

MODE n p

PHYS:P 4j 1

c MATERIAL SPECIFICATION

m11 11023 0.4995 53127 0.4995 $ NaI

m12 6012 1 $ C-12

m13 7014 1 $ N-14

m14 8016 1 $ O-16

m15 20000 1 $ Ca

m16 14000 1 $ Si

m17 1001 1 $ H

m18 26000 1 $ Fe

c SOURCE DEFINITION

sdef pos= 0 0 0 erg=d1

si1   0.01e-6 0.025e-6 1e-6 1 24i 14

sp1   -3   1.025 2.926

f2:p 2

 e02 0 2.5e-8 1.0e-6 5.0e-6 1.0e-5 1.0e-4 1.0e-3 1024i 12

f4:p 4

 e04 0 2.5e-8 1.0e-6 5.0e-6 1.0e-5 1.0e-4 1.0e-3 1024i 12

f18:p 4

ft18 geb 2.5e-3 55.05e-3 0.52365e-6

e58 0 2.5e-8 1.0e-6 5.0e-6 1.0e-5 1.0e-4 1.0e-3 1024i 12

nps 2e9

2. F-4 and F-8 tally Simulation of Cylindrical Geometry

This input file is ^{241}Am-^{9}Be source in cylindrical model

c CYLINDRICAL MODEL

c 1 0 -11 12 -13 imp:n,p=1 $dt

c 2 11 -3.65 -14 12 -15 imp:n,p=1 $NaI

2 42 -7.13 -14 12 -15 imp:n,p=1 $Ge

c 3 3 -1.65 -21 23 -22 imp:n,p=1 $sample

3 3 -5.67 -21 23 -22 imp:n,p=1 $sample 1 k

c 3 3 -17.05 -21 23 -22 imp:n,p=1 $sample 3 k

4 0 01 -02 -04 #2 imp:n,p=1 $air

5 41 -2.6 -01 05 -08 #3 imp:n,p=1 $ cell 5

6 41 -2.6 -05 06 -08 imp:n,p=1 $ cell 6

7 41 -2.6 -06 07 -08 imp:n,p=1 $ cell 7

8 41 -2.6 -07 03 -08 imp:n,p=1 $ cell 8

9 41 -2.6 -01 05 -09 #3 #5 imp:n,p=1 $ cell 9

10 41 -2.6 -05 06 -09 #6 imp:n,p=1 $ cell 10

11 41 -2.6 -06 07 -09 #7 imp:n,p=1 $ cell 11

12 41 -2.6 -07 03 -09 #8 imp:n,p=1 $ cell 12

13 41 -2.6 -01 05 -04 #3 #5 #9 imp:n,p=1 $ cell 13

14 41 -2.6 -05 06 -04 #6 #10 imp:n,p=1 $ cell 14

15 41 -2.6 -06 07 -04 #7 #11 imp:n,p=1 $ cell 15

16 41 -2.6 -07 03 -04 #8 #12 imp:n,p=1 $ cell 16

c 5 4 -2.12 -01 03 -04 imp:n,p=1 $

17 0 -31 #(-04 -02 03) imp:n,p=1

18 0 31 imp:n,p=0

c surface

01 pz 0

02 pz 50

03 pz -40

04 cz 30

05 pz -10

06 pz -20

07 pz -30

08 cz 10

09 cz 20

c detector

11 cz 2.5

12 pz 10

13 pz 20

c 14 c/z 0 8.85 6.35

14 cz 6.35

15 pz 22.7

c sample

21 cz 4

c 22 pz -5

c 23 pz -8.5

22 pz -2

23 pz -5.5

c 22 pz 0.1

c 23 pz -3.4

c 22 pz -12

c 23 pz -15.5

c 22 pz -22

c 23 pz -25.5

c 22 pz -32

c 23 pz -35.5

c arg

31 so 100
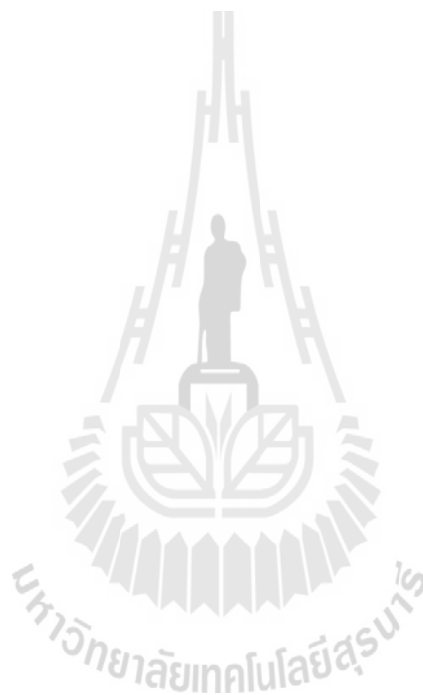
MODE n p

PHYS:P 4j 1

m1 2003 1 $He-3 d=0.1785 g/cm^3

m2 8016 -0.000301 7014 -0.000976 $air (d=0.0013 g/cm^3)

m23 8016 6 6012 4 7014 6 1001 6 $C-4 D=

c m3 1001 0.11 8016 0.89 $waterd=0.997 g/cm^3

m3 6012 0.02 1001 0.37 7014 0.19 8016 0.42 $TNT (d=1.65 g/cm^3)

m20 6012 -17.79 1001 -2.97 $HDPe 1.19

c m19 1001 0.06 6012 0.55 8016 0.35 7014 0.04 $Wood d=0.59

m21 6012 0.63685 1001 0.09798 7014 0.12378 8016 0.14139 $Nylon-

C12H22N2O2 D=1.14

m22 6012 5 1001 8 $ Rubber 0.94

m4   14000 0.47 8016 0.53 $Sand (SiO2 d=2.12 g/cm^3)

c m4 14000 1 1001 2 8016 3 $Sand (SiO2+H2O d=2.8065 g/cm^3)

c m4 20000 1 6012 1 8016 3 $Limestone(CaCO3 d= 2.71 g/cm^3)

c m5   48000 1 $cadmium (d= 8.650 g/cm^3)

c m6 5010 1 9019 3 $BF3(T=127K , 2.178e-3)

c m7 14000 0.47 8016 0.53 $sio2 fill water 5 %

m11 11023 0.4995 53127 0.4995 $ NaI detector 81000 0.001 d=3.67

m12 6012 1 $ C-12 D=2.67 g/cm^3

m13 7014 1 $ N-14 D=1.2506e-3 g/cm^3

m14 8016 1 $ O-16 D=1.429e-3 g/cm^3

m15 20000 1 $ Ca D=1.55 g/cm^3

m16 14000 1 $ Si D=2.33 g/cm^3

m17 1001 1 $ H D=0.0899e-3 g/cm^3

m18 26000 1 $ Fe D=7.874 g/cm^3

m19 13027 4 $ Al

m24 8016 6 6012 3 7014 6 1001 6 $RDX 1.816

c sample material

c m11   1001 2 6012 2 $CH2 -0.952

c m12   1001 2 8016 1 $H2O -1

c m13   1002 2 8016 1 $D2O -1.2

c m16   6012 1 $graphite -2.25

c m17   11023 1 17000 1 $NaCl

c m18   19000 1 17000 1 $KCl

c moderation material

c m21   1001 3 5010 1 6012 3 $Boric acid

c m22   3006 2 16000 1 8016 4 $Li2SO4 -2.06

c N_shielding material

c m31   3006 2 6012 1 8016 3 $Li2CO3 -0.88

m32   82207 1 $Pb -11.35

m35   6012 3 7014 6 1001 6 $ Melamine 1.57

m36   8016 6 6012 3 7014 3 1001 11 $ Silk 0.3

m40   6012 12 1001 22 8016 11 $ Sugar 1.59

m41 1001 0.01 8016 0.56 13027 0.07 14000 0.36 $soil(H,O,Al,Si) Density =

2.6 g/cc

m42 83209 4 33075 3 8016 12 $BGO [Bi4Ge3O12, Ge substituating by As]

D=7.13 g/cc

m43 1002 2 8016 1 $D2O D=1.1056 g/cc

c source definition

sdef pos= 0 0 5 erg=d1 dir=-1 vec= 0 0 1 par=1

c si1   0.01e-6 0.025e-6 1e-6 1 24i 14

c sp1   -3   1.025 2.926

si1   h 0.11 0.33 0.54 0.75 0.97 1.18 1.40 1.61 1.82 2.04

        2.25 2.47 2.68 2.90 3.11 3.32 3.54 3.75 3.97 4.18

```
         4.39  4.61  4.82  5.04  5.25  5.47  5.68  5.89   6.11  6.32

         6.54  6.75  6.96  7.18  7.39  7.61  7.82  8.03   8.25  8.46

         8.68  8.89  9.11  9.32  9.53  9.75  9.96  10.18  10.39  10.60

         10.82  11.03  11.09

sp1  d  0.000   0.014363   0.033397   0.031272   0.028119  0.025002

         0.021361   0.019831   0.017470   0.019248   0.022252

         0.021457   0.022482   0.022766   0.029506   0.035585

         0.036852   0.034583   0.030658   0.029987   0.026906

         0.028626   0.031784   0.030736   0.033340   0.030412

         0.027380   0.023319   0.020584   0.018152   0.017673

         0.020393   0.018299   0.016298   0.016773   0.016806

         0.018833   0.018374   0.016880   0.014352   0.009677

         0.006520   0.004255   0.003666   0.003805   0.005058

         0.006253   0.005519   0.004675   0.003695   0.002781

         0.001513   0.000363

f4:p 2

 e04  0 2.5e-8 1.0e-6 5.0e-6 1.0e-5 1.0e-4 1.0e-3 1024i 12

f18:p 2

ft18  geb  0  0.06  0

 e18  0 2.5e-8 1.0e-6 5.0e-6 1.0e-5 1.0e-4 1.0e-3 1024i 12

f38:p 2

ft38  geb  0.4  0  0

 e38  0 2.5e-8 1.0e-6 5.0e-6 1.0e-5 1.0e-4 1.0e-3 1024i 12

f58:p 2
```

ft58 geb 2.5e-3 55.05e-3 0.52365e-6

e58 0 2.5e-8 1.0e-6 5.0e-6 1.0e-5 1.0e-4 1.0e-3 1024i 12

f14:p 5

e14 0 2.5e-8 1.0e-6 5.0e-6 1.0e-5 1.0e-4 1.0e-3 1024i 12

f24:n 5

e24 0 2.5e-8 1.0e-6 5.0e-6 1.0e-5 1.0e-4 1.0e-3 1024i 12

f34:p 6

e34 0 2.5e-8 1.0e-6 5.0e-6 1.0e-5 1.0e-4 1.0e-3 1024i 12

f44:n 6

e44 0 2.5e-8 1.0e-6 5.0e-6 1.0e-5 1.0e-4 1.0e-3 1024i 12

f54:p 7

e54 0 2.5e-8 1.0e-6 5.0e-6 1.0e-5 1.0e-4 1.0e-3 1024i 12

f64:n 7

e64 0 2.5e-8 1.0e-6 5.0e-6 1.0e-5 1.0e-4 1.0e-3 1024i 12

f74:p 8

e74 0 2.5e-8 1.0e-6 5.0e-6 1.0e-5 1.0e-4 1.0e-3 1024i 12

f84:n 8

e84 0 2.5e-8 1.0e-6 5.0e-6 1.0e-5 1.0e-4 1.0e-3 1024i 12

f94:p 9

e94 0 2.5e-8 1.0e-6 5.0e-6 1.0e-5 1.0e-4 1.0e-3 1024i 12

f104:n 9

e104 0 2.5e-8 1.0e-6 5.0e-6 1.0e-5 1.0e-4 1.0e-3 1024i 12

f114:p 10

e114 0 2.5e-8 1.0e-6 5.0e-6 1.0e-5 1.0e-4 1.0e-3 1024i 12

f124:n 10

 e124 0 2.5e-8 1.0e-6 5.0e-6 1.0e-5 1.0e-4 1.0e-3 1024i 12

f134:p 11

 e134 0 2.5e-8 1.0e-6 5.0e-6 1.0e-5 1.0e-4 1.0e-3 1024i 12

f144:n 11

 e144 0 2.5e-8 1.0e-6 5.0e-6 1.0e-5 1.0e-4 1.0e-3 1024i 12

f154:p 12

 e154 0 2.5e-8 1.0e-6 5.0e-6 1.0e-5 1.0e-4 1.0e-3 1024i 12

f164:n 12

 e164 0 2.5e-8 1.0e-6 5.0e-6 1.0e-5 1.0e-4 1.0e-3 1024i 12

f174:p 13

 e174 0 2.5e-8 1.0e-6 5.0e-6 1.0e-5 1.0e-4 1.0e-3 1024i 12

f184:n 13

 e184 0 2.5e-8 1.0e-6 5.0e-6 1.0e-5 1.0e-4 1.0e-3 1024i 12

f194:p 14

 e194 0 2.5e-8 1.0e-6 5.0e-6 1.0e-5 1.0e-4 1.0e-3 1024i 12

f204:n 14

 e204 0 2.5e-8 1.0e-6 5.0e-6 1.0e-5 1.0e-4 1.0e-3 1024i 12

f214:p 15

 e214 0 2.5e-8 1.0e-6 5.0e-6 1.0e-5 1.0e-4 1.0e-3 1024i 12

f224:n 15

 e224 0 2.5e-8 1.0e-6 5.0e-6 1.0e-5 1.0e-4 1.0e-3 1024i 12

f234:p 16

 e234 0 2.5e-8 1.0e-6 5.0e-6 1.0e-5 1.0e-4 1.0e-3 1024i 12

f244:n 16

 e244 0 2.5e-8 1.0e-6 5.0e-6 1.0e-5 1.0e-4 1.0e-3 1024i 12

nps 5e8
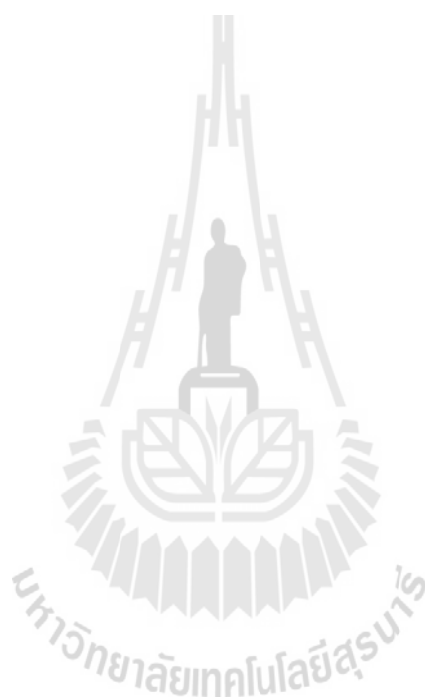
APPENDIX B

TABLE OF MASS FRACTIONS

Table B1 Compositions of materials as modelled in objects at the landmine location.

Material	Mass density (g/cm^3)	Mass fraction									
		H	C	O	N	Na	Al	Si	K	Ca	Fe
Water	1.00	0.11		0.89							
Polyethylene	1.19	0.14	0.86								
Wood	0.59	0.06	0.55	0.35	0.04						
Granite	2.75	0.01		0.56		0.01	0.04	0.31	0.02	0.03	0.01
Concrete	2.40	0.01		0.53		0.02	0.03	0.34	0.01	0.04	0.01
Sand	2.12			0.53				0.47			
Limestone (CaCO$_3$)	2.71		0.12	0.48						0.4	
TNT (C$_7$H$_5$O$_6$N$_3$)	1.65	0.02	0.37	0.42	0.19						
Soil	2.65	0.01		0.56			0.07	0.36			

The data (Mass fractions) are adopted from Table 2 as presented in Maucec (2001).

APPENDIX C

TABLE OF PHOTON ATTENUATION COEFFICIENTS

Table C1   Total Mass Attenuation Coefficients (μ/ρ) in cm^2/g for Gamma-Rays.

Material	Gamma-Ray Energy (MeV)								
	0.10	0.15	0.20	0.30	0.40	0.50	0.60	0.80	1.00
H	0.295	0.265	0.243	0.212	0.1890	0.1730	0.1600	0.1400	0.1260
Be	0.132	0.119	0.109	0.095	0.0847	0.0773	0.0715	0.0628	0.0565
C	0.149	0.134	0.122	0.106	0.0953	0.0870	0.0805	0.0707	0.0636
N	0.150	0.134	0.123	0.106	0.0955	0.0859	0.0805	0.0707	0.0636
O	0.151	0.134	0.123	0.107	0.0953	0.0870	0.0806	0.0708	0.0636
Na	0.151	0.130	0.118	0.102	0.0912	0.0833	0.0770	0.0676	0.0608
Mg	0.160	0.135	0.122	0.106	0.0944	0.0860	0.0795	0.0699	0.0627
A1	0.161	0.134	0.120	0.103	0.0922	0.0840	0.0777	0.0683	0.0614
Si	0.172	0.137	0.125	0.107	0.0954	0.0869	0.0802	0.0706	0.0635
P	0.174	0.144	0.122	0.104	0.0928	0.0846	0.0780	0.0685	0.0617
S	0.188	0.135	0.127	0.108	0.0958	0.0874	0.0806	0.0707	0.0635
A	0.188	0.149	0.117	0.098	0.0867	0.0790	0.0730	0.0638	0.0573
K	0.215	0.158	0.127	0.106	0.0938	0.0852	0.0786	0.0689	0.061 8
Ca	0.238	0.183	0.132	0.109	0.0965	0.0876	0.0809	0.0708	0.0634
Fe	0.344	0.206	0.138	0.106	0.0919	0.0828	0.0762	0.0664	0.0595
Cu	0.427	0.389	0.147	0.108	0.0916	0.0820	0.0751	0.0654	0.058 5
Mo	1.030	0.563	0.225	0.130	0.0998	0.0851	0.076 1	0.0648	0.0575
Sn	1.580	0.648	0.303	0.153	0.1090	0.0886	0.0776	0.0647	0.0568
I	1.830	0.139	0.339	0.165	0.1140	0.0913	0.0792	0.0653	0.0571
W	4.210	1.440	0.708	0.293	0.1740	0.1250	0.1010	0.0763	0.0640
Pt	4.750	1.640	0.795	0.324	0.1910	0.1350	0.1070	0.0800	0.0659
T1	5.160	1.800	0.866	0.346	0.2040	0.1430	0.1120	0.0824	0.0675
Pb	5.290	1.840	0.896	0.356	0.2080	0.1450	0.1140	0.0836	0.0684
U	1.060	2.420	1.170	0.452	0.2590	0.1760	0.1360	0.0952	0.0757
Air	1.570	0.134	0.123	0.106	0.0953	0.0868	0.0804	0.0706	0.0655
NaI	0.151	0.568	0.305	0.155	0.1110	0.0901	0.0789	0.0657	0.0577
H_2O	0.167	0.149	0.136	0.118	0.1060	0.0966	0.0896	0.0786	0.0706
Concrete	0.169	0.139	0.124	0.107	0.0954	0.0870	0.0804	0.0706	0.0635
Tissue	0.163	0.144	0.132	0.115	0.1000	0.0936	0.0867	0.0761	0.1683

Table C1   Total Mass Attenuation Coefficients (μ/ρ) in cm^2/g for Gamma-Rays (Continued).

Material	Gamma-Ray Energy (MeV)								
	1.25	1.50	2.00	3.00	4.00	5.00	6.00	8.00	10.00
H	0.1130	0.1030	0.0876	0.0691	0.0579	0.0502	0.0446	0.0371	0.0321
Be	0.0504	0.0459	0.0394	0.0313	0.0266	0.0234	0.0211	0.0180	0.0161
C	0.0568	0.0518	0.0444	0.0356	0.0304	0.0270	0.0245	0.0213	0.0194
N	0.0568	0.0517	0.0445	0.0357	0.0306	0.0273	0.0249	0.0218	0.0200
O	0.0568	0.0518	0.0445	0.0359	0.0309	0.0276	0.0254	0.0224	0.0206
Na	0.0546	0.0496	0.0427	0.0348	0.0303	0.0274	0.0254	0.0229	0.0215
Mg	0.0560	0.0512	0.0442	0.036	0.0315	0.0286	0.0266	0.0242	.0.0228
A1	0.0548	0.0500	0.0432	0.0353	0.0310	0.0282	0.0264	0.0241	0.0229
Si	0.0567	0.0517	0.0447	0.0367	0.0323	0.0296	0.0277	0.0254	0.0243
P	0.0551	0.0502	0.0436	0.0358	0.0316	0.0290	0.0273	0.0252	0.0242
S	0.0568	0.0519	0.0448	0.0371	0.0328	0.0302	0.0284	0.0266	0.0255
A	0.0512	0.0468	0.0407	0.0338	0.0301	0.0279	0.0266	0.0248	0.0241
K	0.0552	0.0505	0.0438	0.0365	0.0327	0.0305	0.0289	0.0274	0.0267
Ca	0.0566	0.0518	0.0451	0.0376	0.0338	0.0316	0.0302	0.0285	0.0280
Fe	0.0531	0.0485	0.0424	0.0361	0.0330	0.0313	0.0304	0.0295	0.0294
Cu	0.0521	0.0476	0.0418	0.0357	0.0330	0.0316	0.0309	0.0303	0.0305
Mo	0.0510	0.0467	0.0414	0.0365	0.0349	0.0344	0.0344	0.0349	0.0359
Sn	0.0501	0.0459	0.0408	0.0367	0.0355	0.0355	0.0358	0.0368	0.0383
I	0.0502	0.0460	0.0409	0.037	0.0360	0.0361	0.0365	0.0377	0.0394
W	0.0544	0.0492	0.0437	0.0405	0.0402	0.0409	0.0418	0.0438	0.0465
Pt	0.0554	0.0501	0.0445	0.0414	0.0411	0.0418	0.0427	0.0448	0.0477
T1	0.0563	0.0508	0.0452	0.042	0.0416	0.0423	0.0433	0.0454	0.0484
Pb	0.0569	0.0512	0.0457	0.0421	0.0420	0.0426	0.0436	0.0459	0.0489
U	0.0615	0.0548	0.0484	0.0445	0.0440	0.0446	0.0455	0.0479	0.0511
Air	0.0567	0.0517	0.0445	0.0357	0.0307	0.0274	0.0250	0.0220	0.0202
NaI	0.0508	0.0465	0.0412	0.0367	0.0351	0.0347	0.0347	0.0354	0.0366
H$_2$O	0.0630	0.0575	0.0493	0.0396	0.0339	0.0301	0.0275	0.0240	0.0219
Concrete	0.0567	0.0517	0.0445	0.0363	0.0317	0.0287	0.0268	0.0243	0.0229
Tissue	0.0600	0.0556	0.0478	0.0384	0.0329	0.0292	0.0267	0.0233	0.0212

From Gladys White Grodstein, "X-ray Attenuation Coefficients from 10 keV to 100 MeV" NBS Circular 583 (April 30, 1957).

CURRICULUM VITAE

NAME: Mr. Anan Sutcha

GENDER: Male

NATIONALITY: Thai

DATE OF BIRTH: September 22, 1979

EDUCATION BACKGROUND:

- 2007-2011, M.Sc. study at Suranaree University of Technology.

- 1999-2003, B.Sc. Physics from Kasetsart University, Bangkok, Thailand.

CONFERENCE:

- Feasibility Study of Using Neutron Back-scattering Technique In Landmine Detection by Monte Carlo Simulation (2009). Siam Physics Congress: Physics for Dynamic Society, SPC 2009.